# Final Technical Report

U.S. Geological Survey Award Nos. G23AP00389 and G23AP00390

## Basin Effects in the Central and Eastern United States: Collaborative Research with Tufts University and Merrimack College

**Laurie G. Baise, Ph.D.**
Professor and Chair, Dept. of Civil and Env. Engineering, Tufts University, 200 College Ave, Medford, MA, 02155; Tel: 617-627-2211, Fax: 617-627-3994, laurie.baise@tufts.edu

**James Kaklamanos, Ph.D.**
Professor, Dept. of Civil Engineering, Merrimack College, 315 Turnpike Street, North Andover, MA, 01845; Tel: 978-837-3401, KaklamanosJ@merrimack.edu

**Elise H. Meyer**
Graduate Student Researcher, Dept. of Civil and Env. Engineering, Tufts University, 200 College Ave, Medford, MA, 02155; Tel: 617-627-3211, Elise.Meyer@tufts.edu

**Irvin M. Guzman**
Undergraduate Student Researcher, Dept. of Civil Engineering, Merrimack College, 315 Turnpike Street, North Andover, MA, 01845; Tel: 978-837-5000, GuzmanIM@merrimack.edu

**George A. Sachs-Walor**
Undergraduate Student Researcher, Dept. of Civil Engineering, Merrimack College, 315 Turnpike Street, North Andover, MA, 01845; Tel: 978-837-5000, SachsWalorG@merrimack.edu

**Arden J. Dioslaki**
Undergraduate Student Researcher, Dept. of Civil Engineering, Merrimack College, 315 Turnpike Street, North Andover, MA, 01845; Tel: 978-837-5000, DioslakiA@merrimack.edu

**Shiying Nie, Ph.D.**
Postdoctoral Researcher, Dept. of Civil and Env. Engineering, Tufts University, 200 College Ave, Medford, MA, 02155; Tel: 858-405-2727, shiying.nie@tufts.edu

**Weiwei Zhan, Ph.D.**
Assistant Professor, Dept. of Civil, Env. and Construction Engineering, University of Central Florida, 4000 Central Florida Blvd, Orlando, FL, 32816; Tel: 407-823-1361, Weiwei.Zhan@ucf.edu

**Date:** 30 November 2024

**Project Term:** 1 August 2023 – 31 July 2024

**Acknowledgment of Support and Disclaimer:**

This material is based upon work supported by the U.S. Geological Survey under Grant Nos. G23AP00389 and G23AP00390. The views and conclusions contained in this document are those of the authors and should not be interpreted as representing the opinions or policies of the U.S. Geological Survey. Mention of trade names or commercial products does not constitute their endorsement by the U.S. Geological Survey.

# Abstract

Current Central and Eastern United States (CEUS) ground-motion models (GMMs) rely on the average shear-wave velocity in the upper 30 m of the subsurface ($V_{S30}$) as the primary site parameter. Most CEUS GMMs lack parameters quantifying basin effects, despite observations and simulations of basin effects on ground motions (Moschetti et al., 2020; Rekoske et al., 2022; Wang et al., 2022). In this study, we use mixed-effects regression to compute site-to-site terms from ground-motion predictions using the CEUS NGA-East GMMs (Goulet et al. 2021a; Hashash et al., 2020; Stewart et al., 2020) and two different ground-motion datasets (Goulet et al., 2021b; Thompson et al., 2023). These site-to-site terms exhibit strong regional trends consistent with large structures, such as the Mississippi Embayment, the Superior Uplands, and different sections of the Atlantic Coastal Plain.

In this study, we develop a new two-parameter linear amplification term based on continuously available geospatial terms instead of $V_{S30}$. The first parameter accounts for large-scale trends in amplification by using physiographic provinces originally developed by Fenneman and Johnson (1946). To account for small-scale trends in amplification, we use sediment thickness as a secondary parameter in our amplification term. We obtain sediment thickness from a high-quality regional dataset (Boyd et al., 2024) in the Atlantic and Gulf Coastal Plains, and a global dataset (Pelletier et al., 2016) for all other regions. When tested using all ground motions from earthquakes with $M > 4$ against the current NGA-East linear amplification model (Stewart et al., 2020), we observe an average reduction in the standard deviation of site-to-site terms across all periods of 25.3% using our proposed model.

As part of this study, we examine the city-scale effects of sediment thickness on site response in two CEUS cities that reside within basin structures: Memphis, Tennessee, and New York City, New York. We perform theoretical linear one-dimensional (1D) site response analyses to evaluate site response at ground-motion stations within these cities, and compare the results with the current $V_{S30}$-based NGA-East linear amplification model (Stewart et al., 2020) and the linear amplification model proposed in this study. In Memphis, which is located in the deep Mississippi Embayment, we observe high site amplifications with our proposed model, accurately predicting long-period amplification but overestimating short-period amplification. In New York City, which is located on the edge of the Atlantic Coastal Plain, there are significant variations in sediment thickness. Our proposed model has better performance at a deep site than a shallow site, highlighting the need for higher-resolution sediment thickness data in the entire CEUS and the difficulty in modeling site response at shallow sediment sites with high impedance contrasts.

# Table of Contents

# Chapter 1: Introduction

## 1.1 Organization of Report

This report is divided into four chapters to catalog and synthesize the analyses we performed. Chapter 1 explains the organization of the report, introduces background information, and provides the motivation for the study. This chapter also explores relevant datasets at different scales across the Central and Eastern United States (CEUS), aiming to summarize available datasets and assess their robustness. Chapter 2 delves into residual analysis, mixed-effects regression, and regionalization of the current NGA-East Ground Motion Models (GMMs) to develop a new linear site amplification term. This term is not scaled by the average shear-wave velocity in the upper 30 m of the subsurface ($V_{S30}$), but is instead based on physiographic-based regional adjusted provinces and regional sediment thickness datasets. Chapter 3 presents two city-scale geotechnical site response analyses, using both shear wave velocity and sediment thickness to characterize site conditions, in Memphis and New York City. Chapter 4 presents summaries, conclusions, and connections between the three previous sections. An appendix also provides city-scale geotechnical characterization data compiled as part of the project.

## 1.2 Motivation and Background

The 2023 update to the National Seismic Hazard Model (Peterson et al., 2023) led to widespread increases in seismic hazard assessments across the CEUS, with many of these increases affecting large population centers, such as New York City, Washington, D.C., Philadelphia, Memphis, and Boston. As more ground motion data becomes available in the CEUS, accurate ground motion characterization in this region has become a higher priority. Understanding the site amplification effects in the CEUS enables more accurate seismic hazard assessments, informing building codes and land-use planning to mitigate earthquake risks effectively.

The Next Generation Attenuation Models for Central & Eastern North-America (NGA-East) project provided a set of 17 median ground motion models (GMMs) (Goulet et al., 2021a) that were incorporated into the 2018 update of the U.S. National Seismic Hazard Model (NSHM) (Petersen et al., 2020). The NGA-East GMMs are applicable to hard-rock site conditions with $V_{S30}$ (time-averaged shear-wave velocity in the upper 30 m) of 3000 m/s and kappa ($\kappa$) of 0.006 s (Campbell et al., 2014; Hashash et al., 2014; Goulet et al., 2021a), and therefore do not explicitly address local site and basin effects. Ergodic site amplification models relying on $V_{S30}$ (Parker et al., 2019; Hashash et al., 2020; Stewart et al., 2020) are used to obtain ground-motion predictions for soil sites in conjunction with the hard-rock NGA-East GMMs. While $V_{S30}$ has traditionally been used as a site response variable, its effectiveness in predicting site amplification in the CEUS is more limited than in regions such as California (Hassani et al., 2016). In the NGA-East database, only 6% of the $V_{S30}$ values were measured, with the rest estimated using various proxies, including terrain-based, slope-based, and geologic-unit-based methods (Goulet et al., 2021b). This report examines and proposes amplification terms that do not rely on measured or inferred $V_{S30}$.

The geologic and tectonic settings of the CEUS are vastly different from the Western United States (WUS), with the CEUS being intracontinental, tectonically stable, and less topographically variable than the WUS. The tectonic and geologic histories of the CEUS result in large-scale structures with similar geologic and geomorphologic characteristics, such as the Atlantic Coastal Plain, the Great Plains, and the Interior Highlands. Residual analyses using the NGA-East GMMs and recorded ground motions reveal strong residual dependence on geographically defined regions within the CEUS, with additional dependence on sediment thickness. Additionally, topographic relief does not show substantial correlation with subsurface structure as observed in the WUS (Soller and Garrity, 2018) This, along with the low spatial resolution of stations and $V_{S30}$ measurements in the CEUS, makes many potential site and basin terms used in California (e.g., $V_{S30}$, $Z_{1.0}$, $Z_{2.5}$) impractical for much of the CEUS.

Geologically, many parts of the CEUS are characterized by sediments over hard rock, resulting in a strong impedance contrast and resonance-related soil amplification. Site amplification is characterized by the fundamental frequency ($f_0$) and the peak amplitude, which is related to sediment thickness, $V_{S,avg}$ (the time-averaged shear-wave velocity in the sediments) and $V_{S,bedrock}$ (the shear-wave velocity of the underlying bedrock). As a result, sediment thickness can be an effective predictor of site amplification. Recent work has focused on using sediment thickness in the Atlantic and Gulf Coastal Plains as a predictor of site amplification (Boyd et al., 2024; Gann-Phillips et al., 2024). Sediment thickness can also serve as a proxy for basin amplification. Similarly, several studies incorporate fundamental frequency ($f_0$), as an additional site proxy for stable continental regions (Hassani and Atkinson, 2016, 2018). $f_0$ can be determined from either an earthquake horizontal-to-vertical spectral ratio (HVSR) or microtremor HVSR measurement.

This work aims to use sediment thickness as a site and basin proxy to account for site amplification within large basin structures in the CEUS. This is achieved through three different sets of analyses: (1) assessment of different scale sediment thickness datasets in the CEUS; (2) residual analyses to assess CEUS GMM performance and propose a new linear amplification term based on large-scale basin proxies and sediment thickness; and (3) geotechnical site response analyses based on sediment thickness in Memphis, Tennessee, and New York City, New York, to highlight local soil amplification effects and compare ergodic site amplification models (such as the one developed in Chapter 2 and that of Stewart et al. [2020]) with theoretical one-dimensional site response analyses.

## 1.3 Sediment Thickness Datasets

This project required examining various geospatial products providing sediment thickness information, defined either as depth to bedrock or depth to basement. It is important to note the distinction between these measurements. Depth to bedrock measures the depth of unconsolidated sediments above solidified rock, which can be sedimentary or crystalline, while depth to basement includes all materials above crystalline basement, including sedimentary layers. If the bedrock is crystalline, these numbers will be similar; however, in areas where bedrock is sedimentary, basement will be much deeper than bedrock. Both datasets are valuable for identifying potential amplification, as both represent an impedance contrast.

A large-scale data search was conducted, examining regional or country-scale geotechnical databases containing sediment thickness information. This large-scale data compilation was followed by a local search into a set of major CEUS cities to better understand subsurface structures and average sediment thickness within these areas. This section will outline and describe these datasets, providing an overview and maps of the regional datasets, and a brief description of the 11 local city-scale datasets of interest. More detailed information on the city-scale geotechnical characterizations is available in Appendix A.

### 1.3.1 Regional-Scale Data

*(1) Coastal Plains: Boyd et al. (2024)*

The sediment thickness map of the U.S. Atlantic and Gulf Coastal Plains (Boyd et al., 2024), displayed in Figure 1.1, illustrates sediment thicknesses in meters across the Atlantic and Gulf Coastal Plains in the southeastern U.S. This map highlights areas where sedimentary layers are particularly thick, such as the deep sedimentary regions in southern Texas, Louisiana, and Mississippi, while the Atlantic coast generally exhibits shallower sediment layers. Notably, this map measures depth to basement, which refers to the distance from the surface to the ancient crystalline rock layer deep within the crust, distinct from the depth to bedrock.

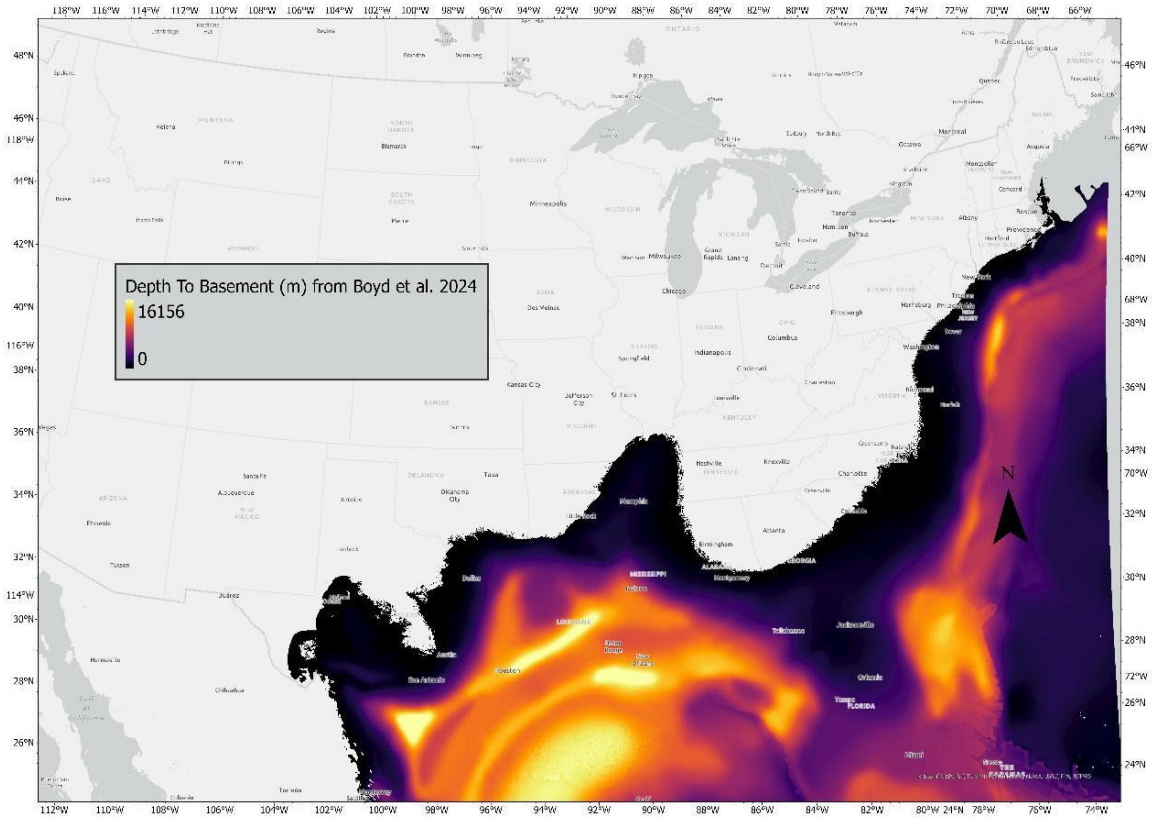


**Figure 1.1.** Depth to basement in meters from Boyd et al. (2024) for the Atlantic and Gulf Coastal Plains.

*(2) Previously Glaciated Regions: Soller and Garrity (2018)*

The Soller and Garrity (2018) dataset displayed in Figure 1.2 presents Quaternary sediment thicknesses across the previously glaciated terrain of the CEUS. Unlike the prior dataset, this measures depth to bedrock, being the distance from the surface elevation to the elevation of consolidated rock. Notably, this dataset reveals several areas with deep unconsolidated sedimentary basins that do not correspond to surface topographic changes due to the glaciation of the terrain. These deeper basins would be overlooked by the elevation-based methods more common in the WUS (Nweke et al., 2020). Some key features include large, deep sedimentary areas in Michigan, South Dakota, and Minnesota.

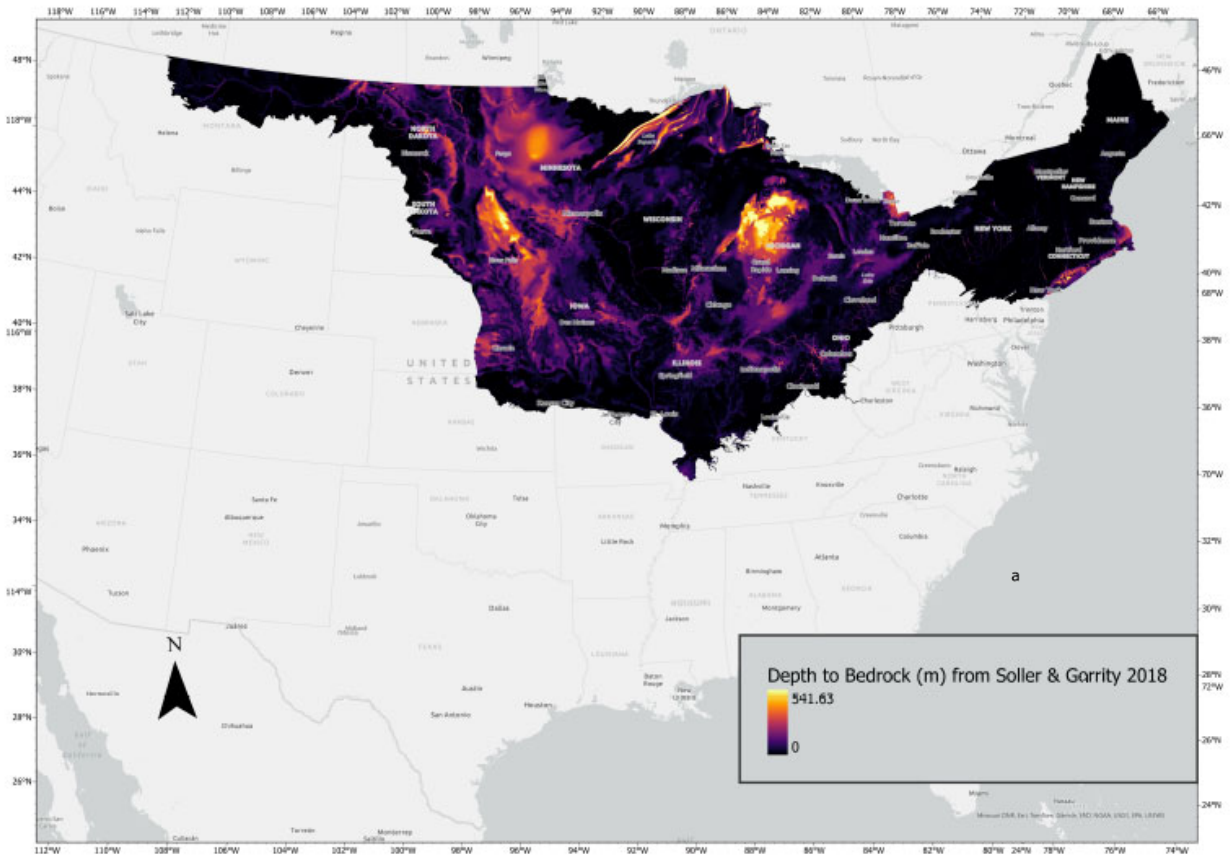


**Figure 1.2**. Depth to bedrock in meters from Soller and Garrity (2018) for previously glaciated regions in the CEUS.

*(3) Topography of the Basement-Cover Contact (the Great Unconformity): Domrois et. al. (2015)*

Figure 1.3 shows the depth to the surface of the Great Unconformity (Domrois et al., 2015), which is the depth to basement rock on the U.S. Cratonic platform. Again, it should be noted here that much of this landscape has little to no topographic relief, but has subsurface structure of varying depths due to ancient geologic and geomorphic processes, which scoured to basement had different depositional and erosional environments after. This database does not appear to indicate the same features illustrated in the depth to bedrock database by Soller and Garrity (2018).

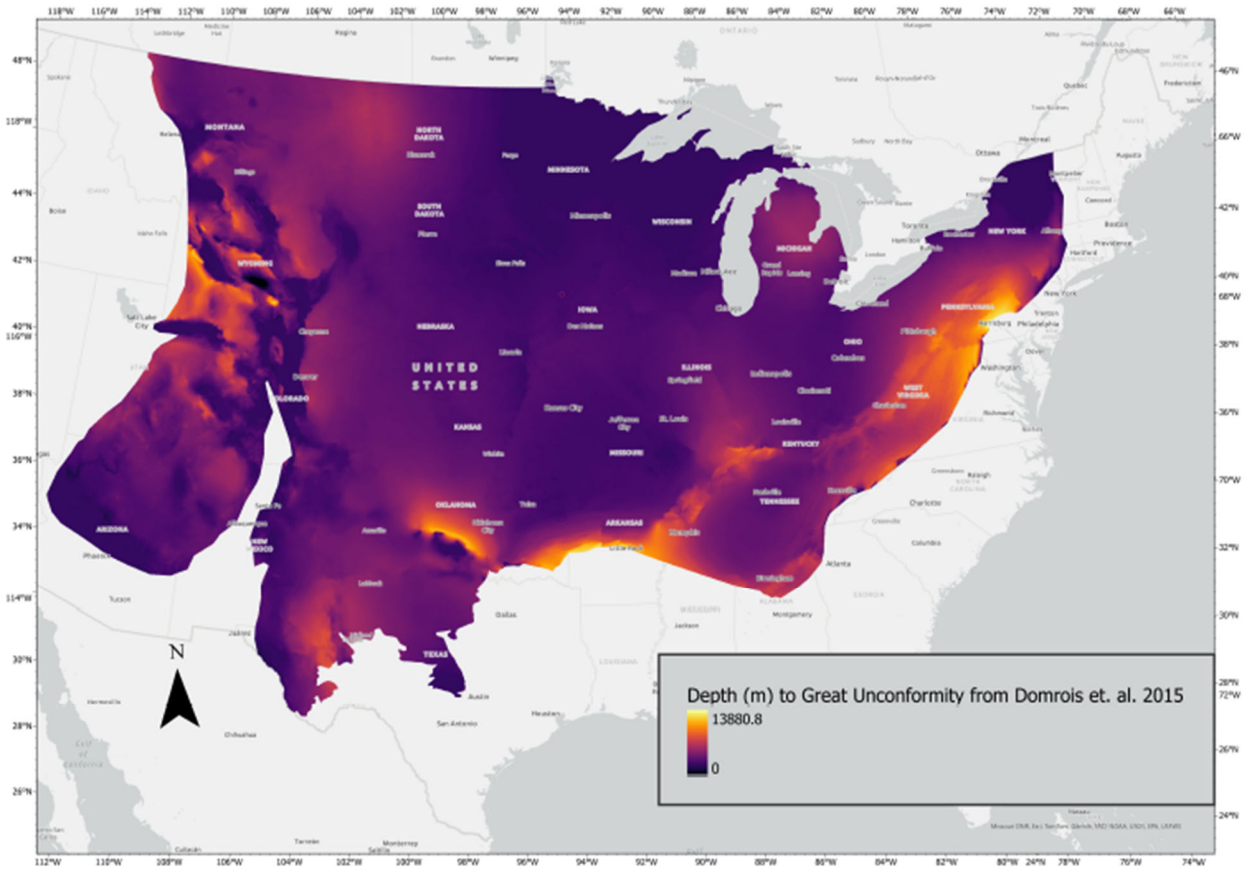


**Figure 1.3**. Depth to the Great Unconformity in meters from Domrois et al. (2015). The great unconformity is where younger sedimentary rocks overlay old Precambrian igneous or metamorphic rock. The depth to the Great Unconformity is the depth to basement.

*(4) The entire CEUS: Average soil/sediment thickness (depth to bedrock): Pelletier et al. (2016)*

The Pelletier et al. (2016) dataset, illustrated in Figure 1.4, is a global-scale dataset that shows the thickness of unconsolidated sediment. It has a spatial resolution of ~1 km, and is derived using inputs of topography, climate, and geology. This is the only sediment thickness dataset covering the entire CEUS, but the thicknesses have a high uncertainty and are capped at a maximum of 50 m depth. As a result, although this database provides an indication of sediment thickness, the variabilities of sediment thickness are not fully captured, especially for deep basins.

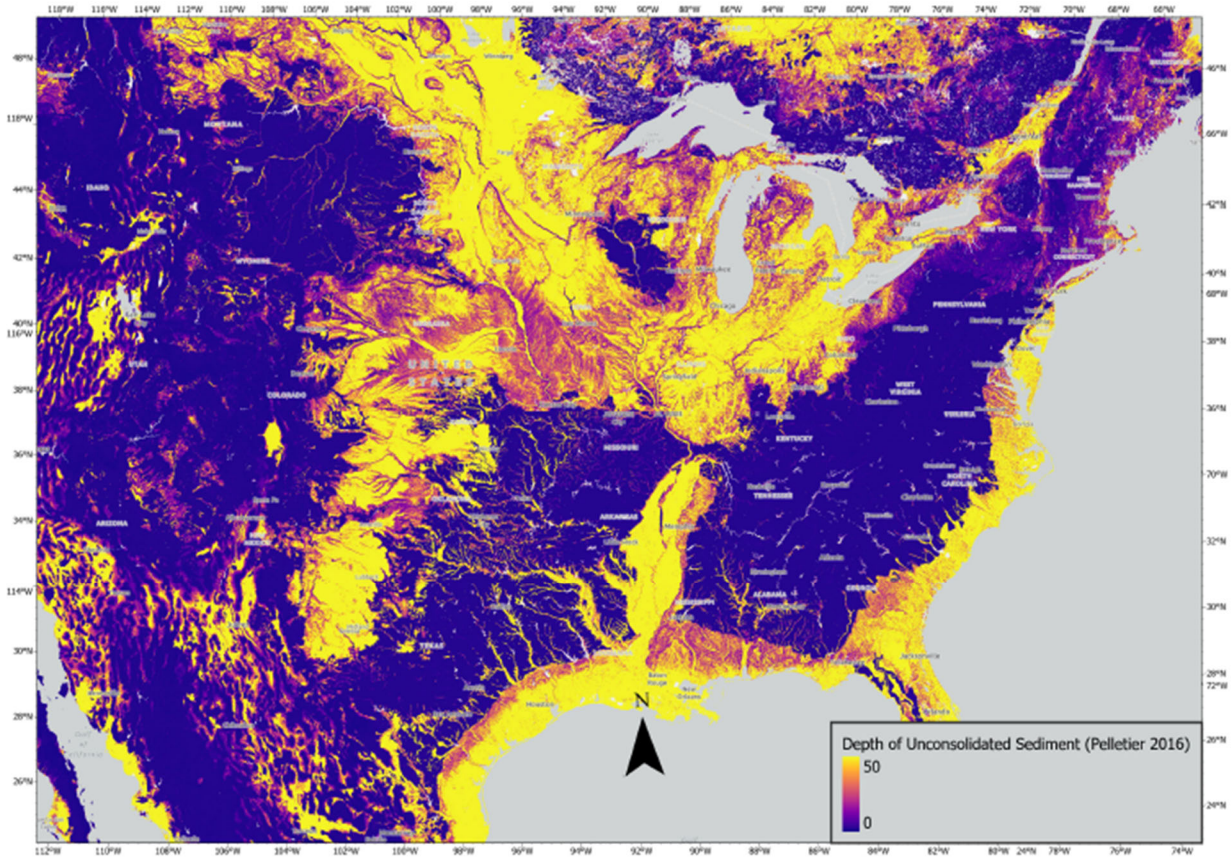


**Figure 1.4.** Depth to bedrock in meters from Pelletier et al. (2016) for the entire CEUS.

### 1.3.2 City-Scale Data

As part of this project, we compiled and analyzed depth-to-bedrock, shear-wave velocity, and other geotechnical data in a set of eleven (11) selected cities in the Central and Eastern United States (CEUS). The goal of the data compilation was to allow for more detailed seismic site response comparisons in a subset of cities; in Chapter 3, we present detailed site response analyses and comparisons for Memphis, Tennessee, and New York City, New York. For our data compilation, we selected major cities that spanned a range of geologic conditions, geotechnical profiles, and seismic hazard levels. The following eleven cities are profiled in Appendix A:

1. Boston, Massachusetts
2. Providence, Rhode Island
3. New York City, New York (further analyzed in Chapter 3)
4. Philadelphia, Pennsylvania
5. Washington, D.C.
6. Charleston, South Carolina
7. Cleveland, Ohio
8. Louisville, Kentucky
9. Chicago, Illinois
10. Saint Louis, Missouri
11. Memphis, Tennessee (further analyzed in Chapter 3)

The focus of the discussions in Appendix A is on resources that describe the geologic conditions and depth to bedrock patterns in each city. There are many cities in the CEUS that are located in sedimentary basins where the soft soil deposits and a strong soil-bedrock impedance contrast have the potential to amplify seismic waves. These sedimentary basins increase the potential for earthquake-induced damage, especially in densely populated areas. More detailed geotechnical data, at the scale of cities, allow for more site-specific characterizations of sediment depths than those from more regional models such as Boyd et al. (2024), Soller and Garrity (2018), Domrois et. al. (2015), and Pelletier et al. (2016).

There are several commonalities among the set of eleven cities we characterized. New York City, Philadelphia, and Washington, D.C., are located on the edge of the Atlantic Coastal Plain, and have dipping bedrock surfaces that deepen as the coastal plain sediments thicken. Boston and Providence are both in local sedimentary basins in New England with varying depths to bedrock from 0 to 80 m. Charleston and Memphis are located within the Atlantic and Gulf Coastal Plains with much less variation in bedrock depths than the other cities; Charleston sits atop approximately 800 to 900 m of Atlantic Coastal Plain sediments, and Memphis sits atop approximately 1100 to 1200 m of Mississippi Embayment sediments. Both cities are also located in areas of high seismic hazards, and have been extensively characterized from a geotechnical perspective. Further inland, the cities of Louisville and Saint Louis are both located along major rivers near the extent of maximum glacial advance during the last Ice Age; both have varying levels of bedrock, up to a maximum of approximately 40 to 50 m, which are greatest beneath the floodplains of the rivers. Further north, Chicago has a varying bedrock surface that approaches a maximum of 45 m in some locations; and Cleveland sits atop a deep narrow sedimentary basin up to approximately 200 m in thickness. This geotechnical data compilation, further profiled in Appendix A, could be used to validate the broader-scale sediment thickness models, update ergodic site amplification models, and perform more site-specific ground response analyses, especially in locations where extensive site characterization data are available.

# Chapter 2: Residual Analysis to Assess CEUS GMM Performance and Propose a New Linear Amplification Term Based on Large-Scale Basin Proxies and Sediment Thickness

Chapter 2 will focus on residual analysis using current CEUS ground motion models and amplification terms, as well as the development and testing of a linear amplification term based on sediment thickness and physiographic province. Ellie Meyer and Laurie Baise at Tufts University led this effort. The goal of this chapter is to highlight the regional trends in site-to-site terms and account for regional amplification in the linear term without relying on inferred $V_{S30}$ from slope or geology.

## 2.1 Datasets

### 2.1.1 Ground-Motion database

We combined two different CEUS ground motion datasets for this study: (1) the publicly available NGA-East dataset from the Pacific Earthquake Engineering Research Center (PEER) (Goulet et al., 2021b), and (2) the Center for Engineering Strong Motion Data (CESMD) database for CEUS ground motions from 2010 to 2020 (Thompson et al., 2023). To ensure accurate, repeatable characterization of site-to-site terms, the databases were filtered to remove recordings from outside the CEUS and beyond the attenuation boundary with the WUS; to remove recordings flagged as outliers; and to remove recordings from stations with two recordings or less. Additionally, we used a maximum rupture distance of 1,000 kilometers, to avoid bias in strong ground-motion prediction at distances greater than 1,000 kilometers. For our final database, we used 38,088 ground motions recorded at 2,114 stations during 378 earthquakes, with a magnitude range of 3 to 5.8, shown in Figure 2.1.

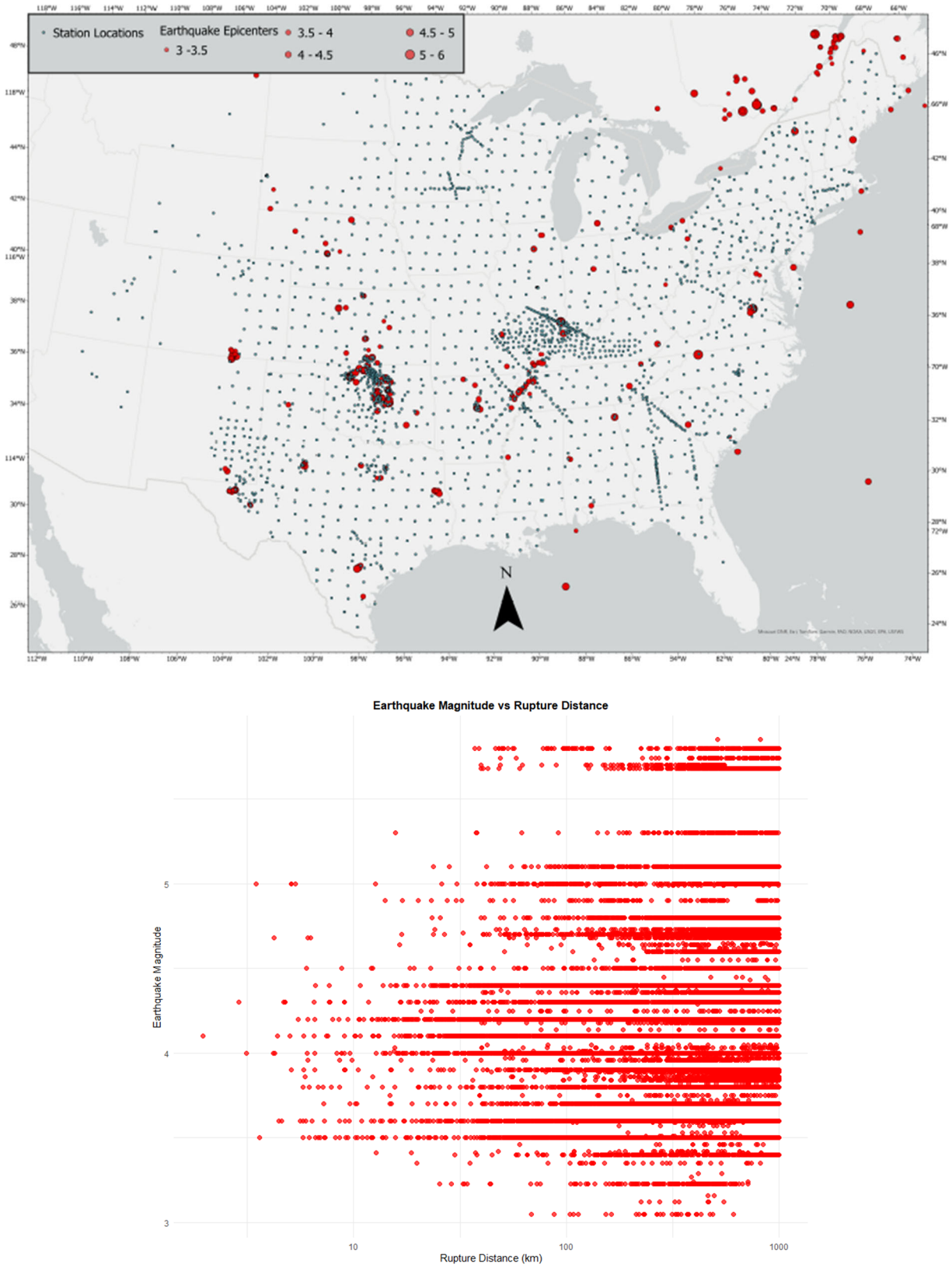


**Figure 2.1.** Top: Location of earthquakes by magnitude and stations used in the database in the CEUS. Bottom: Distribution of magnitude and rupture distance of each ground motion recording used in this analysis.

### 2.1.2 Continuous Geospatial Terms

We define continuous geospatial terms as parameters derived from collected data related to topography, geology, and crustal properties. These parameters are used as proxies for site amplification at a high spatial resolution and are available at any site without the need for site-specific measurements. These geospatial terms include continuous terms, such as elevation, sediment thickness and roughness; and categorical terms, such as surficial geology. We extracted the geospatial terms for each station in the combined ground motion database where the terms were available. In this study, sediment thickness and physiographic provinces are explored in depth as predictors of amplification. All the variables are listed in Table 2.1 with a description of the variable, and an identification of the characteristic(s) for which it serves as a proxy (geology, topography, basin, or basin edge).

**Table 2.1.** Description and sources of geospatial variables, including the characteristics for which each variable serves as a proxy.

| Variable | Variable Description | Geology | Topo-graphy | Basin | Basin Edge | Classification | Source(s) |
|---|---|---|---|---|---|---|---|
| $V_{S30}$ | Shear wave velocity in the upper 30 meters of the crust. "Preferred Vs30" was used for NGA-East Data; estimated from Heath et al. (2020) for CESMD | | | | | Continuous | Thompson et al. (2023)<br>Goulet et al. (2021a) |
| Elevation (m) | Elevation above sea level pulled from 90-m-resolution DEM | | ● | | ● | Continuous | Jarvis et al. (2008) |
| Curvature | Mean curvature calculated on 90-m DEM. Average of minimum and maximum curvature | | ● | ● | | Continuous | Derived using Jarvis et al. (2008) |
| Topographic Slope (degree) | Slope calculated in GIS using a 90-m DEM | | ● | ● | ● | Continuous | Derived using Jarvis et al. (2008) |
| Roughness | Roughness calculated as standard deviation of slope at different moving windows: 3x3, 33x33, and 101x101. These changes in scales capture the roughness at different spatial resolutions. | | ● | ● | ● | Continuous | Derived using Jarvis et al. (2008) |
| Topographic Position Index | Method of terrain classification which measures the elevation of a cell in comparison to the neighboring cells | | ● | ● | | Continuous | Derived using Jarvis et al. (2008) |
| Surficial Materials | Materials at the surface of the Conterminous United States: transported sediments, unconsolidated/residual material developed in bedrock, and bedrock. This dataset also included the approximate thickness of these units as categories. | ● | | | | Categorical | Soller et al. (2009) |
| Geologic Unit | Geologic unit grouped into 31 subgroups of igneous, metamorphic, and sedimentary rock. This dataset also included Critical Minerals Mapping Initiative (CMMI) class. | ● | | | | Categorical | McCafferty et al. (2023) |
| Land cover | 2016 map of land cover from USGS with 95 different categories | | ● | ● | | Categorical | Yang et al. 2018 |
| Sediment Thickness* | Four different datasets defining sediment thickness in the CEUS, as described in Section 1.3.1 | | | ● | ● | Continuous | Boyd et al. (2024)<br>Soller and Garrity (2018)<br>Pelletier et al. (2016)<br>Domrois et al. (2015) |
| Physiographic Divisions* | Large areas of the continental United States that provide a proxy for large scale geomorphology, geology, and crustal structure | ● | ● | | | Categorical | Fenneman and Johnson (1946) |

### 2.1.3 Sediment Thickness

Sediment thickness was of particular interest as a geospatial term, as the work of Boyd et al. (2024) and Akhani et al. (2024) has demonstrated that sediment thickness is an effective parameter for predicting soil amplification in the CEUS. Currently, high-resolution sediment thickness data is not available in the entire CEUS. As discussed, definitions of sediment thickness differ between different studies, with some measuring to bedrock (Pelletier et al., 2016) and some measuring to basement (Boyd et al., 2024). This leads to difficulty in combining sediment thickness datasets.

### 2.1.4 Physiographic Provinces

Physiographic divisions are large areas of the Continental United States that provide a proxy for large-scale geomorphology, geology, and crustal structure. The U.S. physiographic provinces were originally produced by Fenneman and Johnson (1946), and have been used as regional divisions in geologic research (Porter et al. 2016) and hydrological research studies (Sofia et al., 2020). More recently, physiographic provinces were examined with station corrections for magnitude energy calculations (Bindi et al., 2024), showing province dependence on station-specific magnitude residuals.

Fenneman and Johnson (1946) demarcated eight (8) broad divisions of the United States; these divisions are subdivided into 25 provinces, and then subdivided again into 82 different sections. These partitions were accomplished by examining the underlying geologic structures, the terrain texture, and the present rock type. In this study, we use adjusted versions of the Fenneman and Johnson (1946) provinces as geospatial terms for our amplification models. We adjust the provinces by breaking certain provinces into sections, to take advantage of geologic and topographic differences within sections that are not captured by the broader provinces. We use the adjusted provinces rather than the individual 82 sections, because using too many subdivisions could lead to model overfitting when they are sampled by a limited number of stations per section. To obtain the adjusted provinces, we split provinces that contain more than 100 stations into sections within the province. To avoid potential model overfitting, we make sure there are at least five stations per adjusted province. The provinces with more than 100 recordings are located in the Atlantic Coastal Plain, the Central Lowlands, and the Great Plains. The original and final adjusted physiographic provinces are shown in Figures 2.2 and 2.3, respectively.

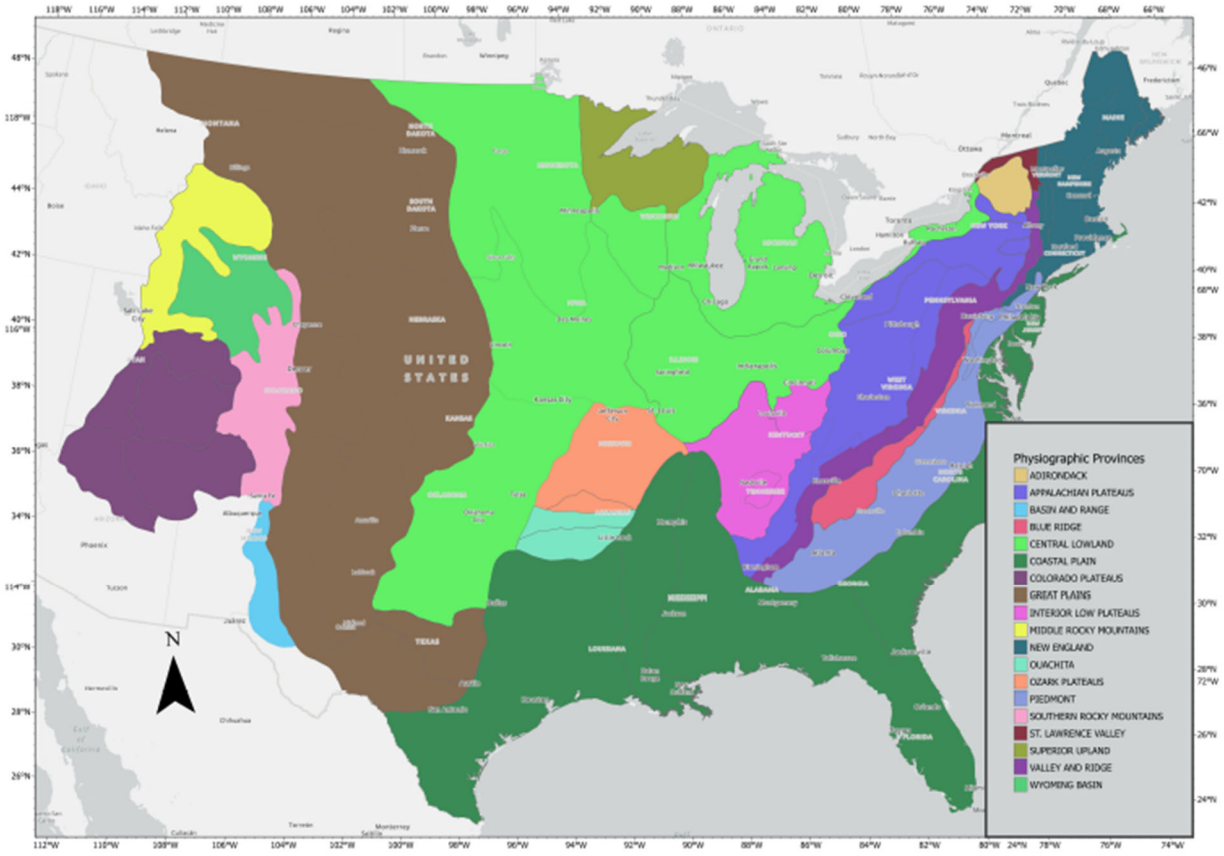


**Figure 2.2.** Physiographic provinces of the CEUS from Fenneman and Johnson (1946).

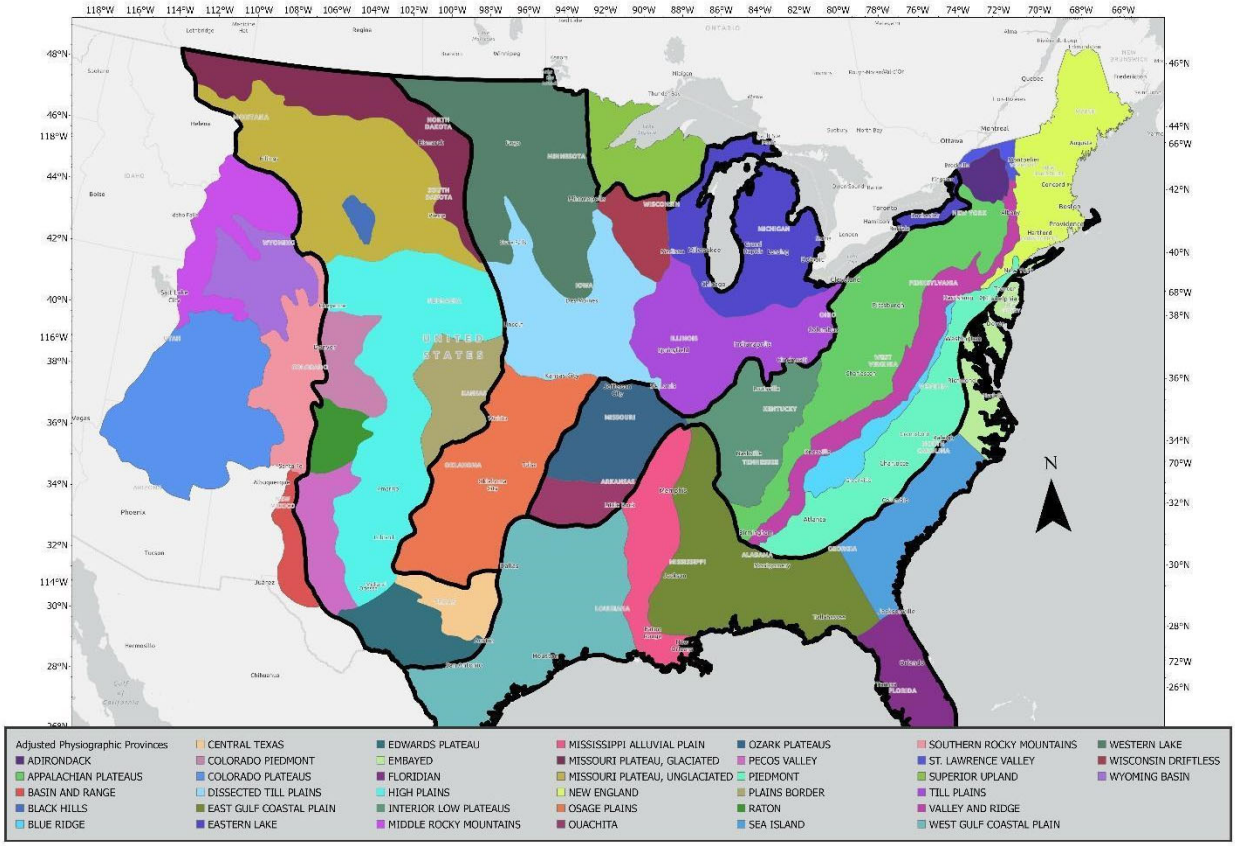


**Figure 2.3.** Adjusted physiographic provinces of the CEUS, obtained by updating the categories of Fenneman and Johnson (1946). We adjusted the Atlantic Coastal Plain, the Central Lowlands, and the Great Plain provinces by splitting them into sections, which are outlined in black.

## 2.2 Methodology

### 2.2.1 Site-to-Site Terms and Amplification Terms

We compared recordings from our ground-motion database to model predictions, yielding ground-motion model residuals. The model predictions were obtained from the 17 NGA-East GMMs (Goulet et al., 2021a), which produce a weighted median, called the central branch, as the median prediction. The hard-rock ground-motion model assumes a bedrock reference condition of $V_{S30}$ = 3000 m/s. Ground-motion predictions for the desired $V_{S30}$ are obtained by using the Stewart et al. (2020) linear amplification model (based on $V_{S30}$), and the Hashash et al. (2020) nonlinear amplification model, also based on $V_{S30}$. Because the NGA-East GMMs only offer predictions for magnitudes of 4 and greater, we followed the approach of Boyd et al. (2024) to obtain predictions for earthquakes having magnitudes 3 to 4, greatly expanding the available ground-motion dataset. We used the Modified Akima Interpolation in MATLAB (Mathworks, 2023) using rupture distance, magnitude, and period (Boyd et al., 2024). We define the residuals as the natural logarithm of the observed ground motion minus the natural logarithm of the predicted ground motion from the GMM central branch and amplification model, shown in Equation 2.1:

$$\delta_{\{ijk\}} = \ln\left(Y_{\{ij\}}\right) - \ln\left[\mu_{\left(M_i,\left(R_{\{rup\}}\right)_{\{ij\}},V_{S30}=3000\right)}\right] + F_{Vs30}\,, \tag{2.1}$$

where $Y_{\{ij\}}$ is the recorded ground motion from event *i* at station *j*, $\mu$ is the central branch prediction using the magnitude *M* and rupture distance $R_{rup}$ from the recording, and $F_{Vs30}$ is the amplification term, which includes the linear amplification ($F_{linear}$) and nonlinear amplification ($F_{nonlinear}$) from Stewart et al. (2020) and Hashash et al. (2020), respectively.

We employ mixed-effects regression (Abrahamson and Youngs, 1992) to decompose our model residuals into overall bias (*c)*, event term ($\delta E_i$), site-to-site term ($\delta S2S_j$), and remaining residual ($\varepsilon_{ij}$), as shown in Equation 2.2:

$$\delta_{\{ijk\}} = c + \delta E_i + \delta S2S_j + \varepsilon_{ij}\,. \tag{2.2}$$

In this decomposition, the event term represents the portion of the residual attributed to the event, and the site-to-site term represents the portion of the residual attributed to the site. We are interested in the site-to-site term, as it shows us which stations are systematically over or under-predicting ground motion using the current GMMs and amplification terms. We performed this calculation for spectral acceleration (SA) across 21 spectral periods, peak ground acceleration (PGA), and peak ground velocity (PGV) to compute the site-to-site term for each station at each period. These site-to-site terms exhibit noticeable regional patterns, as shown in Appendix B for SA at periods of 0.1 s, 1 s, and 3 s, as well as for PGA.

We aim to replace the linear term scaled on $V_{S30}$ with our geospatial-based linear amplification model. Therefore, we add the linear amplification term $F_{lin}$ from Stewart et al. (2020) at each station *j* to our site-to-site terms, giving us the full linear amplification $A_j$ attributed to each station, shown in Equation 2.3:

$$A_j = \delta S2S_j + F_{lin,j} . \quad (2.3)$$

We examined these full amplification terms $A_j$ with our extracted values for our geospatial terms (including sediment thickness) and our physiographic divisions and sections, using the amplification term $A_j$ as the target for our amplification model.

### 2.2.2 Site Parameter Evaluation

The correlation matrices for $A_j$ at each period and our continuous geospatial parameters are shown in Figures 2.4 through 2.7: the entire CEUS in Figure 2.4, the Coastal Plain in Figure 2.5, previously glaciated regions in Figure 2.6, and areas captured by the Great Uncomformity dataset in Figure 2.7. We used sediment thickness from Boyd et al. (2024) for the Coastal Plain, Soller and Garrity (2018) for previously glaciated regions, and Domrois et al. (2015) for the Great Unconformity dataset. All three regions, as well as the entire CEUS, showed similar patterns for some variables, with topographic position index (TPI) and curvature having little to no correlation with any amplification terms. In the entire CEUS, roughness (at three different scales) and topographic slope exhibit negative correlations with amplification, having stronger negative correlations in general as period increases. The same pattern is seen in the glaciated terrain region and extent of the Great Unconformity. For the Coastal Plain region, roughness and slope have weak positive correlations at short periods, which decrease with period until they become moderately negative at longer periods. $V_{S30}$ follows a similar pattern to roughness for each region, showing the least correlation in the Coastal Plain. Sediment thickness in the Coastal Plain has a strong negative correlation at shorter periods, becoming moderately positive at long periods. In the previously glaciated terrain, sediment thickness is moderately correlated at all periods. The correlation pattern in areas captured within the Great Unconformity dataset shows moderate negative correlation at short periods, increasing to weak positive correlation at longer periods. The average sediment thickness from Pelletier et al. (2016) is positively correlated with all period amplification terms in the entire CEUS, in the glaciated terrain, and in the extent of the Great Unconformity, as shown in Figures 2.6 and 2.7. For the Coastal Plain, the Pelletier et al. (2016) dataset shows weak negative correlation at shorter periods and weak positive amplification at longer periods, becoming moderately positive from 3 s to 10 s.

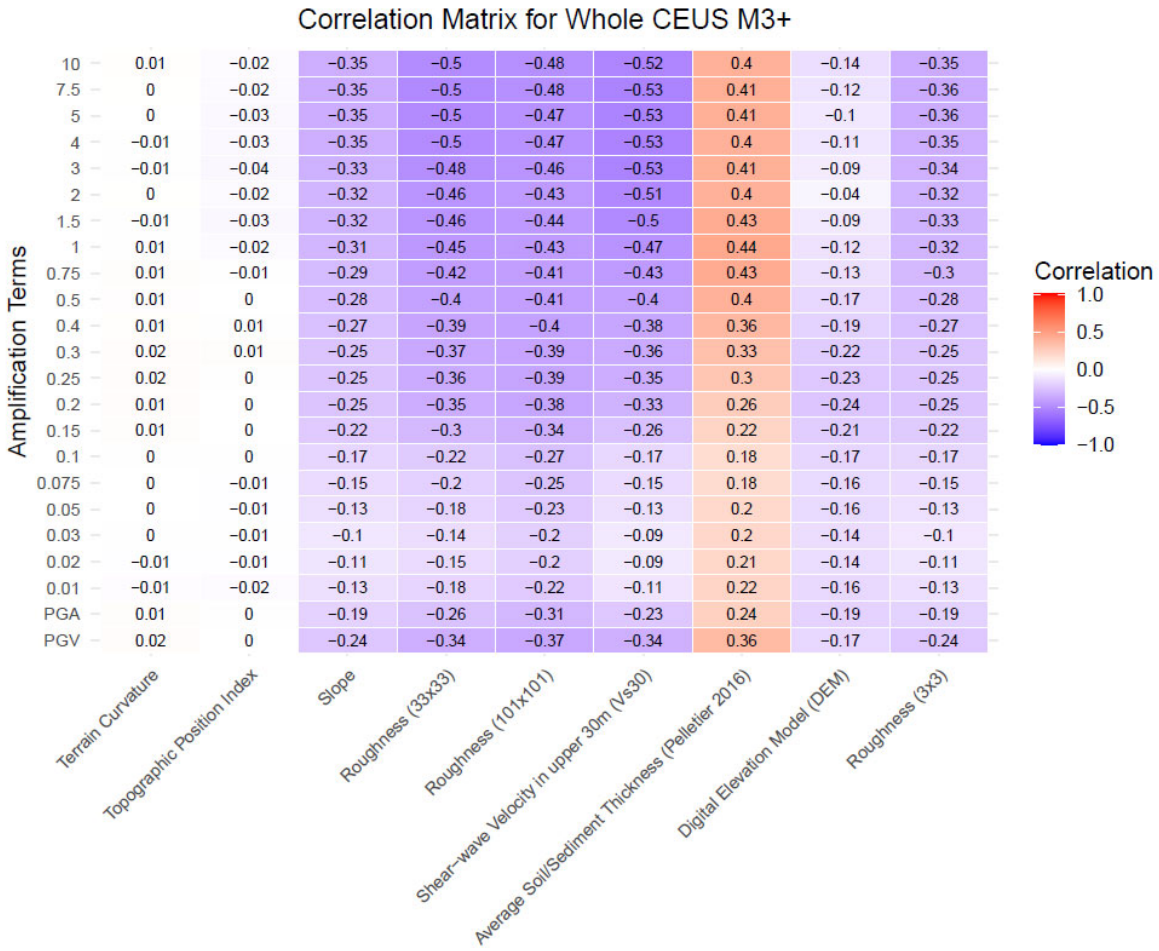


**Figure 2.4.** Correlation matrix between amplification terms across the entire CEUS and continuous geospatial predictors from Table 2.1, including depth to bedrock from Pelletier et al. (2016).

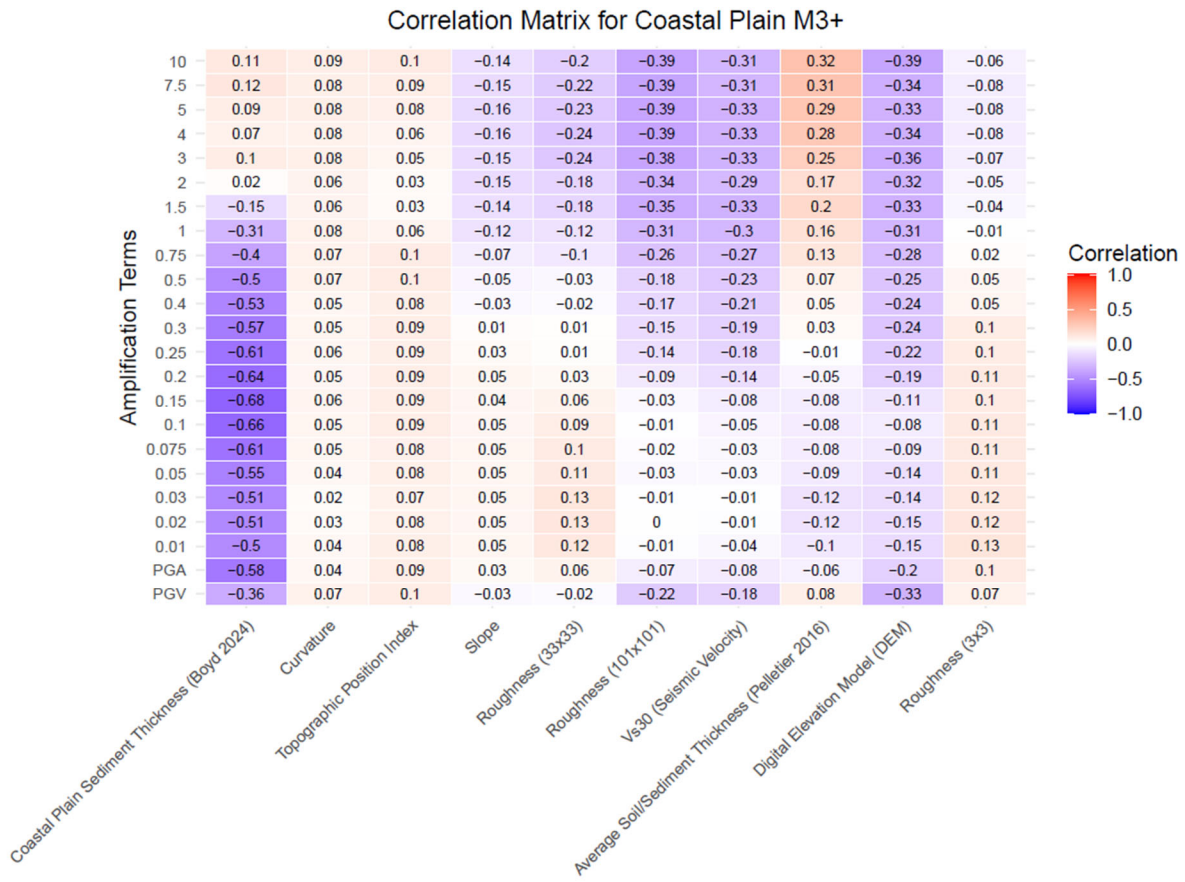


**Figure 2.5.** Correlation matrix between amplification terms across the Coastal Plain, including depth to basement (Boyd et al., 2024), depth to bedrock (Pelletier et al., 2016), and continuous geospatial predictors from Table 2.1.

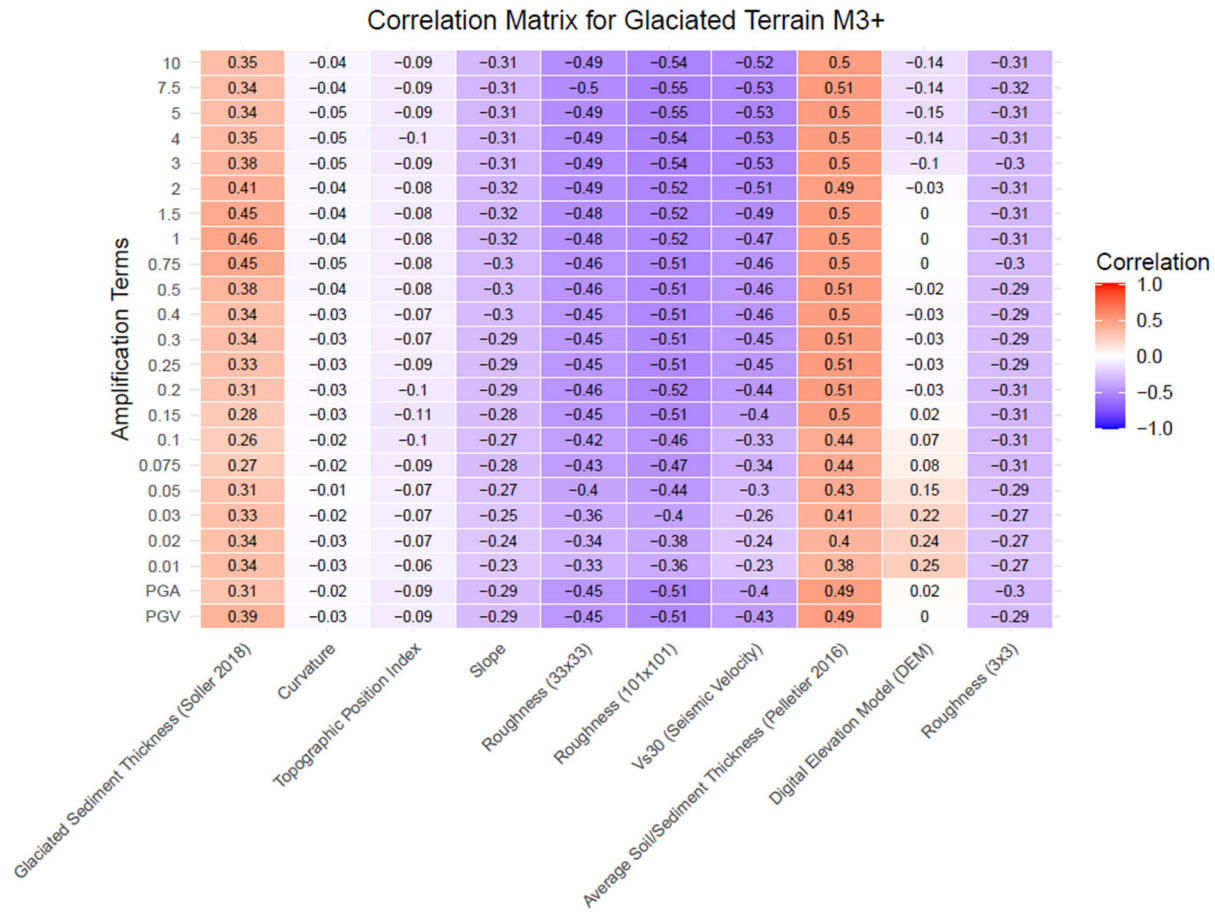


**Figure 2.6.** Correlation matrix between amplification terms across previously glaciated terrain, including regional depth to bedrock (Soller and Garrity, 2018), global depth to bedrock (Pelletier et al., 2016), and continuous geospatial predictors from Table 2.1.

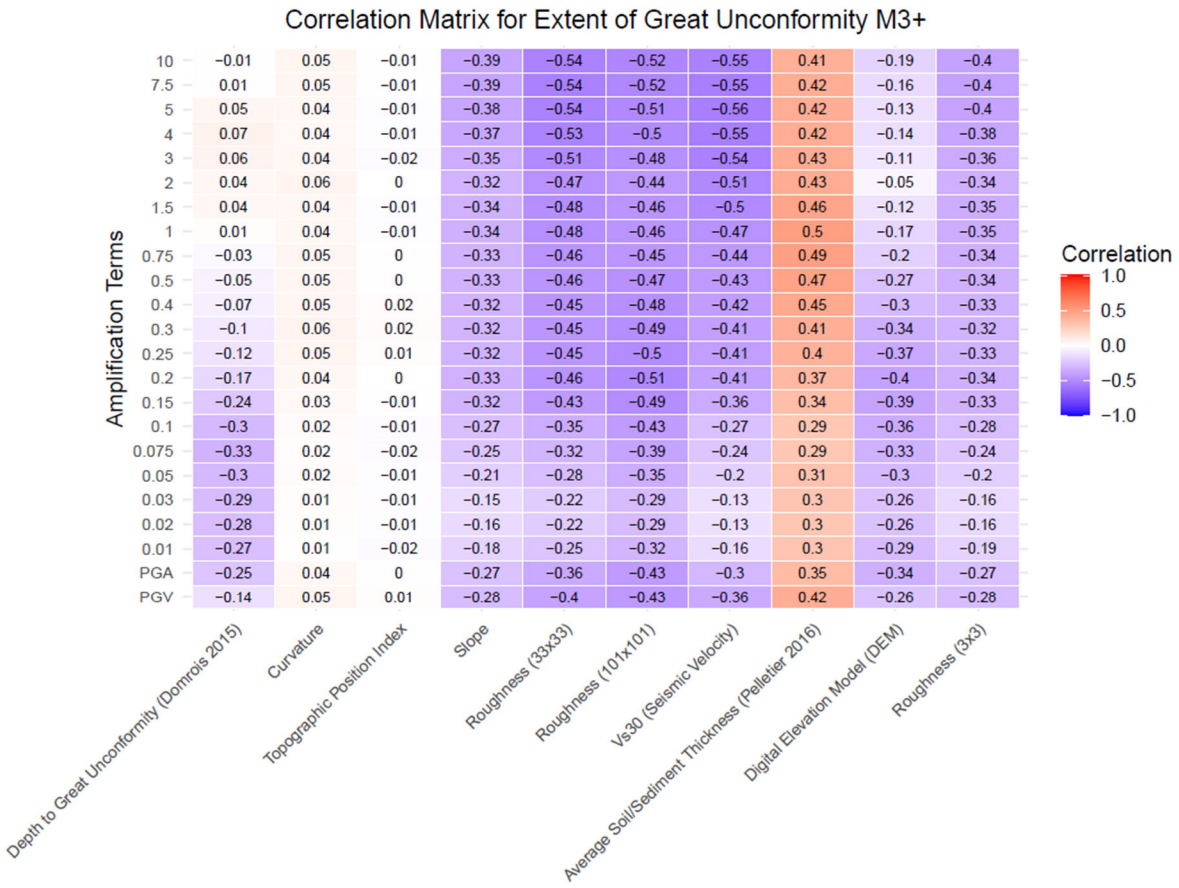


**Figure 2.7.** Correlation matrix between amplification terms across the extent of the Great Unconformity, including depth to basement (Domrois et al., 2015), depth to bedrock (Pelletier et al., 2016), and continuous geospatial predictors from Table 2.1.

Using the Analysis of Variance (ANOVA) test, we also examined the correlation between the linear site amplification term $A_j$ and categorical spatial variables, such as geology and land cover. We tested each of the categorical variables listed in Table 2.1, as well as some variables within the datasets, such as Critical Minerals Mapping Initiative (CMMI) class from the Geologic Unit map (McCafferty et al., 2023) and approximate, categorical, sediment thickness from the surficial materials map (Soller et al., 2009). The surficial materials map also included minimum and maximum geologic age, as well as an estimate of geologic age, all of which are categorical variables representing geologic time periods we also tested. For ANOVA testing, eta-squared ($\eta^2$) is a measure of how much of the total variance is explained by group membership. A high eta-squared ($\eta^2$) means that group membership is adequately explaining the variance. In Figure 2.8, we see that adjusted province and section both show higher eta-squared across all periods. Because adjusted province and section share many of the same divisions, we should see a similar pattern. Surficial materials, divisions, and provinces have moderate eta-squared values across all periods, with division and province having higher values at long periods, and surficial materials showing higher values at shorter periods.

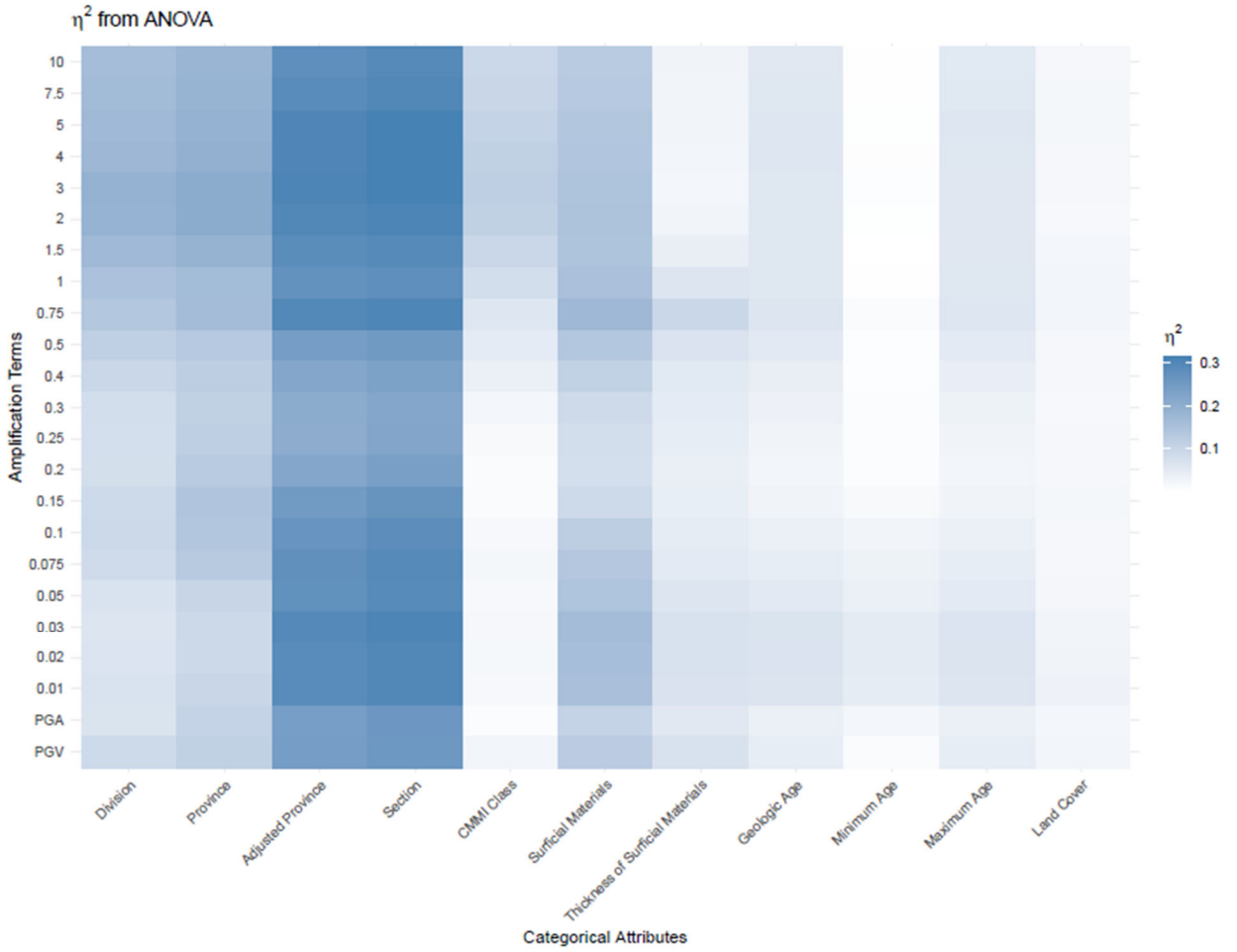


**Figure 2.8.** Eta-squared ($\eta^2$) for amplification terms $A_j$ and categorical predictors (Table 2.1) from ANOVA testing.

### 2.2.3 Multiple Linear Regression with 5-Fold Cross Validation

The amplification terms ($A_j$) were used as the dependent variable in a multiple linear regression with the continuous geospatial terms, sediment thicknesses, and physiographic provinces/sections as predictors. We followed the functional form of Equation 2.4, where $\alpha$ is the intercept term, $\beta_i$ is the regression coefficient, $X_i$ is a predictor variable, and $\varepsilon_j$ is the remaining residual.

$$A_j = \alpha + \beta_1 X_1 + \beta_2 X_2 + \cdots + \beta_n X_n + \varepsilon_j \, . \quad (2.4)$$

We use k-fold cross validation with five folds to train and test our models. The stations are randomly split into five groups. For each set of predictors tested, the model was fit to the data five times, leaving a different randomly selected group of stations out each time. The model was then tested on the left-out group for each of the five model fits, resulting in five root mean square error (RMSE) values. These five RMSE values are averaged for each of the models at each period, to use in a comparison with the other models.

### 2.2.4 Regionalization

The various sediment thickness datasets show moderate correlation with period-specific amplification within the region of available data (Figures 2.4 through 2.7). However, the sediment thickness from Domrois et al. (2015) for the extent of the Great Unconformity showed less promise in correlation versus the continuously available Pelletier et al. (2016) dataset (Figure 2.7). Additionally, the Pelletier et al. (2016) dataset showed better correlation with amplification in the glaciated terrain across all periods compared to the Soller and Garrity (2018) dataset (Figure 2.6). With this in mind, and the goal of a simple, usable model, we regionalize our model into two different areas: the Atlantic and Gulf Coastal Plains, and the northern CEUS. The Coastal Plain subdivision takes advantage of the high-quality sediment thickness dataset available for this region (Boyd et al., 2024). For all regions outside of the Coastal Plain as mapped by Boyd et al. (2024), we use the global Pelletier et al. (2016) dataset for sediment thickness because it displayed stronger correlations than the other regional sediment thickness models.

### 2.2.5 Model Testing

#### *One-Parameter Models:*

We first tested all the potential one-parameter models to determine the best single predictor of amplification term across SA at all 21 periods, PGA, and PGV. These models were fitted and tested for each of the two regions using region-specific sediment thickness data, and for the entire CEUS with the non-regionally specific geospatial terms. Using the 5-fold validation technique described, we evaluated each single-parameter model using the average RMSE of the left-out group. The results for the entire CEUS are shown in Figure 2.9, and results for the Coastal Plain and northern CEUS region are shown in Figures 2.10 and 2.11, respectively. Tables 2.2 through 2.4 provide the corresponding RMSE values in numerical form.

**Whole CEUS:**

Throughout the whole CEUS (Figure 2.9 and Table 2.2), the Adjusted Physiographic Province performs the best as a single predictor across all periods with the lowest average RMSE. Digital elevation model (DEM)-derived predictors and categorical predictors varied across periods, with categorical predictors having lower RMSE at lower periods. Roughness is the best performing geospatial variable. $V_{S30}$ has a lower RMSE for longer periods, but has a relatively higher RMSE for SA at short periods, PGA, and PGV. The model using adjusted physiographic province had an average RMSE 18.2% lower than the average RMSE using $V_{S30}$.

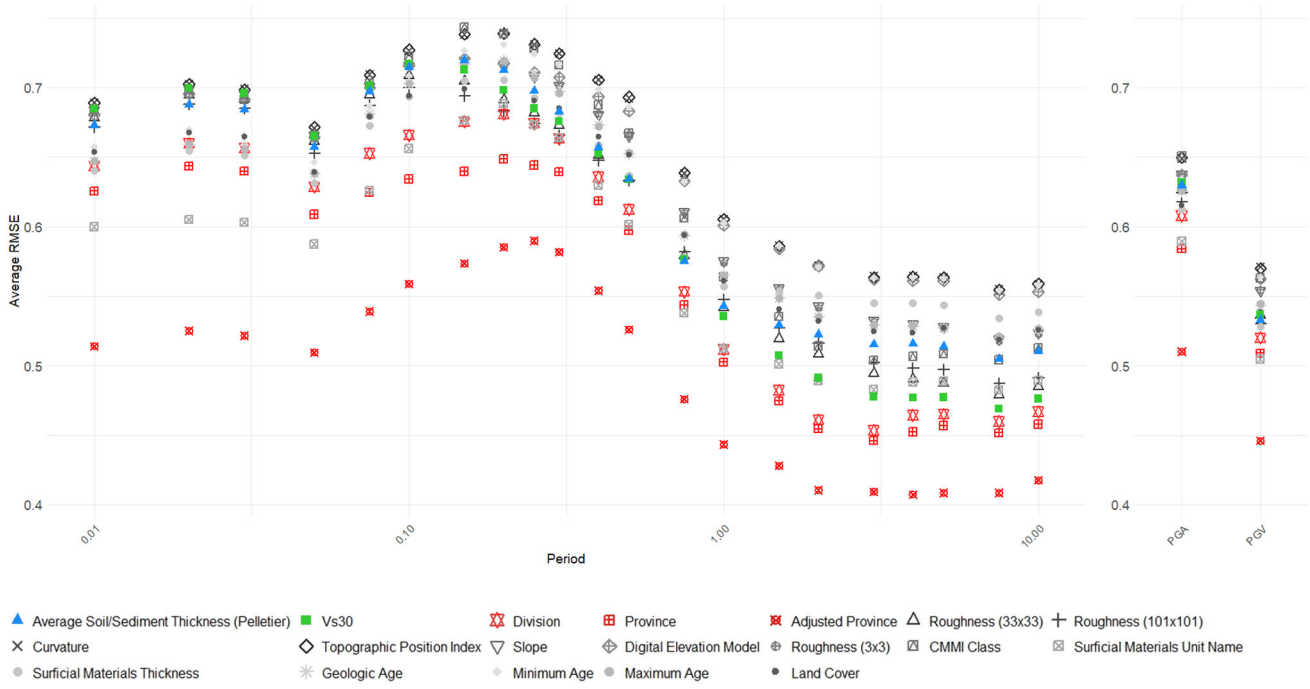


**Figure 2.9**. Average RMSE of the left-out group for each period by predictor for the entire CEUS. Symbols indicate predictors, and colors indicate relevant predictor group with red being physiographic province, green being $V_{S30}$, and blue representing sediment thickness by Pelletier et al. (2016). Other predictors are gray and distinguishable by symbol.

**Table 2.2**. Average RMSE of the left-out group across all periods by predictor for the entire CEUS.

| **Predictors** | **Average RMSE** |
|---|---|
| Adjusted Province | 0.493 |
| Province | 0.561 |
| Surficial Materials Unit Name | 0.573 |
| Division | 0.578 |
| $V_{S30}$ | 0.603 |
| Roughness (101x101) | 0.603 |
| Roughness (33x33) | 0.605 |
| Land Cover | 0.612 |
| Surficial Materials Thickness | 0.613 |
| Average Sediment Thickness (Pelletier et al., 2016) | 0.614 |
| Maximum Age | 0.617 |
| Geologic Age | 0.617 |
| CMMI Class | 0.627 |
| Roughness (3x3) | 0.628 |
| Slope | 0.629 |
| Minimum Age | 0.640 |
| Digital Elevation Model | 0.642 |
| Topographic Position Index | 0.650 |
| Curvature | 0.650 |

**Coastal Plain:**

In the Coastal Plain region (Figure 2.10 and Table 2.3), the Adjusted Physiographic Province also performs the best as a single predictor across the majority of periods with the lowest average RMSE. However, the Boyd et al. (2024) sediment thickness (depth to basement) has a lower RMSE across periods from 0.1 seconds to 0.5 seconds. The model using Adjusted Physiographic Province in the Coastal Plain had an average RMSE 17% lower than the average RMSE using $V_{S30}$.

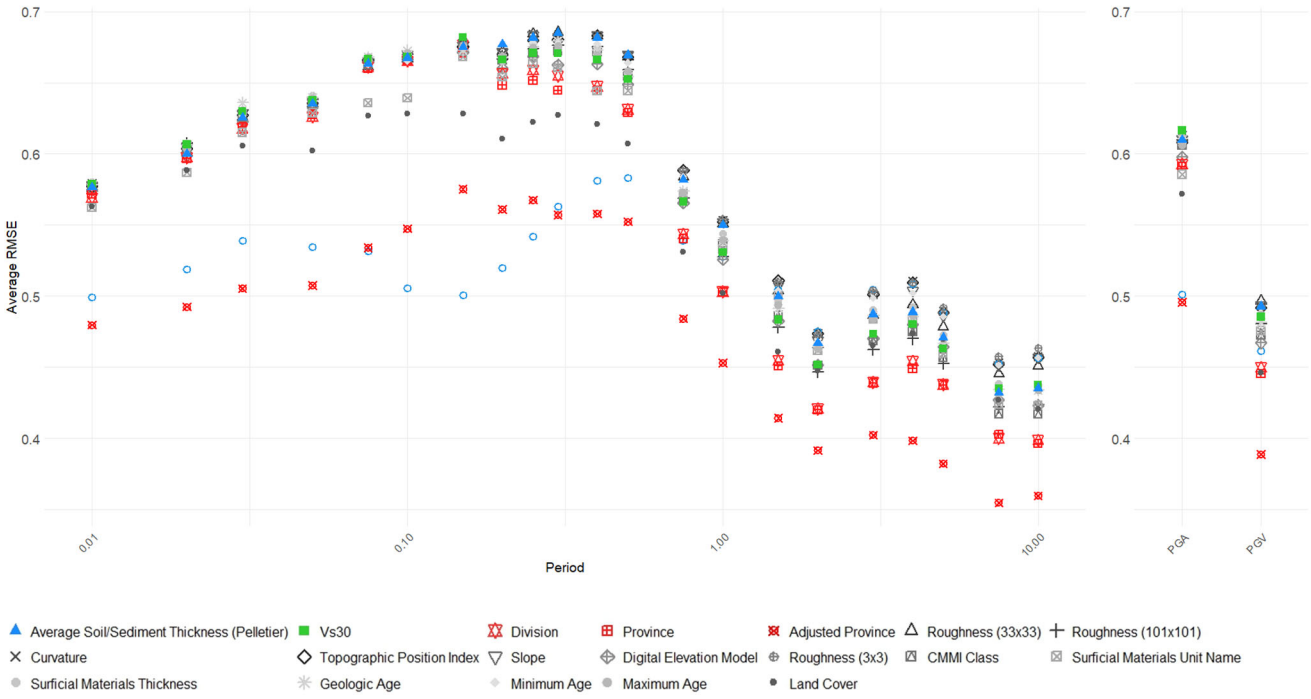


**Figure 2.10**. Average RMSE of the left-out group for each period by predictor for the Coastal Plain. Symbols indicate predictors, and colors indicate relevant predictor group with red being physiographic province, green being $V_{S30,}$ and blue representing sediment thickness by Pelletier et al. (2016) and Boyd et al. (2024). Other predictors are grey and distinguishable by symbol.

**Table 2.3.** Average RMSE of the left-out group across all periods by predictor for the Coastal Plain.

| **Predictors** | **Average RMSE** |
|---|---|
| Adjusted Province | 0.477 |
| Depth to Basement (Boyd et al., 2024) | 0.515 |
| Land Cover | 0.546 |
| Province | 0.552 |
| Division | 0.555 |
| Surficial Materials Unit Name | 0.565 |
| Digital Elevation Model | 0.569 |
| CMMI Class | 0.571 |
| Roughness (101x101) | 0.572 |
| $V_{S30}$ | 0.575 |
| Maximum Age | 0.577 |
| Geologic Age | 0.578 |
| Surficial Materials Thickness | 0.579 |
| Average Sediment Thickness (Pelletier et al., 2016) | 0.581 |
| Roughness (33x33) | 0.583 |
| Minimum Age | 0.583 |
| Roughness (3x3) | 0.585 |
| Topographic Position Index | 0.585 |
| Slope | 0.586 |
| Curvature | 0.587 |

**Northern CEUS:**

In the northern CEUS (Figure 2.11 and Table 2.4), all the physiographic province-based predictors work well, due to the similarity between the provinces, adjusted provinces, and divisions within this region. Roughness and average soil/sediment thickness from Pelletier et al. (2016) are the optimal geospatial variables. The model using Adjusted Physiographic Province in the northern region had an average RMSE 17.4% lower than the average RMSE using $V_{S30}$.

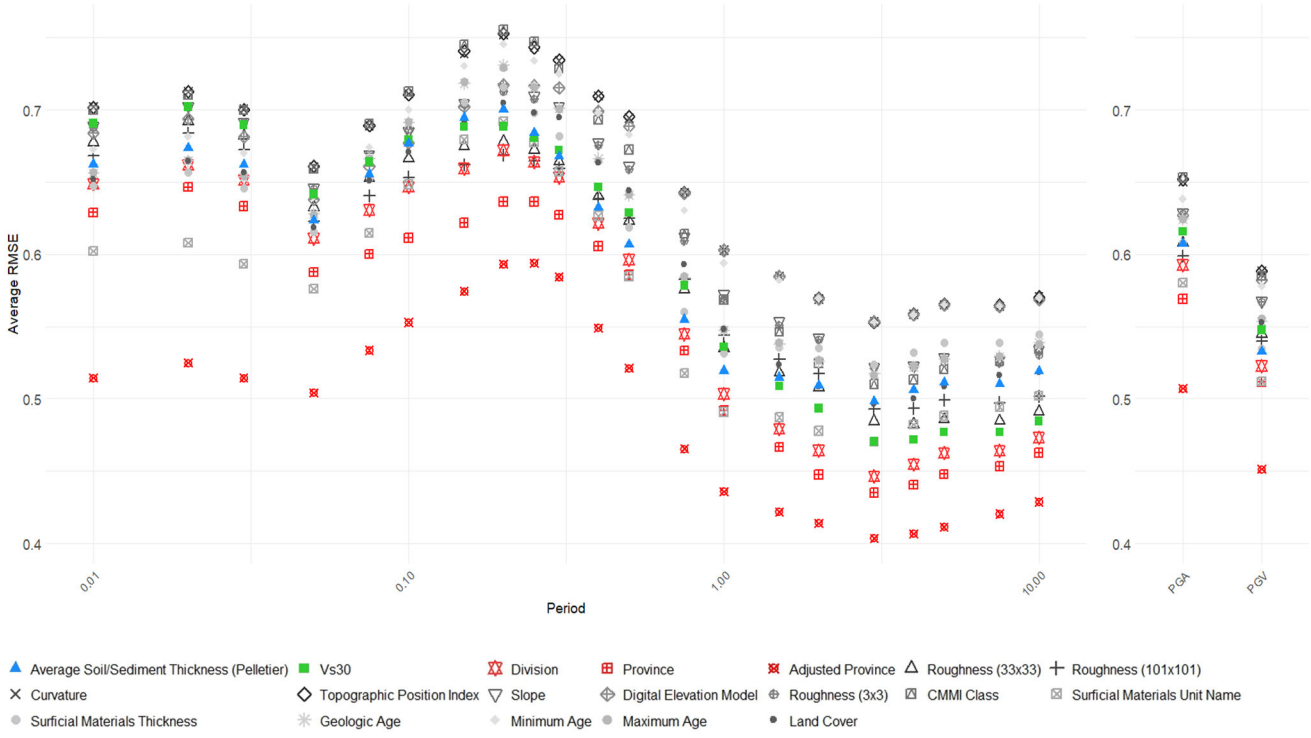


**Figure 2.11.** Average RMSE of the left-out group for each period by predictor for the Northern CEUS. Symbols indicate predictors, and colors indicate relevant predictor group with red being physiographic province, green being $V_{S30,}$ and blue representing sediment thickness by Pelletier et al. (2016). Other predictors are grey and distinguishable by symbol.

**Table 2.4**. Average RMSE of the left-out group across all periods by predictor for the Northern CEUS.

| **Predictors** | **Average RMSE** |
|---|---|
| Adjusted Province | 0.493 |
| Province | 0.551 |
| Surficial Materials Unit Name | 0.568 |
| Division | 0.571 |
| Roughness (101x101) | 0.594 |
| Roughness (33x33) | 0.595 |
| Average Sediment Thickness (Pelletier et al., 2016) | 0.597 |
| $V_{S30}$ | 0.597 |
| Land Cover | 0.604 |
| Surficial Materials Thickness | 0.606 |
| Geologic Age | 0.615 |
| Maximum Age | 0.615 |
| Roughness (3x3) | 0.623 |
| Slope | 0.625 |
| CMMI Class | 0.635 |
| Digital Elevation Model | 0.639 |
| Minimum Age | 0.642 |
| Curvature | 0.652 |
| Topographic Position Index | 0.652 |

***Two-Parameter Models:***

We then tested all two parameter models using the best single predictor as the first parameter. The best predictor is the Adjusted Physiographic Province for each region, but the other categorical variables are highly correlated with the Adjusted Physiographic Province (and share the same boundaries). Therefore, we only use continuous numerical variables for the second parameter to smooth the divisions between the adjusted provinces and avoid sharp boundaries between categorical-only predictors. The average RMSE of the left-out group of the two-parameter models is shown in Figures 2.12 to 2.14 across spectral periods, with the legend displaying the second continuous predictor that was used as a secondary predictor (in addition to Adjusted Physiographic Province). Figures 2.12, 2.13, and 2.14 show the results for the entire CEUS, Coastal Plain, and Northern CEUS Region, respectively. Tables 2.6, 2.7, and 2.8 show the respective average RMSE values as a function of spectral period.

For each region, the best performing model used Adjusted Physiographic Province as the initial parameter. The addition of a second geospatially continuous parameter further decreased the average RMSE in each region with varying levels. For the Coastal Plain region, the sediment thickness dataset provided an additional 12.7% decrease in average RMSE. For the Northern CEUS, the depth to bedrock provided an additional 1% decrease in average RMSE.

**Whole CEUS:**

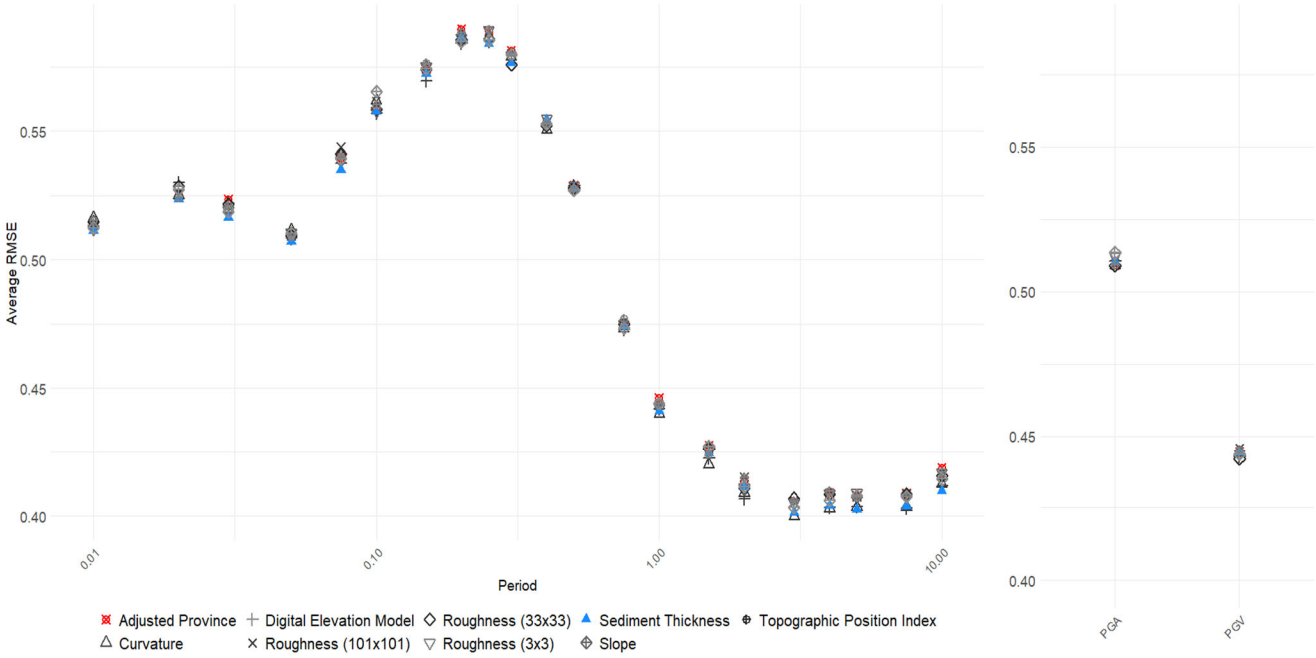


**Figure 2.12.** Average RMSE of the left-out group for each period by each secondary predictor, in addition to adjusted province, for the whole CEUS.

**Table 2.6.** Average RMSE of the left-out group across all periods by secondary predictor for the whole CEUS.

| **Predictors** | **Average RMSE** |
|---|---|
| Adjusted Province + Average Sediment Thickness (Pelletier et al., 2016) | 0.490 |
| Adjusted Province + Roughness (101x101) | 0.491 |
| Adjusted Province + Roughness (33x33) | 0.491 |
| Adjusted Province + TPI | 0.493 |
| Adjusted Province + DEM | 0.493 |
| Adjusted Province + Slope | 0.493 |
| Adjusted Province + Curvature | 0.493 |
| Adjusted Province + Roughness (3x3) | 0.493 |
| Adjusted Province | 0.494 |

## Coastal Plain:

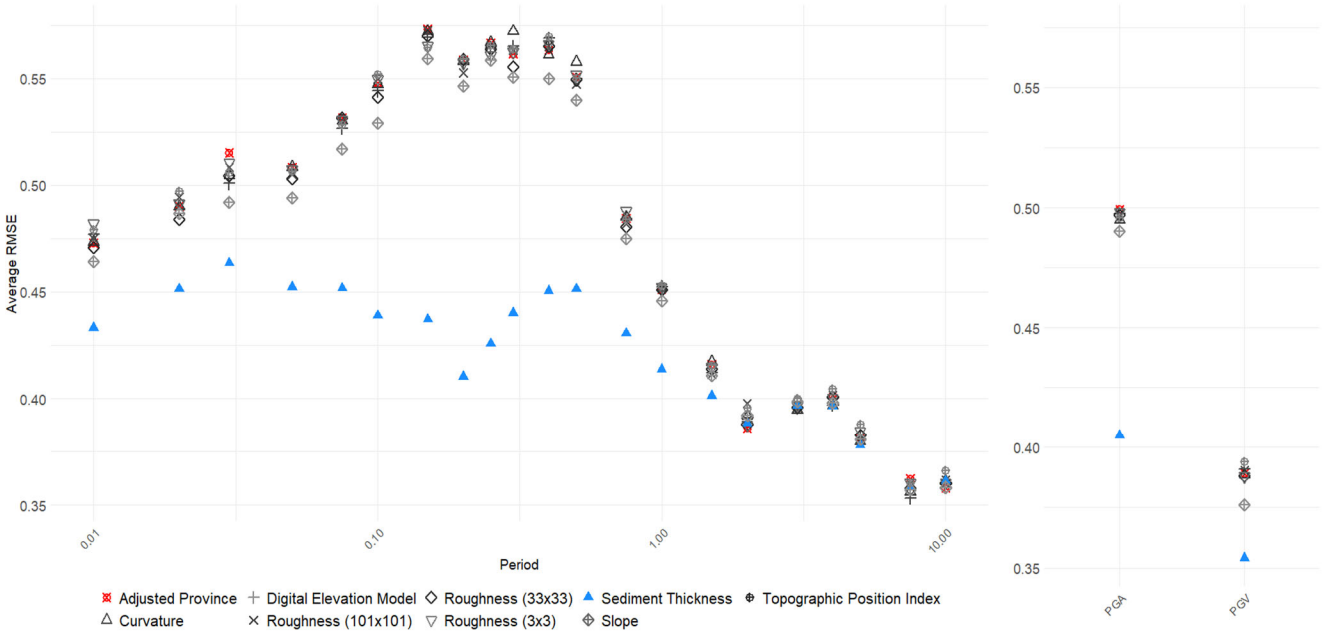


**Figure 2.13.** Average RMSE of the left-out group for each period by each secondary predictor, in addition to adjusted province, for the Coastal Plain.

**Table 2.7.** Average RMSE of the left-out group across all periods by secondary predictor for the Coastal Plain.

| **Predictors** | **Average RMSE** |
|---|---|
| Adjusted Province + Sediment Thickness in Coastal Plain (Boyd et al., 2024) | 0.417 |
| Adjusted Province + DEM | 0.468 |
| Adjusted Province + TPI | 0.474 |
| Adjusted Province + Roughness (101x101) | 0.476 |
| Adjusted Province + Curvature | 0.476 |
| Adjusted Province + Roughness (33x33) | 0.477 |
| Adjusted Province | 0.477 |
| Adjusted Province + Slope | 0.477 |
| Adjusted Province + Roughness (3x3) | 0.478 |

## Northern CEUS:

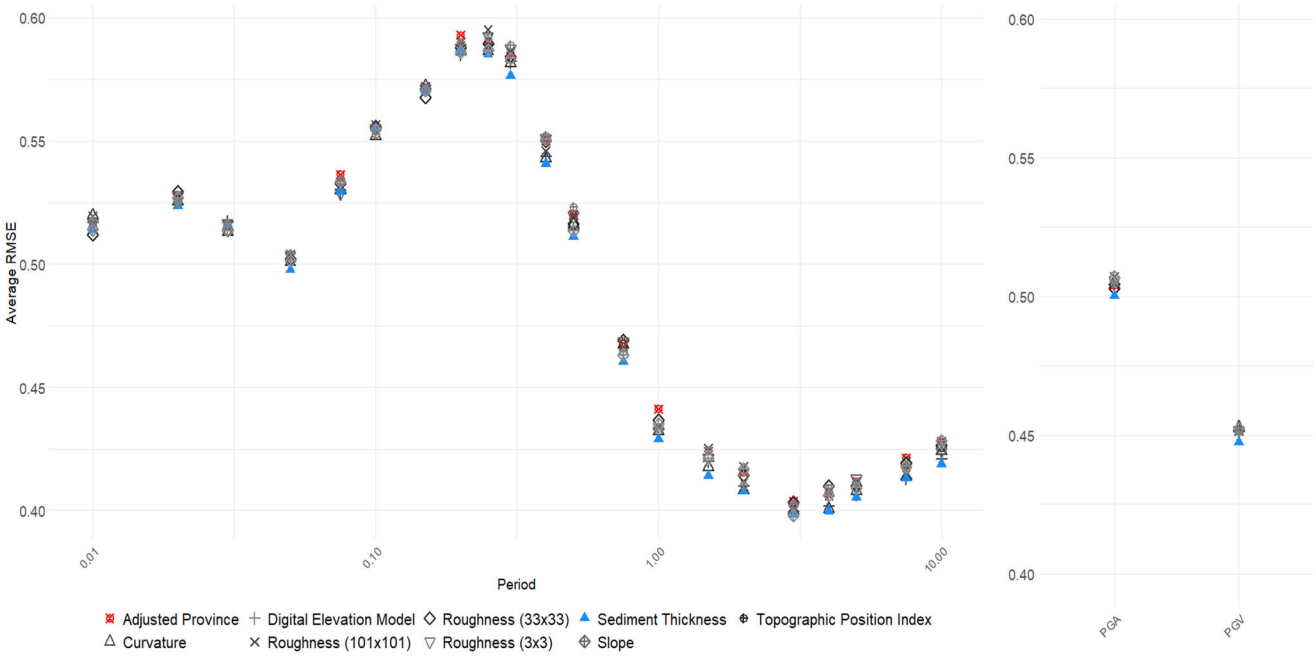


**Figure 2.14**. Average RMSE of the left-out group for each period by each secondary predictor, in addition to adjusted province, for the Northern CEUS.

**Table 2.8**. Average RMSE of the left-out group across all periods by secondary predictor for the Northern CEUS.

| **Predictors** | **Average RMSE** |
|---|---|
| Adjusted Province + Average Sediment Thickness (Pelletier et al., 2016) | 0.487 |
| Adjusted Province + Roughness (101x101) | 0.489 |
| Adjusted Province + Roughness (33x33) | 0.489 |
| Adjusted Province + DEM | 0.491 |
| Adjusted Province + TPI | 0.491 |
| Adjusted Province + Slope | 0.492 |
| Adjusted Province + Roughness (3x3) | 0.492 |
| Adjusted Province + Curvature | 0.492 |
| Adjusted Province | 0.493 |

## 2.3 Results

### 2.3.1 Model

For each of the two regions (Coastal Plain and northern CEUS), we fit the two-parameter model that produced the greatest reduction in RMSE in Section 2.2.5. We fit the models using multiple linear regression with adjusted physiographic provinces and sediment thickness as predictors, and the linear amplification terms as response variables. We extract the coefficients from these fitted models and create a new linear amplification term with the following functional form:

$$F_{Linear,j} = F_{ADJPROVINCE,j} + c_1 SedimentThickness_j \,, \tag{2.5}$$

where $F_{ADJPROVINCE,j}$ is the coefficient from the adjusted province of the station, $c_1$ is the sediment thickness coefficient based on region, and $SedimentThickness_j$ is the sediment thickness at the station. Appendix C provides tables of the coefficients $F_{ADJPROVINCE,j}$ and $c_1$ for regions throughout the CEUS.

We recommend a regionalized site amplification model for the CEUS that uses the different sediment thickness datasets and adjusted physiographic provinces. The adjusted physiographic provinces account for the large-scale regional patterns seen in the amplification terms. We observe these large patterns due to the geologic and tectonic history of the CEUS, which results in less topographic and geologic differences on a spatial scale than the WUS, where we might see large differences in slope, geology, and soil stiffness at a smaller scale. The adjusted provinces provide a proxy for differing geology and topography on a broad scale and likely relate to differences in velocity structure. Within these provinces, we also observe variation due to smaller structures, localized geology, and small-scale differences in soil stiffness. We recommend using local sediment thickness data to account for these within-province differences.

### 2.3.2 Reduction in S2S Variability

To assess our proposed model, we examine the difference in site variability between our proposed model and the current NGA-East linear site amplification model based on $V_{S30}$ (Stewart et al., 2020). To perform this comparison, we replace the linear term from the current NGA East GMM with our proposed linear term at each station. We then follow Equation 2.1 to obtain ground-motion residuals for each recording and Equation 2.2 to perform mixed effects regression, yielding site-to-site terms with the new linear amplification term at each station. We compare these site-to-site terms with the original S2S terms using the NGA-East linear site amplification based on $V_{S30}$ by computing the standard deviation of S2S values at each period, including PGA and PGV.

We provide two different comparisons, one using the NGA-East dataset (Goulet et al., 2021b), and another using a combined dataset that adds ground motions from CESMD (Thompson et al., 2023). First, we compare the S2S values using only the data from the NGA East dataset (Goulet et al., 2021b), by computing the standard deviation of S2S at 655 stations in the CEUS using our proposed model and the current NGA-East model. The current NGA-East model scaled on $V_{S30}$

was derived using the NGA-East database. The standard deviation of the site-to-site term for these 655 stations is shown in Figure 2.15. The standard deviation of S2S terms using our linear amplification model based on physiographic province and sediment thickness is lower than the standard deviation using the $V_{S30}$-based NGA-East linear amplification model across all periods less than 3 s. For periods longer than 3 s, the $V_{S30}$-based NGA-East linear amplification model offers slightly lower standard deviations than our model. For SA for periods of 0.01 seconds to 3 seconds, as well as PGA and PGV, there is significant reduction in the standard deviation of S2S using our proposed model, with an average reduction of 33.9% across all periods.

We also compare the standard deviations using a combined dataset of ground motions from NGA-East and the CESMD (Figure 2.1). This comparison is performed to evaluate the models against more data, including more recent earthquakes. These S2S values use more data at each station to quantify site effects and have more spatial coverage. However, the original $V_{S30}$-based NGA-East model has not seen the data from CESMD in model development. We examine the standard deviation of S2S at 2,078 stations to assess the variability for each model in Figure 2.16. The standard deviation using our physiographic province and sediment thickness-based amplification model is lower across all periods, including PGA and PGV, with an average reduction of 25.3%.

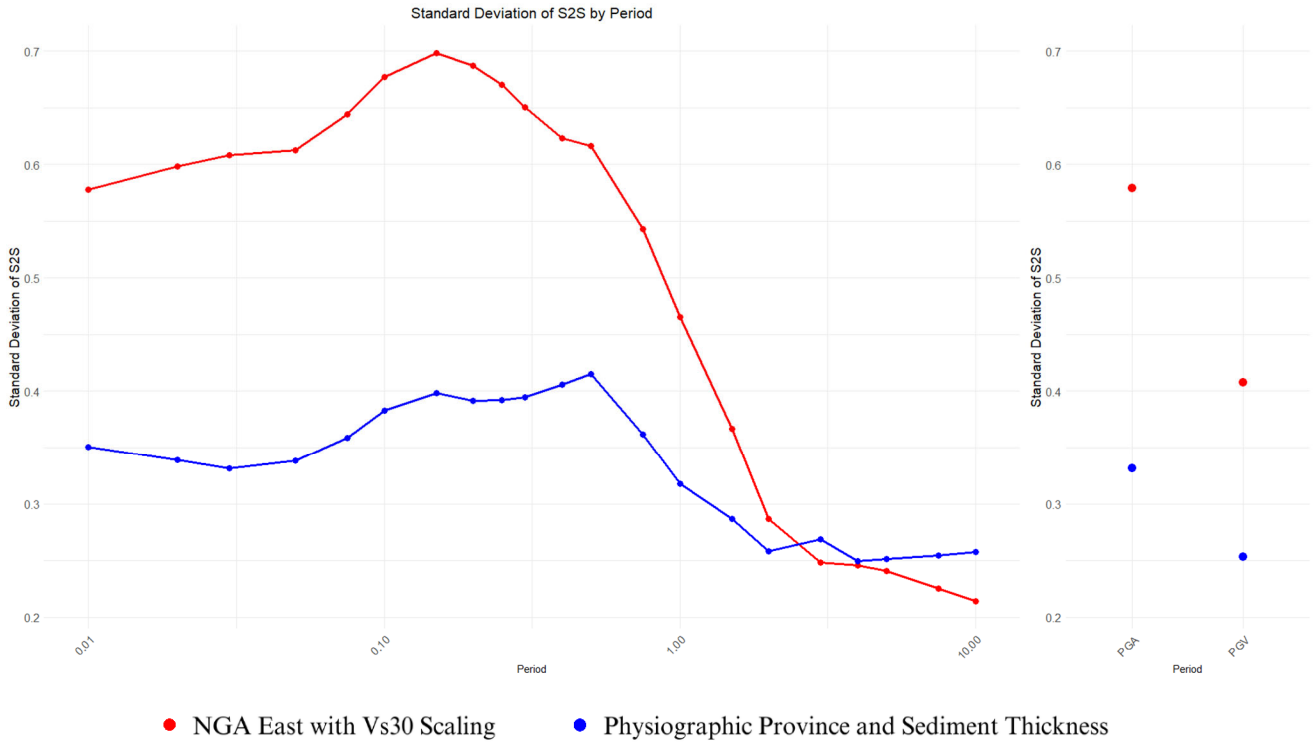


**Figure 2.15.** Standard deviation of site-to-site terms using ground-motion data from NGA East, using the current NGA-East linear amplification term (red) and the new proposed amplification term as part of this study (blue).

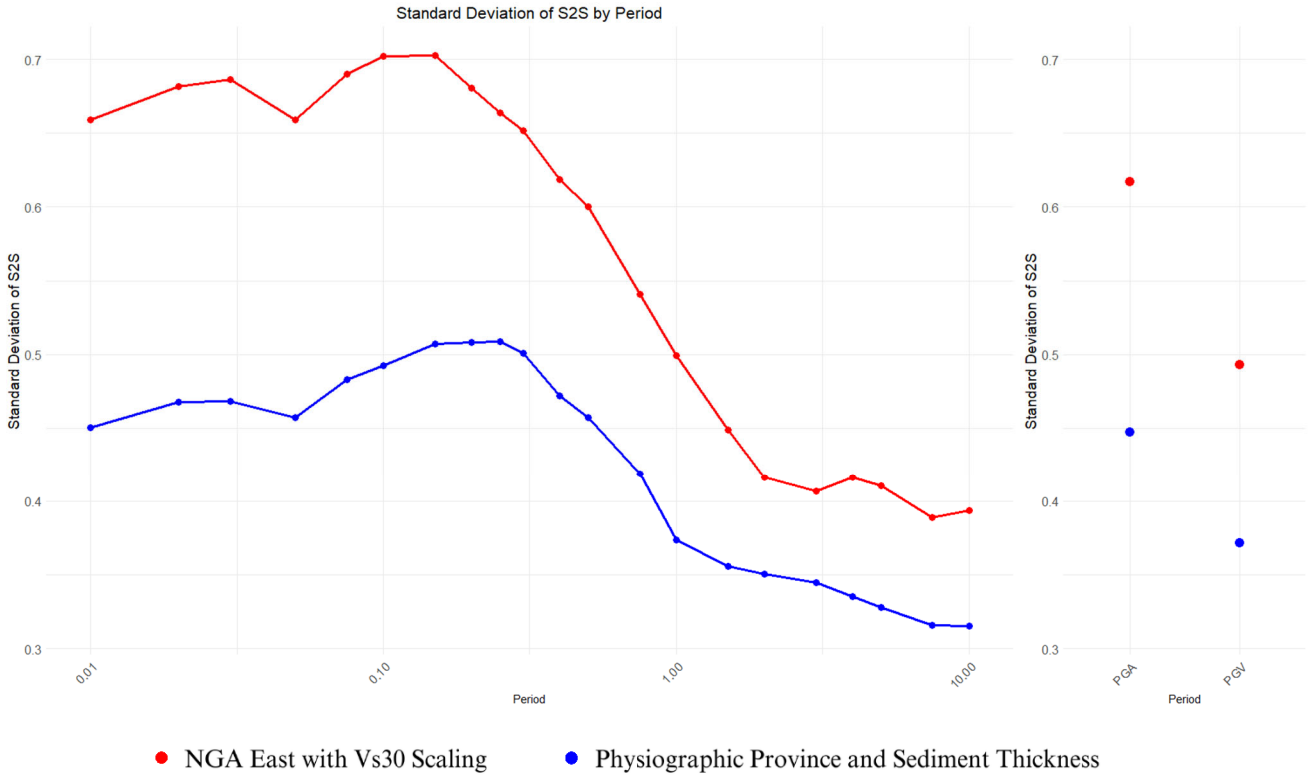


**Figure 2.16.** Standard deviation of site-to-site terms from the entire ground-motion dataset (using records from both NGA-East and CESMD) for magnitudes 4 and greater, using the current NGA-East linear amplification term (red) and the new proposed amplification term as part of this study (blue).

# Chapter 3: Geotechnical Site Response Analyses in Selected CEUS Cities: Memphis and New York City

Chapter 3 will describe the results of linear one-dimensional (1D) site response analyses in two selected Central and Eastern United States (CEUS) cities: Memphis, Tennessee, and New York City, New York. These efforts were led by Professor James Kaklamanos and three of his undergraduate research assistants at Merrimack College: Irvin Guzman, George Sachs-Walor, and Arden Dioslaki. The goal is to characterize the effects of sediment thickness on site response in two major American cities in well-characterized sedimentary basins of varying thicknesses, and to compare linear amplifications from our ergodic site amplification model (described in Chapter 2) with amplification spectra from theoretical one-dimensional linear site response analyses. Memphis, Tennessee, was selected due to its high seismic hazard close to the New Madrid Seismic Zone, its deep sediment thickness in the middle of the Mississippi Embayment, and the abundance of shear-wave velocity measurements (more so than any other city in the CEUS). New York City, New York, was selected to sample a location on the edge of the Atlantic Coastal Plain with shallower sediments, its location in a region of moderate seismicity, and the availability of ground-motion recordings from the recent 2024 **M** 4.8 Tewksbury, New Jersey, earthquake. For each of the cities, we will describe the shear-wave velocity datasets, site response methodology, and results of the analyses. The framework established herein can be used to study other cities in the Central and Eastern U.S., such as those in Appendix A.

## 3.1 Site Characterization Data and Models

In this section, we will describe the available site characterization data that were used to develop shear-wave velocity models for our study locations in Memphis, Tennessee, and New York City, New York. The available depth-to-bedrock models in each region are also discussed.

### 3.1.1 Memphis, Tennessee

Memphis, Tennessee, is located in the Mississippi Embayment within the Gulf Coastal Plain. Due to its high seismic hazard and close distance to the New Madrid Seismic Zone, Memphis is arguably the most well-characterized CEUS city in terms of seismic hazards. The depth to bedrock in Memphis is approximately 1 km, with the bedrock surface sloping downwards approaching the Mississippi River. Figure 3.1 shows the estimated depths of Paleozoic limestones and Cretaceous sediments from the model of Cramer et al. (2004). The increasing bedrock depths approaching the Mississippi River are clearly observed.

In this study, we employ the recent Boyd et al. (2024) sediment thickness model for the Atlantic and Gulf Coastal Plains to characterize the depth to bedrock in Memphis, Tennessee. Boyd et al. (2024) define the depth to bedrock as the base of the Cretaceous sediments underlying the Atlantic Coastal Plain and Mesozoic sediments underlying the Gulf Coastal Plain. Across the ground-motion stations encountered in the vicinity of Memphis, Tennessee, the sediment thicknesses range from approximately 800 to 1300 m, with an average of 1100 to 1200 m. In the site response calculations to be described later in this chapter, shear-wave velocity profiles are developed throughout the entire sediment column, and they are truncated at the depth of bedrock.

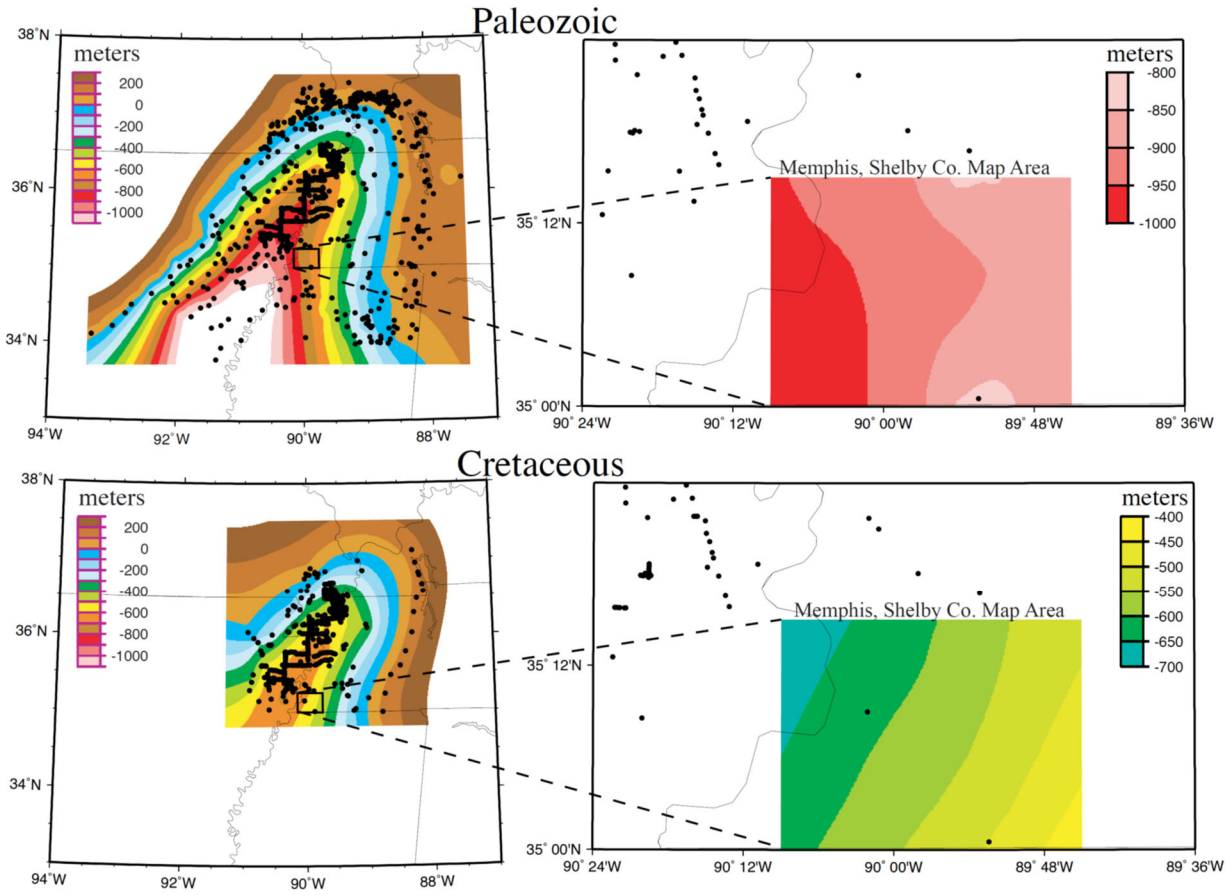


**Figure 3.1.** Estimated depths to the top of the Paleozoic limestones (top figures) and Cretaceous sediments (bottom figures) in the vicinity of Memphis, Tennessee. Black dots indicate locations where well log observations constrain these boundaries. Memphis is at a surface elevation of approximately 100 m. Source: Cramer et al. (2004).

This study leverages the extensive shear-wave velocity ($V_S$) data available throughout the Memphis area. Gann-Phillips et al. (2024) developed a regional seismic velocity model for the U.S. Atlantic and Gulf Coastal Plains based on measured shear wave velocity, sediment thickness, and surface geology. Depth-based $V_S$ models were developed using measured data across multiple surficial geologic units: Quaternary Holocene (QH), Quaternary Pleistocene (QP), Tertiary (T), and Cretaceous (K). The $V_S$ data in the Memphis region considered by Gann-Phillips et al. (2024) are shown in Figure 3.2, along with the different surficial geologic units in the vicinity. Gann-Phillips et al. (2024) opted to include an additional Memphis (MEM)-specific $V_S$ model separate from the broader Tertiary (T) $V_S$ model because the geographically clustered $V_S$ data in Memphis displayed differing characteristics. Plots of the Gann-Phillips et al. (2024) velocity models for QH, T, and MEM (the three units relevant to the greater Memphis area) in the upper 1300 m (roughly the maximum sediment thickness in greater Memphis) are provided in Figure 3.3. The QH and MEM velocity models are very similar, but the T velocity model is noticeably stiffer beneath depths of approximately 170 m.

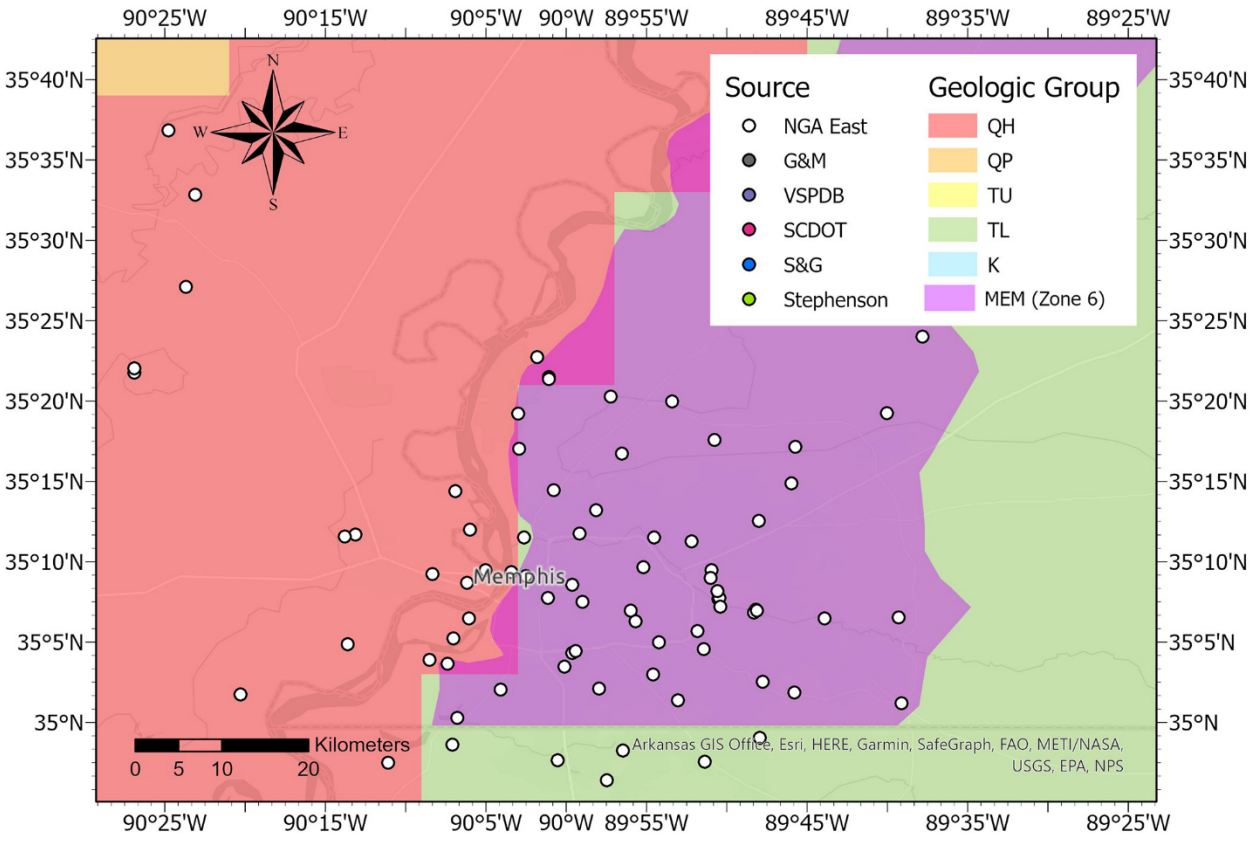


**Figure 3.2.** Gann-Phillips et al. (2024) Memphis $V_S$ data cluster, along with the boundaries of the different geologic units. The $V_S$ profile data in Memphis are largely from the Next Generation Attenuation (NGA) East $V_S$ database (used in the work by Parker et al., 2017). Source: Gann-Phillips et al. (2024).

In addition to extensive site characterization data, the Memphis region also has a large number of ground-motion recording stations owing to its high seismic hazard. As explained in Chapter 2, a set of seismic stations was developed for this project using two different CEUS ground motion datasets: the publicly available NGA-East dataset from the Pacific Earthquake Engineering Research Center (Goulet et al., 2021) and the Center for Engineering Strong Motion Data (CESMD) database for CEUS ground motions from 2010 to 2020 (Thompson et al., 2023). Figures 3.4 and 3.5 provide an overview of the distribution of ground-motion stations relative to the velocity profile locations in Memphis, with labels for the ground-motion stations in Figure 3.4 and velocity profiles in Figure 3.5. There are a total of 21 ground-motion recording stations and 99 velocity profiles compiled for the Memphis area.

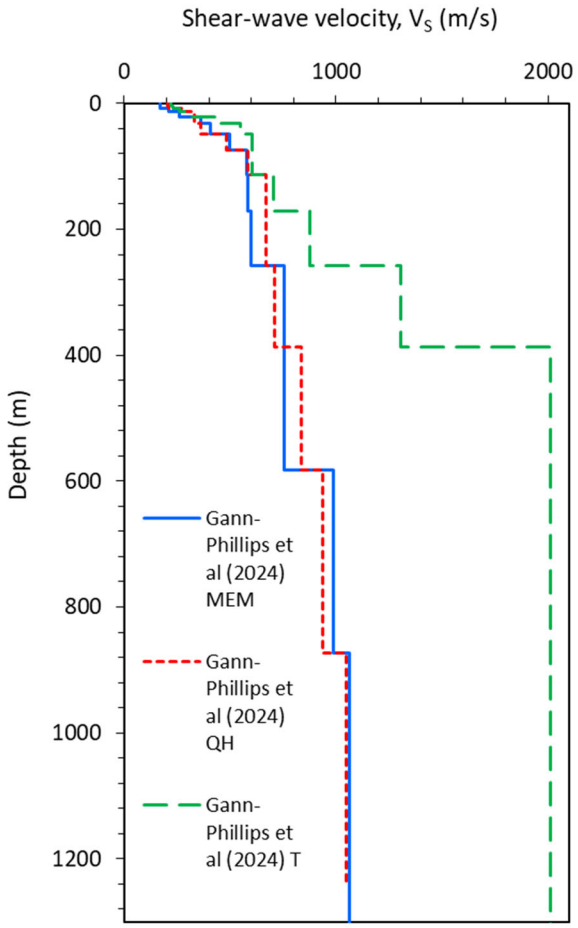


**Figure 3.3.** Gann-Phillips et al. (2024) Coastal Plain velocity models for Quaternary Holocene (QH), Memphis subgroup (MEM), and Tertiary (T), the three surficial geologic units present in the vicinity of Memphis. The plot is provided to a depth of 1300 m, approximately the maximum sediment thickness in the greater Memphis area.

At each of the 21 ground-motion stations, we selected the nearest measured velocity profiles (within a range of 10 km) for the development of station-specific average velocity models for site response analyses. Figure 3.6 illustrates circles with 10-km radii around each of the 21 ground-motion stations that aided in the selection of relevant velocity profiles for each station. Tables 3.1 and 3.2 provide a list of the stations, sediment depths from Boyd et al. (2024), and characteristics of the average velocity model at each station. For stations with no nearby velocity profiles, the Gann-Phillips et al. (2024) Coastal Plain velocity model was used to characterize the subsurface velocity. Depending on which surficial geologic unit is associated with the seismic recording station, either the QH, T, or MEM velocity model was used (Figure 3.3). The average velocity profiles were used to characterize the near-surface velocity structure at each station; the construction of the velocity models at depth will be described later in this section. The average shear-wave velocities in the upper 30 m ($V_{S30}$) for all sites fall into the National Earthquake Hazards Reduction Program (NEHRP) Site Class D (stiff soil) category ($180 \leq V_{S30} \leq 360$ m/s), with the exception of Station NM.COLT, which falls into Site Class C (very dense soil and soft rock) but is close to the CD boundary (BSSC, 2020).

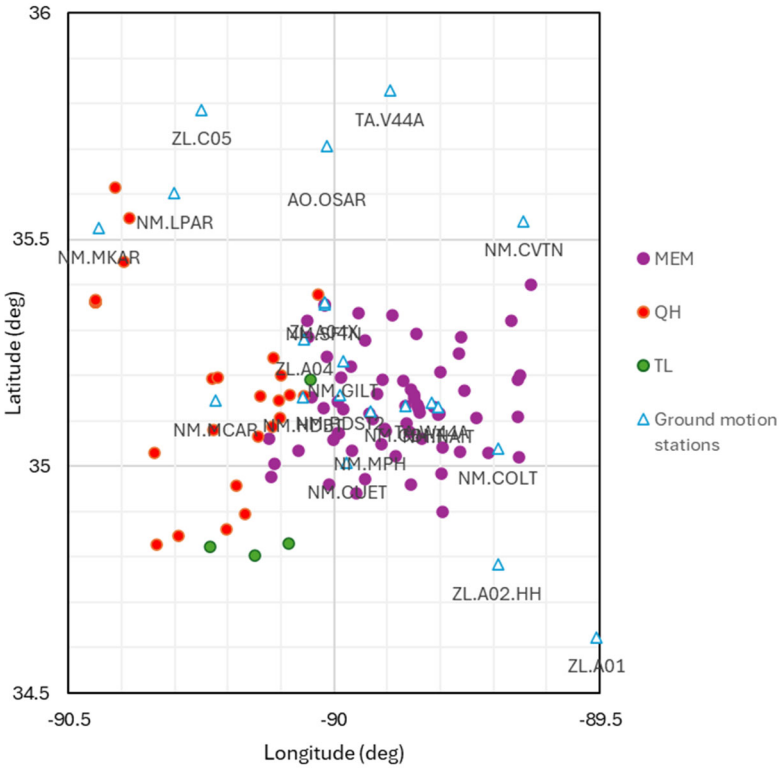


**Figure 3.4.** Distribution of ground-motion stations in the Memphis area relative to the available velocity profiles, separated by surficial geologic unit. Station identification numbers are listed.

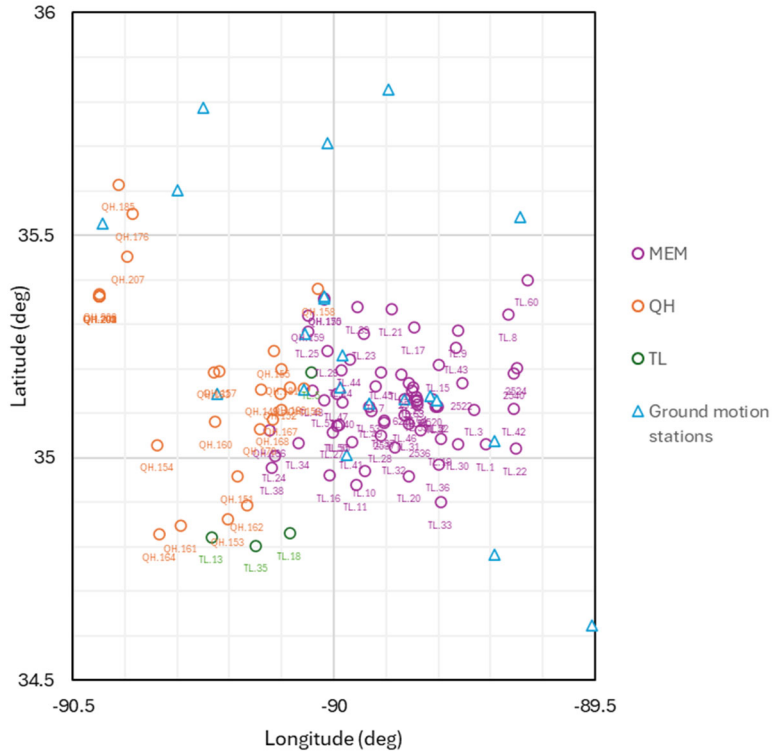


**Figure 3.5.** Distribution of velocity profiles in the Memphis area, sorted by geologic unit, relative to the ground motion stations. Identification numbers of velocity profiles are listed.

**Table 3.1.** Characteristics of ground-motion recording stations and associated site characterization data in Memphis, sorted from west to east.

| Station Code | Station Name / Location | Latitude (deg) | Longitude (deg) | Geologic unit | Surface elevation (m) | Sediment thickness (m) | Average shear-wave velocity, $V_{S30}$ (m/s) |
|---|---|---|---|---|---|---|---|
| NM.MKAR | Mark Tree, AR (CERI) | 35.5257 | -90.4418 | QH | 64 | 1061 | 212 |
| NM.LPAR | Lepanto, AR | 35.6019 | -90.3002 | QH | 65 | 1092 | 219 |
| ZL.C05 | Manila, AR, USA | 35.7870 | -90.2497 | QH | 68 | 1023 | 237 |
| NM.MCAR | Mid-South CC, West Memphis, AR (CERI) | 35.1450 | -90.2230 | QH | 66 | 1260 | 189 |
| NM.HDBT | Hernando de Soto Bridge; Memphis, TN | 35.1533 | -90.0582 | QH | 57 | 1218 | 257 |
| ZL.A04 | Memphis, TN | 35.2793 | -90.0560 | QH | 92 | 1267 | 260 |
| NM.SFTN | Shelby Forest, TN | 35.3575 | -90.0187 | MEM | 127 | 1284 | 260 |
| ZL.A04X | Memphis, TN, USA | 35.3624 | -90.0178 | MEM | 135 | 1279 | 260 |
| AO.OSAR | Osceola, AR | 35.7064 | -90.0126 | QH | 73 | 1128 | 237 |
| NM.RDST2 | Rhodes College, Memphis, TN | 35.1578 | -89.9886 | MEM | 80 | 1195 | 320 |
| NM.GILT | SWCC Gill Campus, Memphis, TN | 35.2310 | -89.9830 | MEM | 85 | 1218 | 245 |
| NM.CUET | CUSEC HQ, Memphis, TN | 35.0070 | -89.9760 | MEM | 100 | 1185 | 285 |
| NM.MPH | Univ of Memphis, Memphis, TN | 35.1220 | -89.9320 | MEM | 96 | 1174 | 309 |
| TA.V44A | Blytheville, AR | 35.8282 | -89.8954 | QH | 73 | 1099 | 237 |
| NM.CBHT | Christian Brothers High School, Memphis, TN | 35.1326 | -89.8657 | MEM | 83 | 1114 | 249 |
| TA.W44A | Shelby Farms Park, Memphis, TN | 35.1395 | -89.8161 | MEM | 91 | 1090 | 235 |
| NM.NAIT | Shelby Farm, Memphis, TN | 35.1300 | -89.8040 | MEM | 86 | 1080 | 235 |
| NM.COLT | UM Carrier Ctr, Collierville, TN | 35.0385 | -89.6922 | MEM | 110 | 976 | 388 |
| ZL.A02.HH | Byhalia, MS | 34.7837 | -89.6919 | TL | 126 | 941 | 299 |
| NM.CVTN | Crestview Middle School, Covington, TN | 35.5415 | -89.6435 | MEM | 99 | 1064 | 251 |
| ZL.A01 | Waterford, MS | 34.6231 | -89.5059 | TL | 126 | 782 | 299 |

**Table 3.2.** Characteristics of selected velocity profiles used in the development of average shear-wave velocity models at Memphis ground-motion recording stations.

| Station Code | Number of profiles used in average $V_S$ model | Depth of average $V_S$ model (m) | Nearby velocity profiles used in the station-specific average $V_S$ model (Figure 3.5) |
|---|---|---|---|
| NM.MKAR | 3 | 175 | QH.176, QH.185, QH.207 |
| NM.LPAR | 2 | 175 | QH.176, QH.185 |
| ZL.C05 | 0 | 0 | None; use Gann-Phillips et al. (2024) QH model |
| NM.MCAR | 3 | 70 | QH.157, QH.160, QH.163 |
| NM.HDBT | 2 | 80 | QH.156, TL.48 |
| ZL.A04 | 2 | 50 | QH.159, TL.25 |
| NM.SFTN | 3 | 58 | QH.158, QH.175, QH.150 |
| ZL.A04X | 3 | 58 | QH.158, QH.175, QH.150 |
| AO.OSAR | 0 | 0 | None; use Gann-Phillips et al. (2024) QH model |
| NM.RDST2 | 3 | 76 | TL.40, TL.47, TL.51 |
| NM.GILT | 3 | 70 | TL.14, TL.44, TL.29 |
| NM.CUET | 6 | 67 | TL.10, TL.16, TL.41, TL.27, TL.28, TL.32 |
| NM.MPH | 6 | 100 | TL.7, TL.49, 2537, TL.53, TL.37, TL.40 |
| TA.V44A | 0 | 0 | None; use Gann-Phillips et al. (2024) QH model |
| NM.CBHT | 7 | 160 | TL.6, TL.26, TL.54, TL.59, TL.63, TL.64, 6275 |
| TA.W44A | 8 | 160 | TL.2, TL.4, TL.52, 2520, TL.64, TL.54, TL.6, TL.59 |
| NM.NAIT | 8 | 160 | TL.2, TL.4, TL.52, 2520, TL.64, TL.54, TL.6, TL.59 |
| NM.COLT | 2 | 20 | TL.1, TL.22 |
| ZL.A02.HH | 0 | 0 | None; use Gann-Phillips et al. (2024) T model |
| NM.CVTN | 1 | 58 | TL.60 |
| ZL.A01 | 0 | 0 | None; use Gann-Phillips et al. (2024) T model |

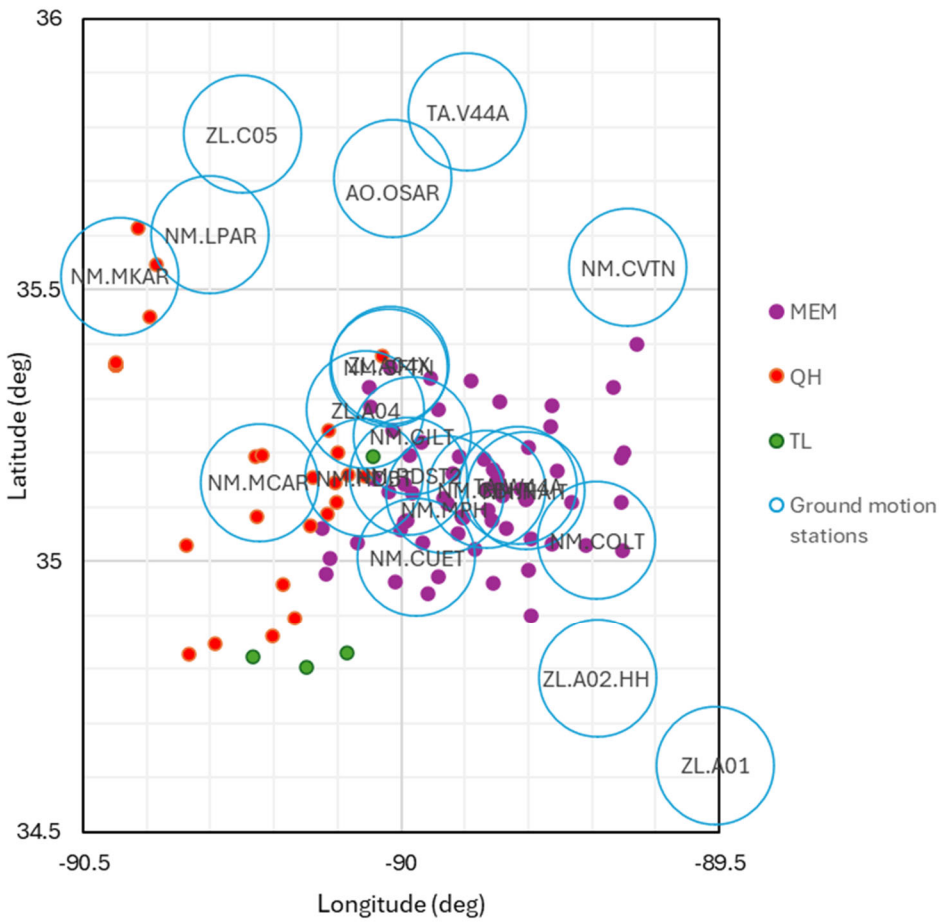


**Figure 3.6.** Distribution of ground-motion stations in the Memphis area relative to the available velocity profiles, with 10-km-radius circles drawn around each station. This map was used to select relevant profiles for each of the stations for site response analyses.

From all the relevant velocity profiles at each station, an average Vs profile was computed using the geometric mean of the available velocity data at each depth. The average profile at each station was plotted with the measured Vs profiles for each station, and the average profile was smoothed as needed to avoid artificial impedance contrasts and velocity inversions. Across the 21 stations, a total of 44 measured velocity profiles were incorporated into the model; Figure 3.7 provides a plot of all the measured Vs profiles that entered the computation of the average Vs models in Memphis. Of the 21 stations, there were five (5) stations that used the Gann-Phillips et al. (2024) velocity model all the way to the surface due to the lack of nearby seismic velocity measurements. In addition, two sets of two stations were located in such close proximity to each other that the same average Vs model was used for each pair of stations. Therefore, a total of 14 sets of average near-surface Vs models were developed. Figure 3.8 provides an example of the average velocity profile, along with the associated measured velocity data, for a ground-motion recording station (Station NM.CUET: CUSEC HQ) in Memphis.

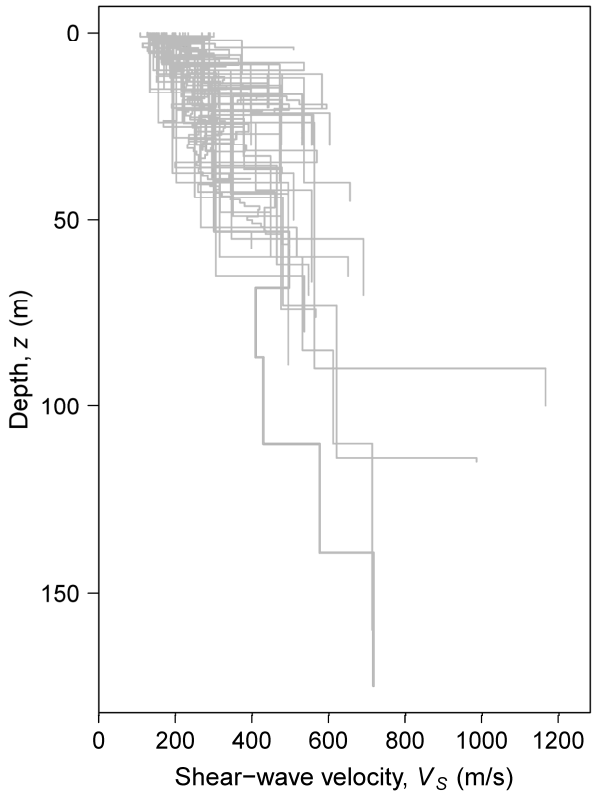


**Figure 3.7.** Plots of the 48 measured $V_S$ profiles that entered the near-surface average velocity profile models at the 21 ground-motion stations in Memphis.

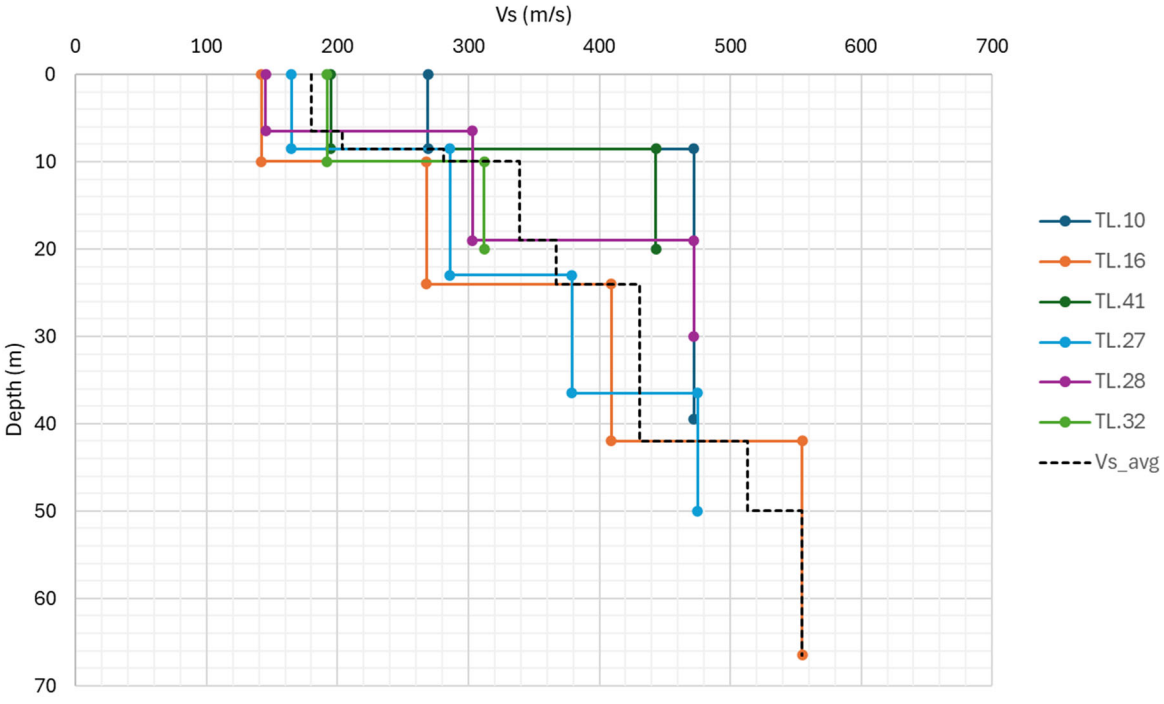


**Figure 3.8.** Example near-surface average $V_S$ model based on measured $V_S$ data for Station NM.CUET: CUSEC HQ (latitude: 35.0070°, longitude: -89.9760°) in Memphis.

Beneath the near-surface average $V_S$ model at each station, the deeper portion of the profile was constrained using the Gann-Phillips et al. (2024) Coastal Plain Vs model corresponding to the geologic unit in which the station is located (either QH, MEM, or T). The Gann-Phillips et al. (2024) model is applied for depths beneath the "Depth of average $V_S$ model (m)" column for each station in Table 3.2, up to the sediment thickness at each station as noted in Table 3.1. However, a transition zone was sometimes needed at some stations in cases where the values of the station-specific velocity model at the depth of transition exceed the values of the Gann-Phillips et al. (2024) velocity model. In these cases, a transition velocity was used to avoid artificial inversions associated with the stitching of the two velocity models. The ending value of the station-specific velocity model was extended downward until it met the velocity model of Gann-Phillips et al. (2024). Figure 3.9 provides an example of the full velocity model for Station NM.CUET (CUSEC HQ) in Memphis, which has a sediment thickness of 1185 m. The underlying bedrock velocity in Memphis is quantified as $V_{S,bedrock}$ = 3000 m/s, consistent with the CEUS reference rock condition of Hashash et al. (2014), as well as the Gann-Phillips et al. (2024) velocity model.

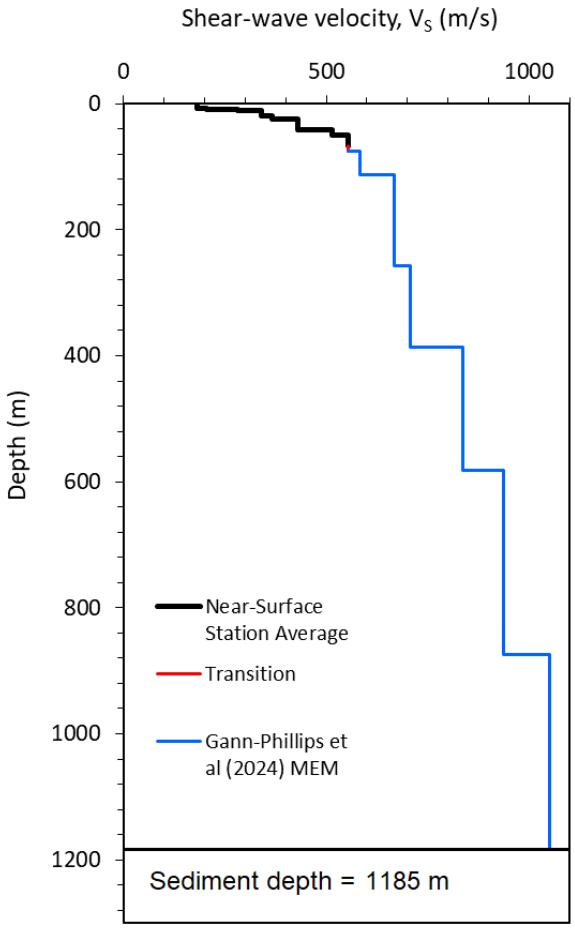


**Figure 3.9.** Example full $V_S$ model for site response for Station NM.CUET: CUSEC HQ (latitude: 35.0070°, longitude: -89.9760°) in Memphis. The upper 67 m is characterized using the near-surface average $V_S$ model in Figure 3.8, the deeper part of the profile (75 to 1185 m) is constrained using the Gann-Phillips et al. (2024) Memphis-specific (MEM) Coastal Plain velocity model, and a transition zone from 67 to 75 m extends the near-surface average velocity model to meet the underlying Gann-Phillips et al. (2024) velocity profile. Beneath the depth to bedrock (which varies from site to site), the profile is truncated and a bedrock velocity of $V_{S,bedrock}$ = 3000 m/s is assigned.

### 3.1.2 New York City, New York

New York City, New York, was selected as our second study area due to its significance as largest U.S. city by population, its location in a region of moderate seismicity, and the availability of ground-motion recordings from the recent 2024 **M** 4.8 Tewksbury, New Jersey, earthquake. New York City, which is located on the edge of the Atlantic Coastal Plain, has significantly shallower sediment thicknesses overall than Memphis, but there is greater variability in the thicknesses of sediments.

DeMott et al. (2023) developed a comprehensive depth-to-bedrock model for the five boroughs of New York City, using historical data and horizontal-to-vertical spectral ratio (HVSR) measurements. Figure 3.10 illustrates the depth-to-bedrock model of DeMott et al. (2023), which provides bedrock depths in feet. There is a clear increase in sediment thickness from northwest to southeast as the Atlantic Coastal Plain thickens. Bedrock is typically shallow (generally 0 to 15 m deep) throughout most of Manhattan, the Bronx, and Staten Island (with the exception of the southern part of Staten Island, where it is deeper). Bedrock depths increase significantly in Brooklyn and Queens, reaching a maximum of approximately 360 m in the extreme southeastern portion of New York City on the Rockaway Peninsula. Because there is such a large variation in subsurface conditions, New York City provides an interesting test case to evaluate the impact of sediment thickness on site response. We employed the depth-to-bedrock model of DeMott et al. (2023) for the New York City stations evaluated in this study.

Compared to Memphis, there are far fewer seismic velocity profiles available for New York City. We conducted a literature search to find publications with $V_S$ data for New York City, and used the results to develop a near-surface velocity model specific to New York City. In Memphis, the large spatial coverage of velocity measurements allowed us to select the profiles most relevant to each seismic station. In New York City, the spatial coverage of velocity measurements is sparser, and developing station-specific velocity profiles is not as feasible. Therefore, all the velocity measurements are pooled to develop a city-wide $V_S$ model that will be applied to all stations.

Shear-wave velocity data for New York City were extracted from a number of studies, and involved a combination of measured $V_S$ profiles and assumed $V_S$ profiles (computed, for example, from correlations with standard penetration test data). Eight profiles were collected from Nikolau et al. (2001), in which site factors for seismic bridge design in the New York metropolitan area were evaluated. An additional ten $V_S$ profiles from Nikolau and Edinger (2001) from Brooklyn, Queens, and Manhattan were compiled and cross-checked with the profiles of Nikolau et al. (2001) to remove any duplicates; four profiles were retained. Six $V_S$ profiles collected from surface-wave measurements by Stephenson et al. (2009) were also included in the dataset. Additional shear-wave velocity data were collected from Thomann and Chowdhury (2004) from bridge projects in Brooklyn, from Li and Wetzel (2019) for two project sites (one in Manhattan and one in Brooklyn), and from Riegel et al. (2019) for the Brooklyn Queens Expressway Connector. Plots of all the profiles are provided in Figure 3.11. The 21 $V_S$ profiles in the database span the upper 60 m of the subsurface and exhibit a clear increase with depth.

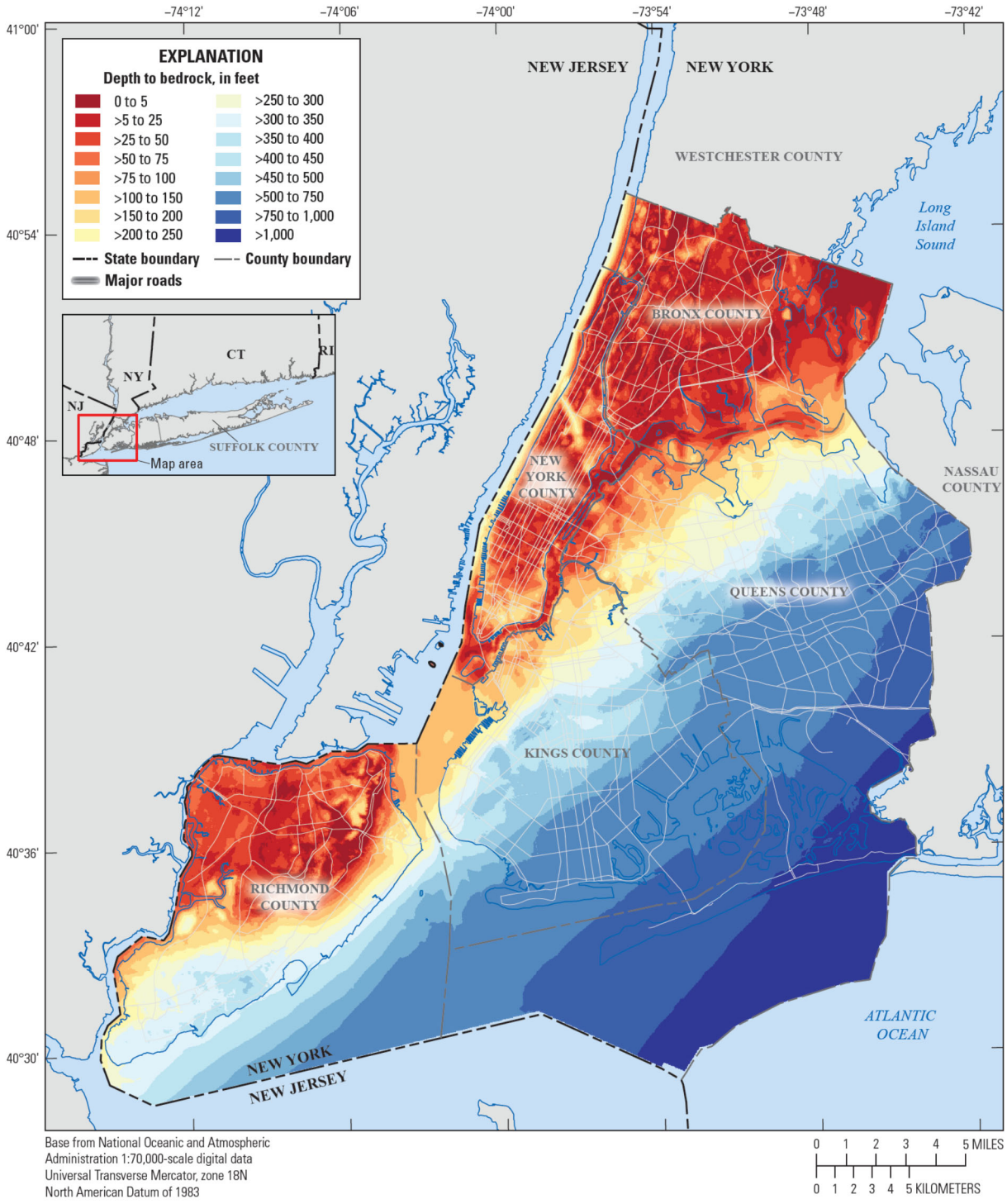


**Figure 3.10.** Depth-to-bedrock model of DeMott et al. (2023) for New York City. Depths are provided in feet. Source: DeMott et al. (2023).

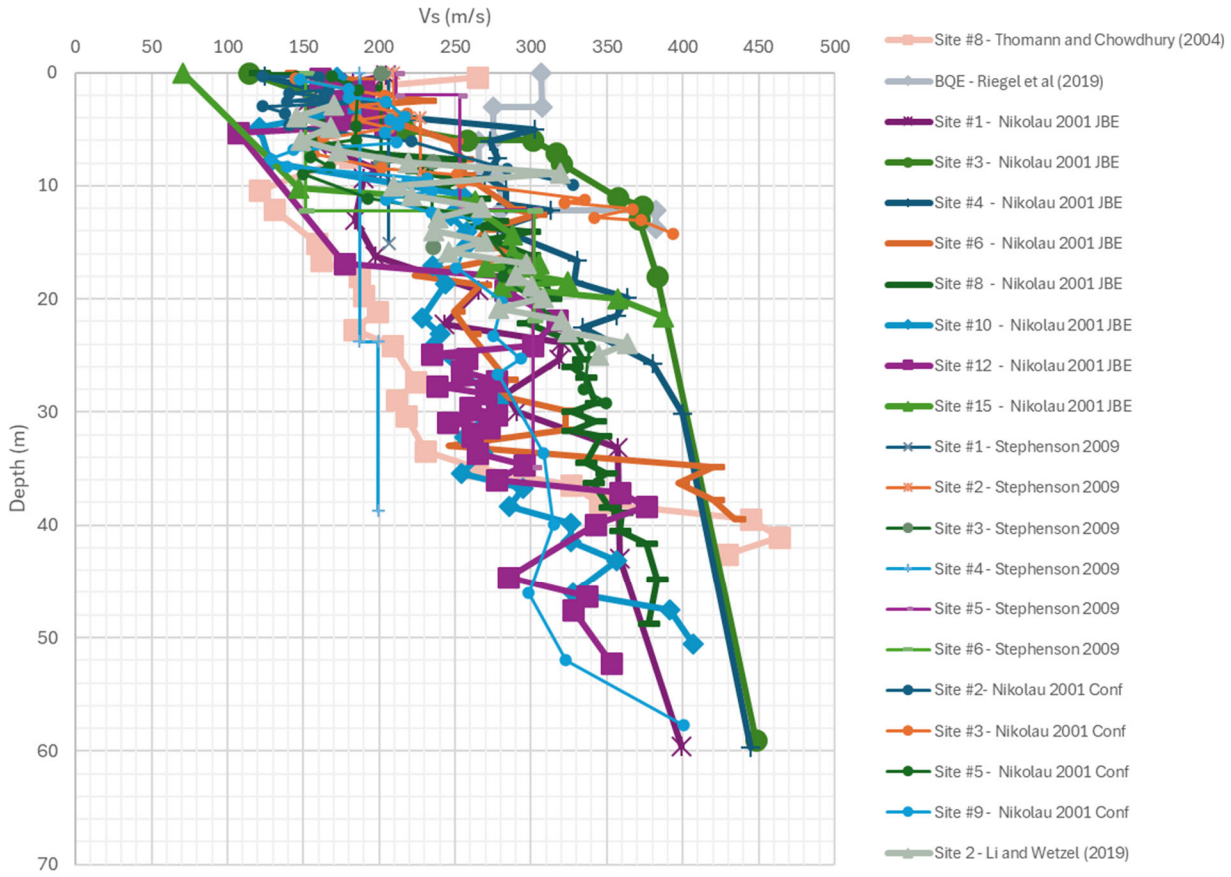


**Figure 3.11.** Compilation of near-surface velocity data (21 $V_S$ profiles) for New York City from Nikolau et al. (2001), Nikolau and Edinger (2001), Stephenson et al. (2009), Thomann and Chowdhury (2004), Li and Wetzel (2019), and Riegel et al. (2019). Bedrock velocity measurements in Stephenson et al. (2009) are excluded.

A power-law regression model for shear-wave velocity ($V_S$) as a function of depth ($z$) was developed using the velocity profile data in Figure 3.11. The functional form in Equation 3.1 was employed:

$$V_s = a(1+z)^b, \tag{3.1}$$

where $a$ and $b$ are the two model coefficients to be determined from the regression. The coefficient $a$ is interpreted as the surficial shear-wave velocity, and the coefficient $b$ quantifies the dependence with depth. Similar functional forms were employed by, for example, Ibs-von Seht and Wohlenberg (1999) and Delgado (2000). The usage of the term $1 + z$ instead of $z$ ensures that seismic velocity does not approach zero in the upper meter of the profile.

Equation 3.1 is easily fit using linear regression techniques, as the equation can be linearized by taking the natural logarithm of both sides:

$$\ln(V_S) = \ln(a) + b\ln(1+z)\,. \tag{3.2}$$

The velocity data in Figure 3.11 were sampled every 0.1 m to extract the data to fit the coefficients. We found that $a$ = 116 m/s and $b$ = 0.29, so the New York City-specific near-surface seismic velocity model becomes:

$$V_s = 116(1+z)^{0.29}\,, \tag{3.3}$$

applicable for depths in the range $0 \leq z \leq 60$ m. Figure 3.12 is a plot of the power-law model in Equation 3.3 overlain on the seismic velocity data from Figure 3.11, and Figure 3.13 presents a simplified plot with the data points associated with the velocity measurements.

Throughout most of Manhattan, the Bronx, and Staten Island, the bedrock depths are shallow enough (usually well under 60 m) that Equation 3.3 will be sufficient for characterizing the subsurface velocity structure above bedrock. However, a deeper representation of the velocity profile is necessary for many sites in Brooklyn and Queens, where the depth to bedrock exceeds 60 m. Therefore, in a similar approach to that of Memphis is taken: because these deeper-sediment locations are located in the Atlantic Coastal Plain, the Gann-Phillips et al. (2024) Coastal Plain $V_S$ model is appended at these depths. Because many of the Coastal Plain sediments in the vicinity of New York City are Pleistocene in age (DeMott et al., 2023; Nikolaou et al., 2001), the Gann-Phillips et al. (2024) velocity model for the Quaternary Pleistocene (QP) unit is selected.

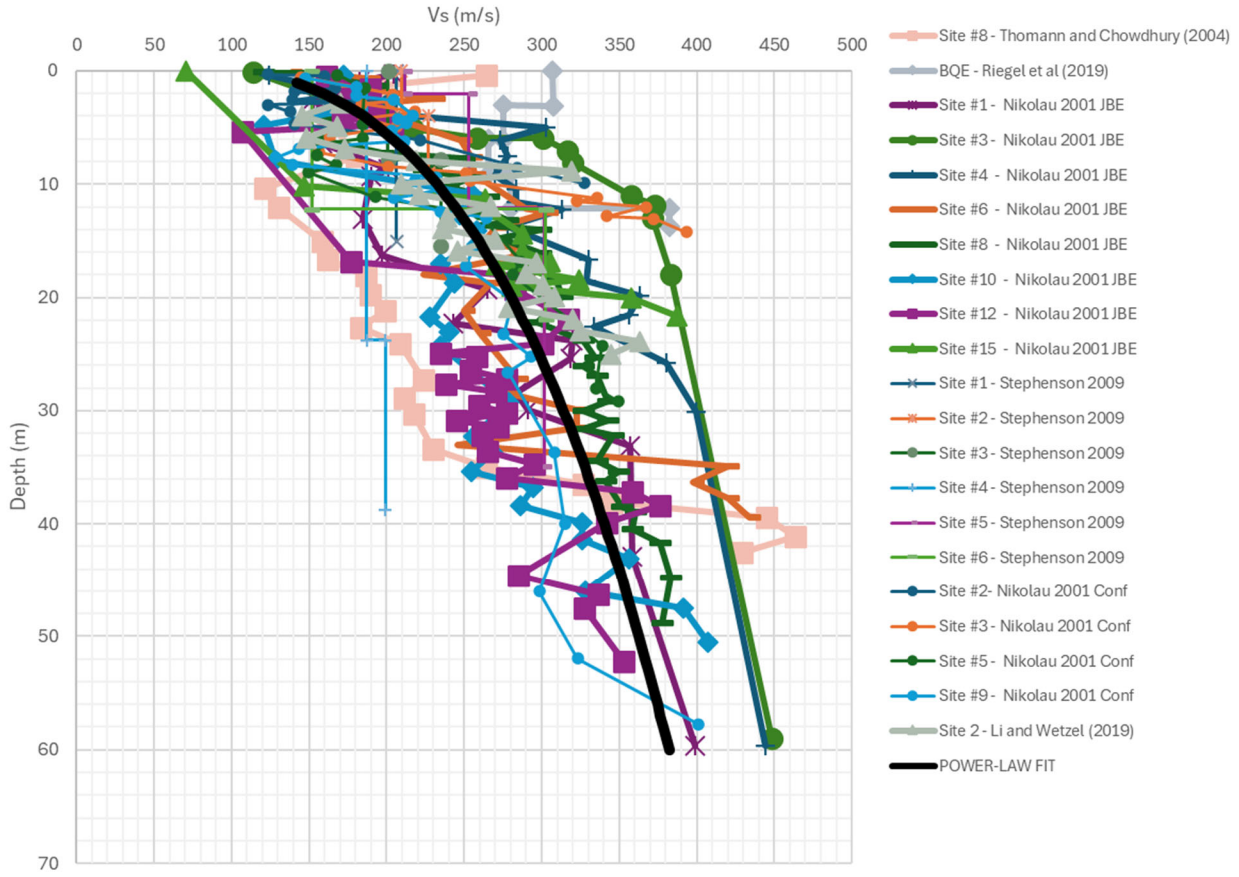


**Figure 3.12.** Near-surface $V_S$ power-law model for New York City (Equation 3.3) for $0 \leq z \leq 60$ m, overlain on the database of 21 $V_S$ profiles used to derive the model.

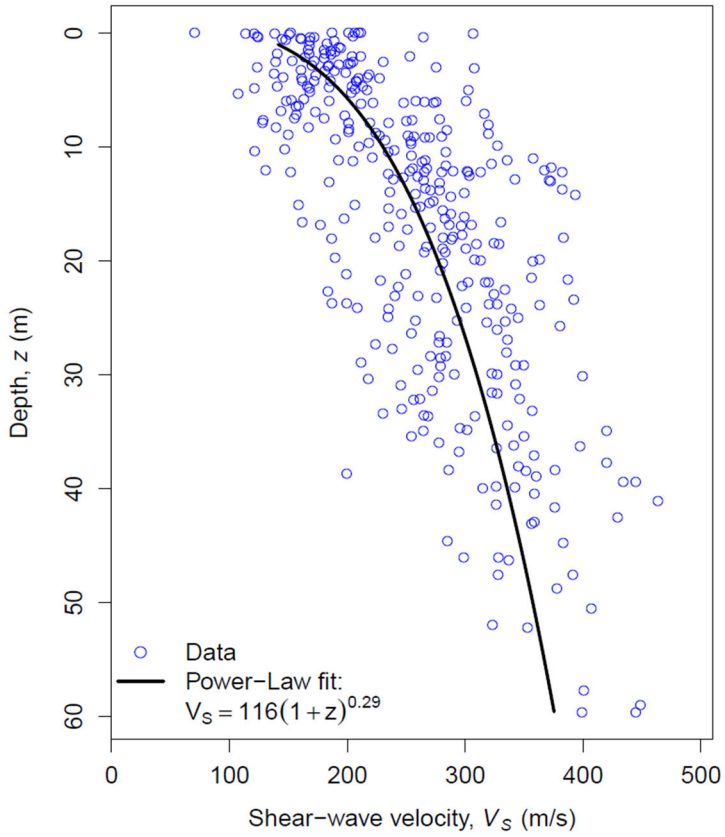


**Figure 3.13.** Near-surface $V_S$ power-law model for New York City (Equation 3.3) for $0 \leq z \leq 60$ m, overlain on data points representing the shear-wave velocity database from Figure 3.11.

Figure 3.14 presents the full $V_S$ model for New York City to a maximum possible depth of 365 m. In site response analyses, the velocity profile is truncated at the depth at which bedrock is reached, so most sites will use a significantly shallower profile. For $0 \leq z \leq 60$ m, we use the New York City-specific power-law model based on published $V_S$ profiles from New York City (Equation 3.3): $V_s = 116(1 + z)^{0.29}$. For $60 < z < 71.5$ m, we employ a linear gradient transition between the New York City-specific power-law model and the Gann-Phillips et al. (2024) QP model to reduce the artificial impedance contrast in transitioning from one velocity model to the next. For 71.5 m $\leq z <$ depth of bedrock, we append the Gann-Phillips et al. (2024) Coastal Plain velocity model for Quaternary Pleistocene (QP) sediments. If the depth to bedrock is less than 71.5 m, the $V_S$ profile is truncated at the depth of bedrock and does not encounter the Gann-Phillips et al. (2024) velocity profile. Beneath the depth to bedrock, we assume a bedrock velocity ($V_{S,bedrock}$) of 2000 m/s, which is consistent with bedrock measurements in New York City from Stephenson et al (2009), as well as Baise et al. (2016) for Boston. Our assumed bedrock velocity of 2000 m/s is less than the commonly assumed value of 3000 m/s for the CEUS (Hashash et al., 2014), and reflects a greater degree of weathering of the bedrock near the surface.

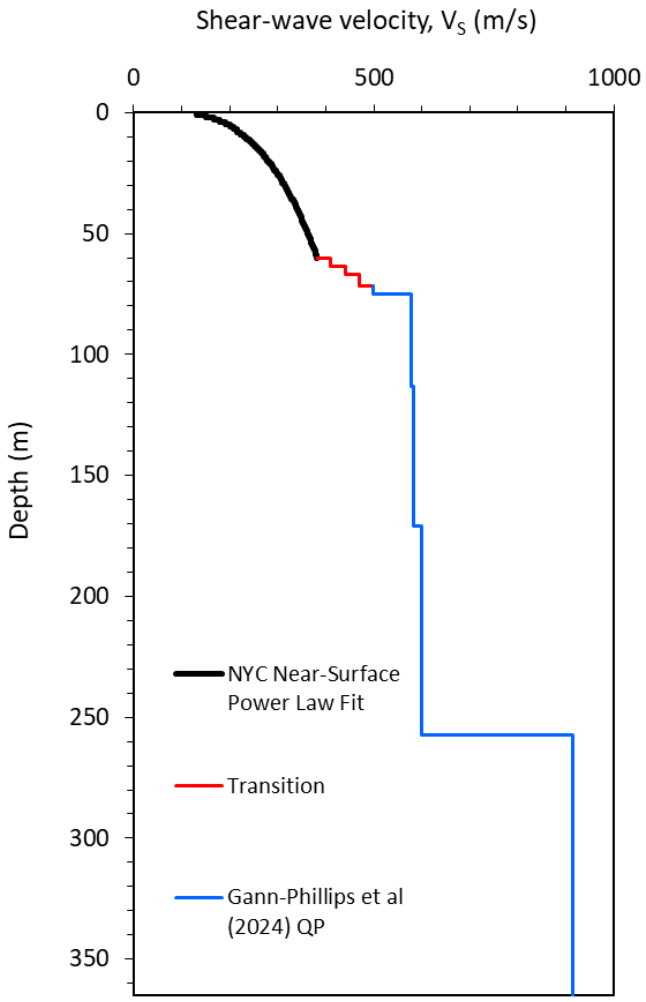


**Figure 3.14.** Full $V_S$ profile for site response analyses in New York City, using Equation 3.3 for depths from 0 to 60 m, a linear gradient transition for depths from 60 to 71.5 m, and the Gann-Phillips et al. (2024) Coastal Plain velocity model for Quaternary Pleistocene (QP) sediments for depths greater than 71.5 m. In site response analyses, the velocity profile is truncated at the depth at which bedrock is reached at a particular site; sediment thicknesses vary in New York City from 0 to 365 m. Beneath the sediment column, a bedrock velocity of $V_{S,bedrock}$ = 2000 m/s is assigned.

Site response was evaluated at a set of three ground-motion stations in the vicinity of New York City. Table 3.3 provides a summary of the seismic stations, including their locations, surface elevation, sediment thickness from DeMott et al. (2023), and average shear-wave velocity ($V_{S30}$). Note that two of the stations have sediment thicknesses less than 30 m, so their $V_{S30}$ computation samples a portion of the bedrock. The first station (LD.CUNY) is located on the campus of Queens College, City University of New York, near the Flushing neighborhood in Queens in the Atlantic Coastal Plain on 150 to 160 m of sediments (NEHRP Site Class D). The second station (LD.CPNY) is located in Central Park in Manhattan on 6 m of sediments, and the third station (LD.FOR) is located on the campus of Fordham University in the Bronx on 8 m of sediments; both of these seismic stations are located outside of the Coastal Plain, and are grouped as NEHRP Site Class C. A color-coded map of the stations and their depths to bedrock is provided in Figure 3.15.

**Table 3.3.** Characteristics of ground-motion recording stations and associated site characterization data in New York City

| Station Code | Station Name / Location | Latitude (deg) | Longitude (deg) | Surface elevation (m) | Sediment thickness (m) | Average shear-wave velocity, $V_{S30}$ (m/s) |
|---|---|---|---|---|---|---|
| LD.CUNY | Queens College, Flushing-Queens, NYC | 40.73493 | -73.81761 | 36 | 158.0 | 237 |
| LD.CPNY | Central Park, New York City | 40.7911 | -73.9602 | 29 | 5.8 | 635 |
| LD.FOR | Fordham University, The Bronx, NYC | 40.8603 | -73.8852 | 32 | 7.9 | 533 |

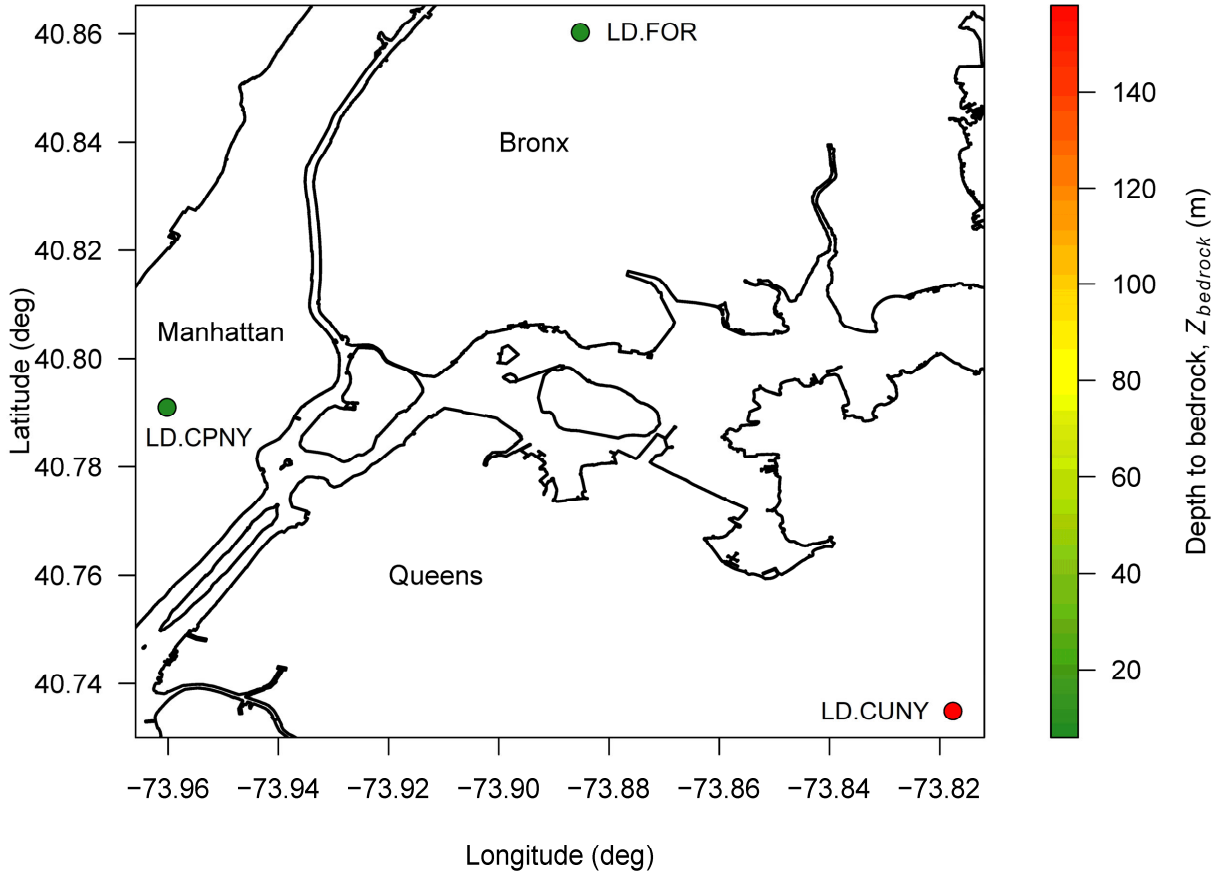


**Figure 3.15.** Map of the three seismic stations from Table 3.3 considered in New York City, colored by depth to bedrock.

## 3.2 Site Response Methodology

This section describes the approach taken for linear site response analyses at all ground-motion stations in Memphis and New York City. We compared the linear amplifications of our ergodic site amplification model (described in Chapter 2) and the NGA-East model of Stewart et al. (2020), both of which are applicable to central and eastern North America, with amplification spectra from theoretical one-dimensional linear site response analyses. Therefore, we performed one-dimensional linear site response analyses at each station in Table 3.2 for Memphis and Table 3.3 for New York City. The one-dimensional linear amplification spectrum was the key desired output of the site response analysis.

We computed the linear amplifications using the program NRATTLE (written by C. Mueller with modification by R. Herrmann and distributed with the Boore (2005) program SMSIM. This program implements the Thomson-Haskell matrix method (Haskell, 1953; Thomson, 1950) for one-dimensional linear wave propagation. For our calculations, we adapted NRATTLE for application in the statistical language and environment R (R Core Team, 2024). The fundamental assumptions inherent in the Thomson-Haskell matrix method include: (1) the medium is assumed to consist of laterally constant layers overlying a non-attenuating halfspace; (2) wavefronts are assumed to be planar; (3) damping is assumed to be independent of frequency and strain; and (4) only the SH-wave (the horizontally-polarized component of the S wave) is modeled. We refer to these collective assumptions as the linear SH1D site response model. For each layer in the profile, the Thomson-Haskell matrix method requires the following: layer thickness ($h$), shear-wave velocity ($V_S$), material density ($\rho$), and shear-wave velocity quality factor ($Q_S$). The layer thicknesses and shear-wave velocities are obtained from the station-specific velocity profiles described in Section 3.1. The computation of the material density and quality factor are described in the following paragraphs.

For material density $\rho$ of each layer, we use the density-velocity relations of Boore (2016). The Boore (2016) density model is composed of density-velocity relations for three ranges of the shear-wave velocity $V_S$. To employ the Boore (2016) density model, we first estimate the compression-wave velocity $V_P$ from $V_S$ using the relationship of Brocher (2005), where the units of $V_P$ and $V_S$ are km/s:

$$V_P = 0.9409 + 2.0947\,V_S - 0.8206\,V_S^2 + 0.2683\,V_S^3 - 0.0251\,V_S^4. \tag{3.4}$$

Once $V_P$ and $V_S$ have been determined, the following piecewise function is used to estimate the material density $\rho$ (kg/m$^3$). We adjusted the Boore (2016) model for a minimum density of 1930 kg/m$^3$ as prescribed in the original version of Boore's density model:

$$\rho = \begin{cases} 1930 & \text{for } V_P < 1.5 \\ 1740\,V_P^{\frac{1}{4}} & \text{for } 1.5 \le V_P < 6 \\ 1661.2\,V_P - 472.1\,V_P^2 + 67.1\,V_P^3 - 4.3\,V_P^4 + 0.106\,V_P^5 & \text{for } V_P \ge 6\,. \end{cases} \tag{3.5}$$

The velocity range encompassing most of the profiles is the second piecewise zone (corresponding to $0.30 < V_S < 3.55$ km/s), for which Boore (2016) uses the density-$V_P$ relation of Gardner et al. (1974).

For the shear-wave velocity quality factor ($Q_S$) of each layer, we employ the widely-used relationship of Campbell (2009), which was based on data from the CEUS. Using the layer shear-wave velocity, $Q_S$ is computed as

$$Q_S = 7.17 + 0.0276V_S. \quad (3.6)$$

Note that the small-strain damping ratio ($D_{min}$) and $Q_S$ are related according to the fundamental equation

$$D_{min} = \frac{1}{2Q_S}. \quad (3.7)$$

In addition to the properties of the soil layers ($h$, $V_S$, $\rho$, and $Q_S$), we must specify the shear-wave velocity of the bedrock halfspace ($V_{S,bedrock}$) and the material density of the bedrock halfspace ($\rho_{,bedrock}$) that represents the base of the model under the soil column. As detailed in Section 3.1, we assume $V_{S,bedrock}$ = 3000 m/s for Memphis and $V_{S,bedrock}$ = 2000 m/s for New York City. We assume $\rho_{,bedrock}$ = 2600 kg/m$^3$ for all locations; this density is consistent with $V_{S,bedrock}$ = 3000 m/s for Memphis, but it is also consistent with typical densities of the types of rocks underlying New York City (largely gneiss and schist).

## 3.3 Site Response Results and Comparisons

This section describes the results of our linear site response analyses at all ground-motion stations in Memphis and New York City. In addition, we compare linear amplifications of our ergodic site amplification model (described in Chapter 2) and the model of Stewart et al. (2020) with amplification spectra from theoretical one-dimensional linear site response analyses.

### 3.3.1 Memphis, Tennessee

As an example of the results, we provide the linear amplification spectra for two stations in Memphis: Stations NM.CUET and NM.MCAR. First, we consider station NM.CUET (CUSEC HQ), located in Memphis, Tennessee, south of the airport and near the state border with Mississippi. The site is located on 1185 m of sediments and has a $V_{S30}$ of 285 m/s; the development of the $V_S$ profile for this site was illustrated in Figures 3.8 and 3.9. Second, we consider station NM.MCAR (Mid-South Community College), located across the Mississippi River in West Memphis, Arkansas. The site is located on 1260 m of sediments and has the lowest value of $V_{S30}$ (189 m/s) of any station we considered in Memphis.

Figures 3.16 and 3.17 illustrate the amplification spectra for Station NM.CUET and NM.MCAR, respectively. In each figure, we show (a) the $V_S$ profile, (b) the amplification spectrum vs. frequency, and (c) the amplification spectrum vs. spectral period. From the first (lowest-frequency) peak of the amplification spectrum, we identify the fundamental frequency ($f_0$) and its associated amplification ratio ($A_0$). In addition, we identify the peak amplification ($A_p$) and its associated frequency ($f_p$). From the inverse of $f_0$ and $f_p$, we also identify the fundamental period ($T_0$) and the period of the maximum amplification ($T_p$). In order to evaluate average amplifications in the context of common design codes, we calculated the mean amplitude of the amplification spectrum over the short period ($F_a$: 0.1–0.5 s) and the intermediate-period ($F_v$: 0.5–1.5 s) ranges.

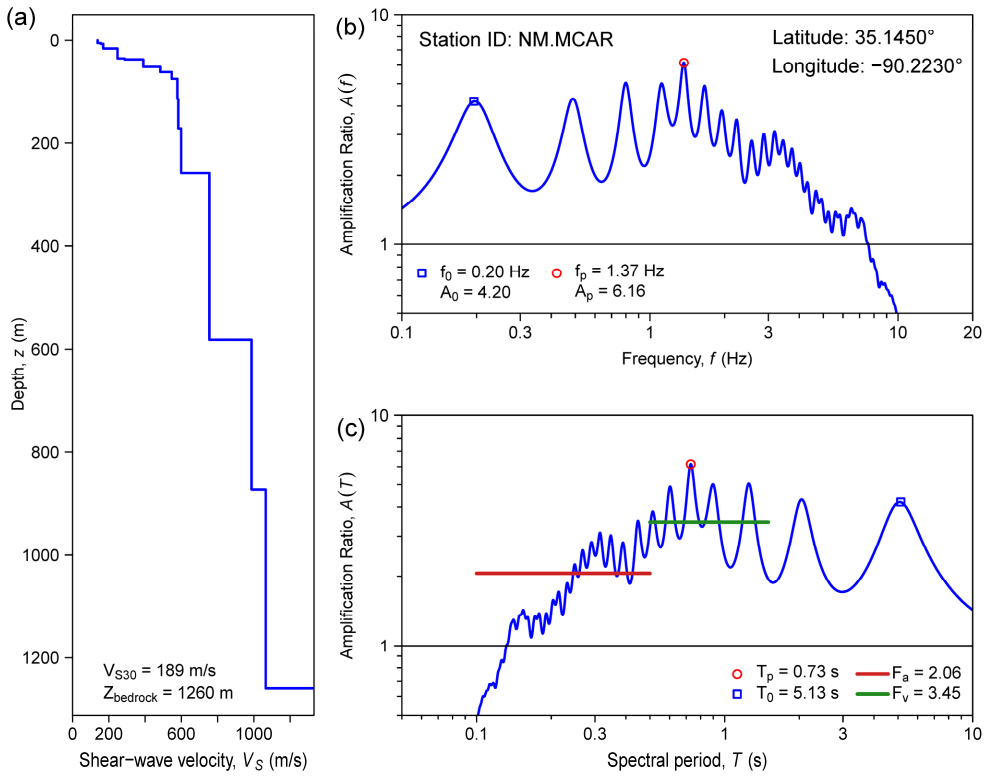


**Figure 3.16.** Plots of (a) the $V_S$ profile, (b) the amplification spectrum vs. frequency, and (c) the amplification spectrum vs. spectral period, computed using linear 1D theoretical site response analyses at station NM.MCAR.

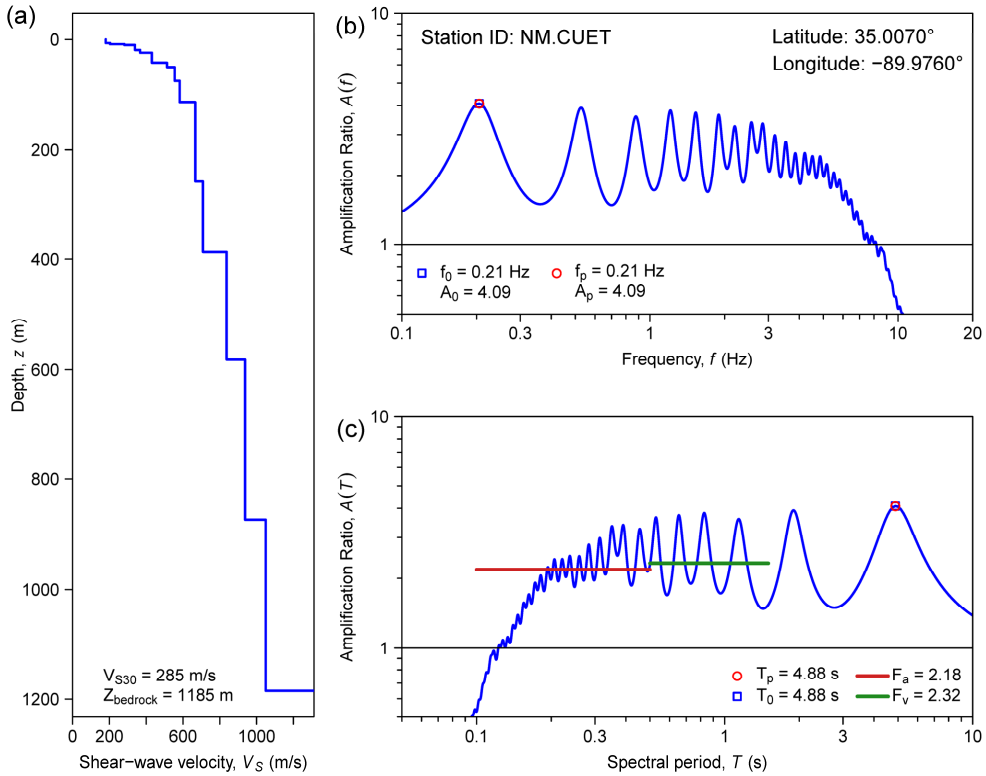


**Figure 3.17.** Plots of (a) the $V_S$ profile, (b) the amplification spectrum vs. frequency, and (c) the amplification spectrum vs. spectral period, computed using linear 1D theoretical site response analyses at station NM.CUET.

In general, the linear 1D amplification spectra for these two deep soil sites display similar trends: fundamental frequencies near 0.2 Hz and associated amplification ratios slightly greater than 4, several higher modes with similar or slightly greater amplifications than the fundamental mode, and a lack of amplification of higher frequencies (> 10 Hz). Station NM.CUET has a $V_{S30}$ approximately 100 m/s greater than station NM.MCAR, and has a sediment thickness 75 m less. For Station NM.CUET, the peak amplification occurs at the fundamental mode, and the mean short- and intermediate-period amplitudes ($F_a$ and $F_v$) are both similar. On the other hand, the station on softer soil (NM.MCAR) has a peak amplification of 6.16 (the greatest of any site) that occurs in a higher mode; there are noticeably greater mean amplifications at longer periods than shorter periods ($F_v$ exceeds $F_a$).

Table 3.4 displays the results of the linear 1D site response analyses for all 21 stations in Memphis. Most stations have fundamental frequencies in the vicinity of 0.2 Hz (fundamental periods between 4 and 5 s) and associated amplification ratios between 4 and 5 at the fundamental mode. The two southeasternmost stations (ZL.A02.HH and ZL.A01), located in Mississippi, are on shallower soil than the stations closer to Memphis, and they have slightly greater fundamental frequencies (near 0.6 Hz) and associated amplification ratios between 3 and 4. The peak amplification at many stations occurs at a higher mode (generally between 1 and 2 Hz) and falls in the range of 4 to 6. The mean amplifications are slightly greater for longer periods than shorter periods, reflecting the longer-period response that is critical for deep soil sites. Across all 21 stations, the average $F_a$ (spanning the 0.1 to 0.5 s range) is 2.09, and the average $F_v$ (spanning to 0.5 to 1.5 s range) is 2.84.

Figures 3.18 through 3.23 plot the spatial distribution of depth to bedrock, $f_0$, $A_0$, $F_a$, and $F_v$, respectively, on a map of the Memphis area. A clear pattern in the depth to bedrock in Figure 2.18 is observed, with greater values closer to the Mississippi River (the border with Arkansas). The fundamental frequency exhibits a narrow range across most sites, as seen in Figure 3.19, but $f_0$ is noticeably larger at the two southernmost sites noted in the previous paragraph. Figure 3.20 shows that the amplification $A_0$ at the fundamental frequency is greatest at the sites in the northern area of the study and smallest at the two southernmost sites, but the range is generally small. Similarly, $F_a$ shows a relatively narrow range across most sites (Figure 3.21), although it is largest at the two southernmost stations. Finally, Figure 3.22 shows that $F_v$ has a relatively heterogenous spatial pattern, as the particular value depends heavily on the individual amplification spectrum at each site.

**Table 3.4.** Parameters from linear 1D theoretical site response calculations at Memphis ground-motion recording stations.

| | Properties of fundamental mode | | | Properties of peak amplification | | | Mean amplifications | |
|---|---|---|---|---|---|---|---|---|
| Station Code | $f_0$ (Hz) | $T_0$ (s) | $A_0$ | $f_p$ (Hz) | $T_p$ (s) | $A_p$ | $F_a$ (0.1–0.5 s) | $F_v$ (0.5–1.5 s) |
| NM.MKAR | 0.23 | 4.44 | 4.38 | 0.89 | 1.13 | 6.02 | 1.78 | 3.41 |
| NM.LPAR | 0.22 | 4.55 | 4.35 | 0.86 | 1.16 | 5.98 | 1.89 | 3.28 |
| ZL.C05 | 0.23 | 4.44 | 4.45 | 1.34 | 0.75 | 4.72 | 2.32 | 2.71 |
| NM.MCAR | 0.20 | 5.13 | 4.20 | 1.37 | 0.73 | 6.16 | 2.06 | 3.45 |
| NM.HDBT | 0.20 | 5.00 | 4.27 | 0.81 | 1.24 | 5.10 | 1.73 | 3.01 |
| ZL.A04 | 0.20 | 5.13 | 4.16 | 1.43 | 0.70 | 4.47 | 2.08 | 2.64 |
| NM.SFTN | 0.19 | 5.26 | 4.03 | 1.11 | 0.90 | 4.93 | 1.83 | 2.92 |
| ZL.A04X | 0.20 | 5.13 | 4.04 | 1.12 | 0.90 | 4.94 | 1.83 | 2.92 |
| AO.OSAR | 0.22 | 4.65 | 4.32 | 1.53 | 0.66 | 4.74 | 2.28 | 2.71 |
| NM.RDST2 | 0.21 | 4.88 | 4.10 | 1.18 | 0.85 | 4.30 | 1.69 | 2.53 |
| NM.GILT | 0.20 | 5.00 | 4.03 | 1.51 | 0.66 | 4.82 | 2.24 | 2.62 |
| NM.CUET | 0.21 | 4.88 | 4.09 | 0.21 | 4.88 | 4.09 | 2.18 | 2.32 |
| NM.MPH | 0.21 | 4.88 | 4.09 | 0.21 | 4.88 | 4.09 | 2.05 | 2.15 |
| TA.V44A | 0.22 | 4.65 | 4.35 | 1.56 | 0.64 | 4.70 | 2.27 | 2.72 |
| NM.CBHT | 0.22 | 4.65 | 4.14 | 1.24 | 0.81 | 5.41 | 1.88 | 2.94 |
| TA.W44A | 0.22 | 4.55 | 4.18 | 1.24 | 0.81 | 5.71 | 1.91 | 3.11 |
| NM.NAIT | 0.22 | 4.55 | 4.19 | 1.25 | 0.80 | 5.70 | 1.91 | 3.11 |
| NM.COLT | 0.24 | 4.25 | 4.29 | 0.24 | 4.25 | 4.29 | 1.58 | 2.13 |
| ZL.A02.HH | 0.57 | 1.77 | 3.44 | 2.87 | 0.35 | 4.65 | 3.26 | 2.98 |
| NM.CVTN | 0.22 | 4.55 | 4.26 | 1.27 | 0.79 | 5.20 | 1.79 | 2.93 |
| ZL.A01 | 0.59 | 1.69 | 3.88 | 3.18 | 0.31 | 5.03 | 3.23 | 2.98 |

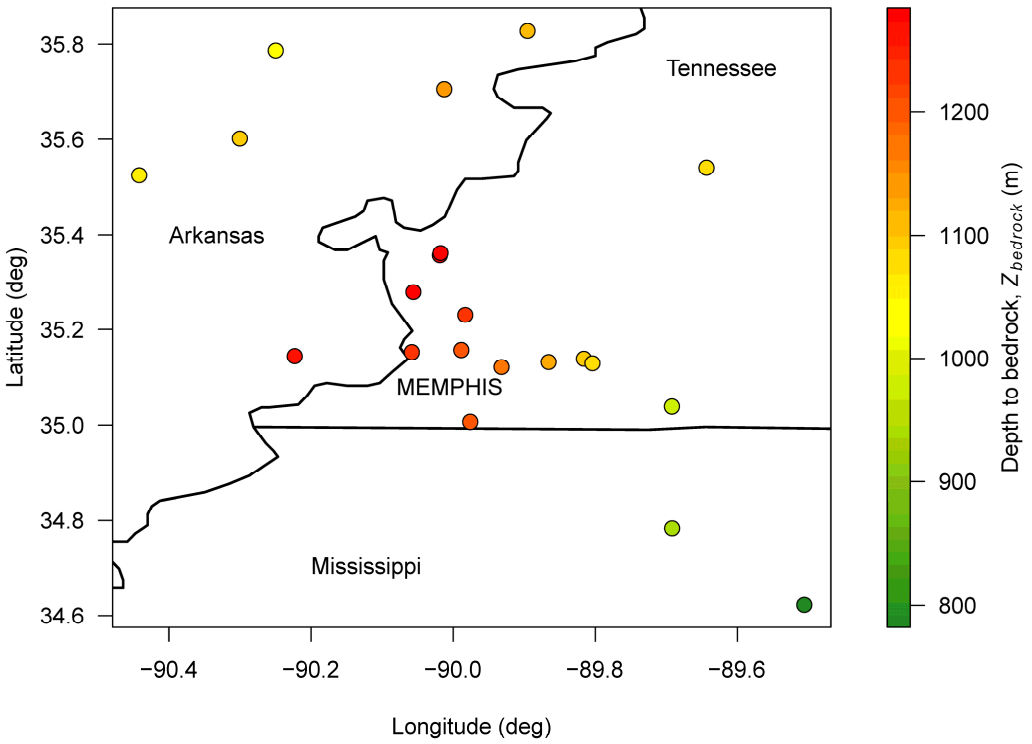


**Figure 3.18.** Map of the 21 seismic stations from Table 3.1 considered in Memphis, colored by depth to bedrock ($Z_{bedrock}$).

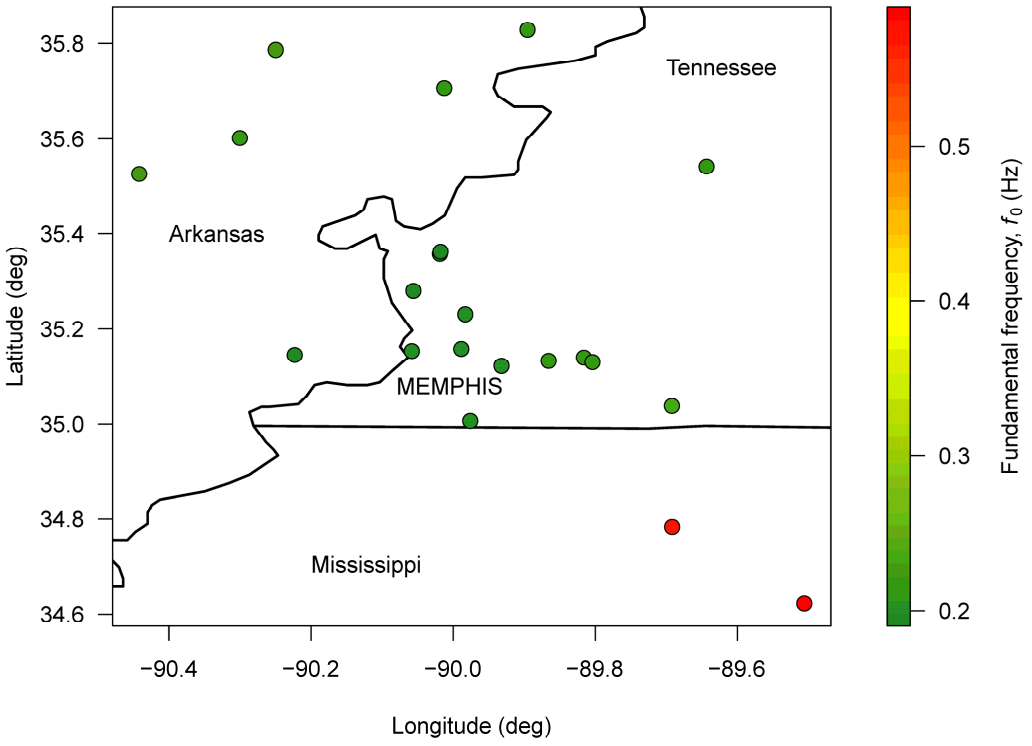


**Figure 3.19.** Map of the 21 seismic stations from Table 3.1 considered in Memphis, colored by fundamental frequency ($f_0$) determined from the theoretical 1D linear amplification spectrum.

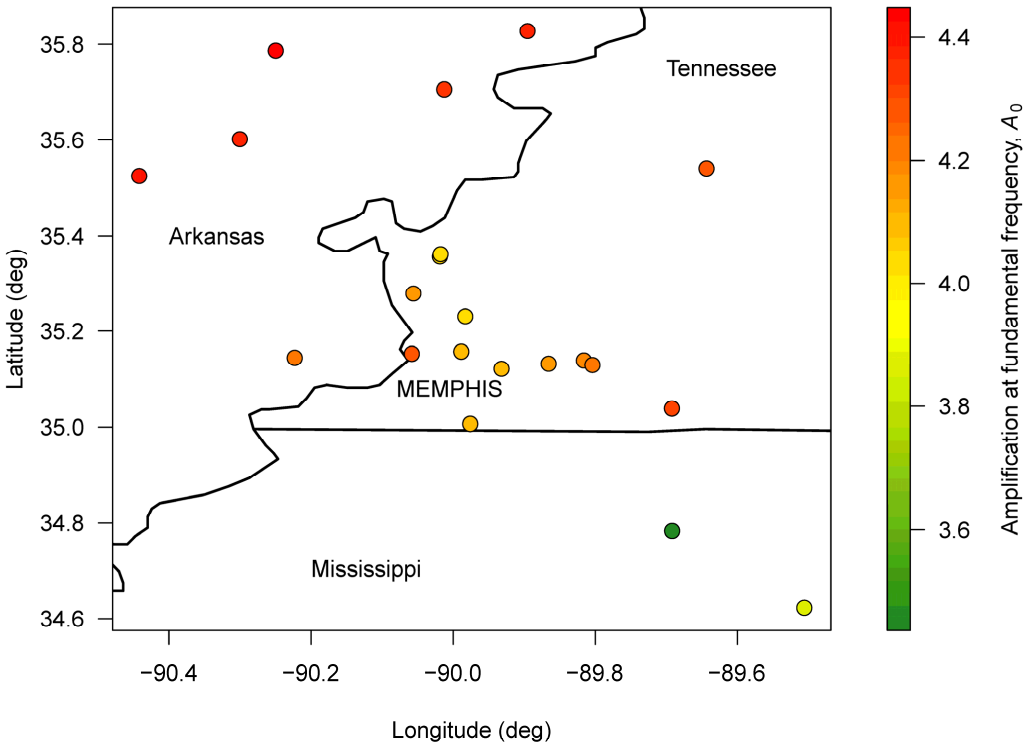


**Figure 3.20.** Map of the 21 seismic stations from Table 3.1 considered in Memphis, colored by the amplification $A_0$ at the fundamental frequency, as determined from the theoretical linear SH1D site response calculation.

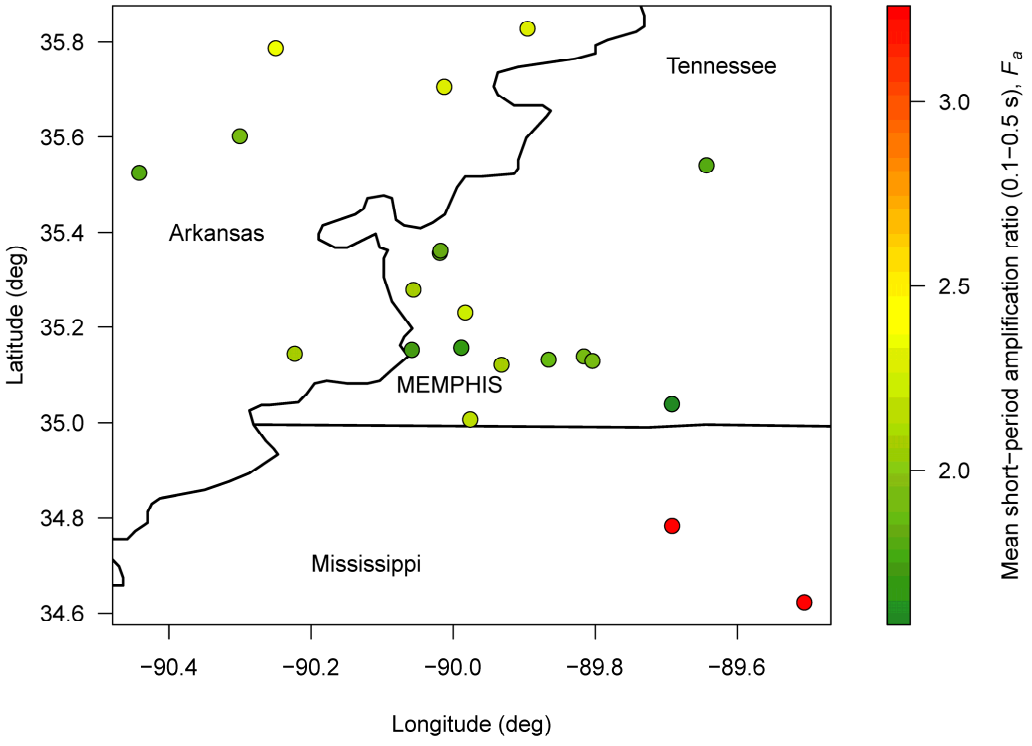


**Figure 3.21.** Map of the 21 seismic stations from Table 3.1 considered in Memphis, colored by the mean short-period amplification ratio ($F_a$) over the 0.1 to 0.5 s range.

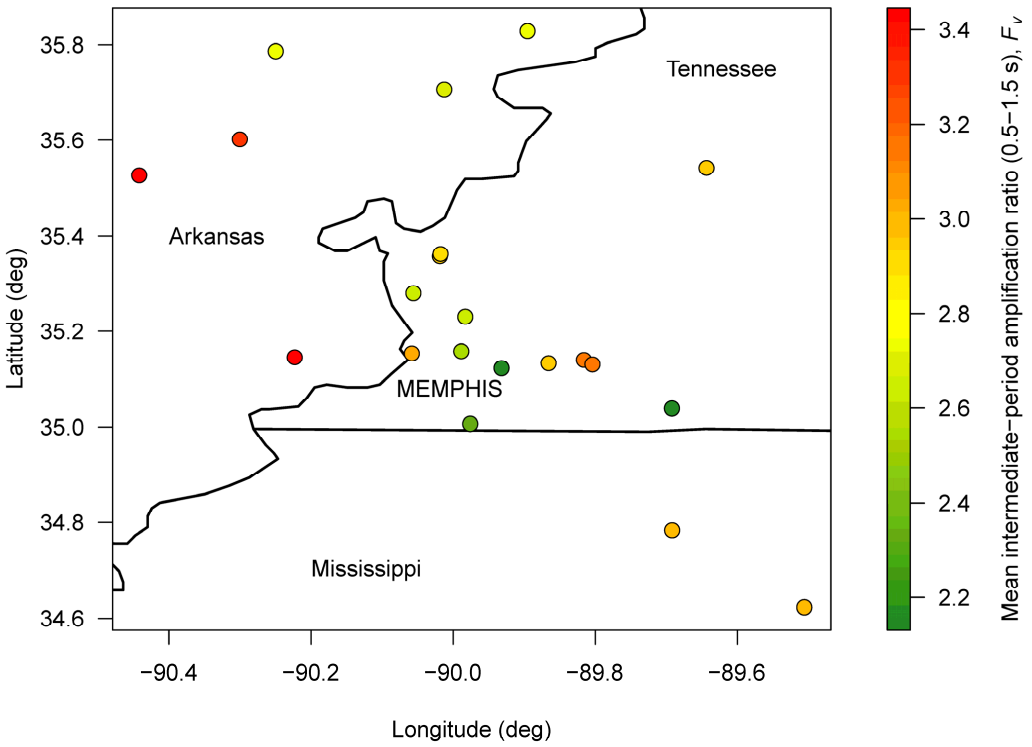


**Figure 3.22.** Map of the 21 seismic stations from Table 3.1 considered in Memphis, colored by the mean intermediate-period amplification ratio ($F_v$) over the 0.5 to 1.5 s range.

Next, we compare the theoretical 1D linear amplification spectra with linear amplifications of our ergodic site amplification model (described in Chapter 2) and the model of Stewart et al. (2020) for central and eastern North America. First, to visualize the differences in the amplifications at a sample of stations, we plot the amplification spectra from these alternate methods at Station NM.CUET and NM.MCAR, previously evaluated in Figures 3.16 and 3.17, respectively. For our model and that of Stewart et al. (2020), the linear amplification ratios are computed by exponentiating the linear amplification term $F_{linear}$, which is constructed in natural logarithmic space: Amplification = exp($F_{linear}$). Figure 3.23 displays a comparison of the amplification spectra for Stations NM.CUET and NM.MCAR.

Figure 3.23 shows that both our ergodic model and that of Stewart et al. (2020) provide amplifications that capture the general shape of the theoretical 1D linear amplification spectrum, but, as expected, cannot replicate the individual peaks of the transfer function. Despite having different functional forms, our model provides similar trends in amplifications to Stewart et al. (2020). Particularly for the softer site (NM.MCAR), our model predicts larger amplifications at longer periods and more accurately captures the peak amplifications in this range. Neither ergodic model accurately captures the drop-off in amplifications at short periods (high frequencies) in the deep soil column.

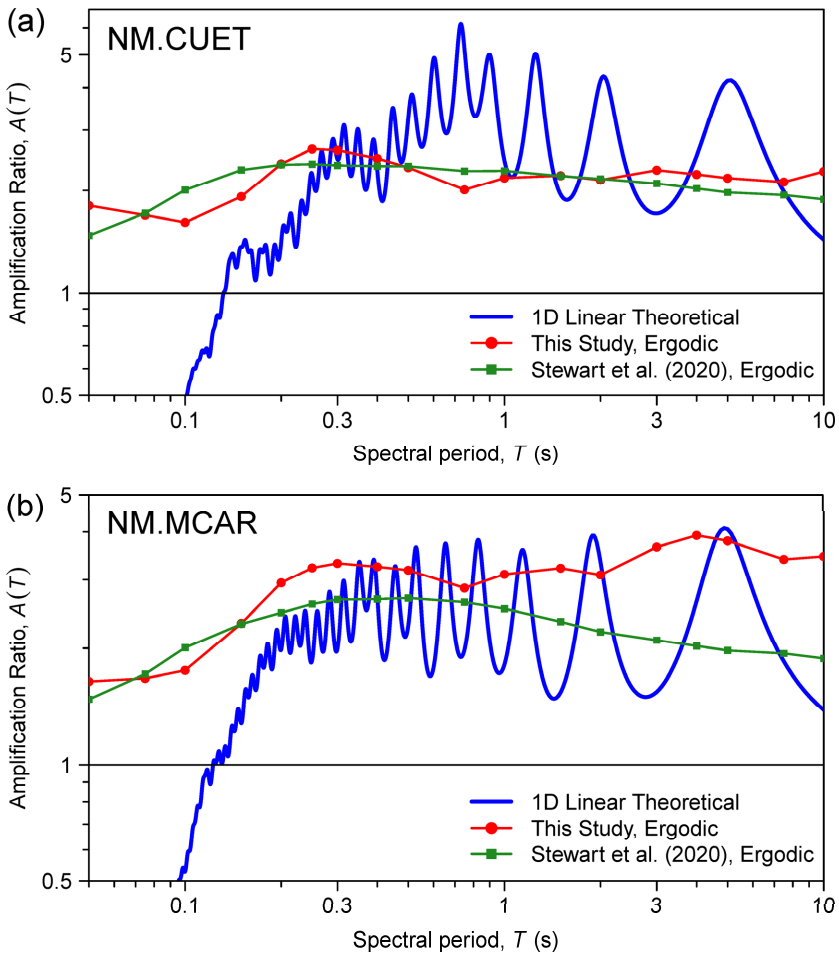


**Figure 3.23.** Comparison of amplification spectra from linear 1D theoretical site response analyses, the ergodic model developed in this study, and the ergodic model of Stewart et al. (2020) at stations (a) NM.CUET and (b) NM.MCAR.

Figure 3.24 provides comparison plots of the mean short-period amplification ($F_a$) over the 0.1–0.5 s range, and the mean intermediate-period amplification ($F_v$) over the 0.5–1.5 s range. The mean amplifications from the theoretical 1D linear site response analysis are shown on the horizontal axis, and the mean amplifications from the ergodic site amplification models are shown on the vertical axis. Across all sites in Memphis, our model offers greater mean amplifications at both period ranges compared to the Stewart et al. (2020) model. At short periods, both models tend to overpredict $F_a$ (more data points located above the 1:1 line), with our model exhibiting slightly greater bias than the Stewart et al. (2020) model. In terms of $F_a$, relative to the values predicted from theoretical 1D linear site response, the root mean square error (RMSE) of our model is 0.71, compared to 0.57 for Stewart et al. (2020). However, at longer periods, our model offers less biased predictions of $F_v$ than Stewart et al. (2020); our data points tend to be more clustered around the 1:1 line, while the Stewart et al. (2020) model tends to underpredict $F_v$. Our model has a root mean square error of 0.58 for $F_v$, compared to 0.77 for Stewart et al. (2020). The fact that sediment thickness is a primary explanatory variable in our model is consistent with the better performance of our model at longer periods, because sediment thickness is more correlated to long-period response in deep sedimentary basins like the Mississippi Embayment.

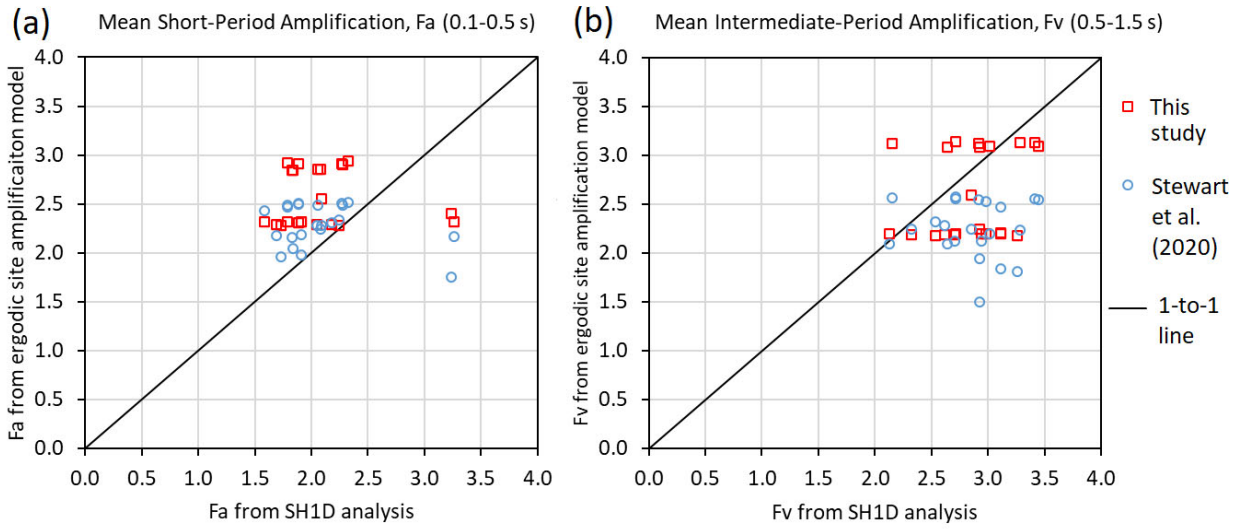


**Figure 3.24.** Comparison plots of (a) the mean short-period amplification ($F_a$) over the 0.1–0.5 s range, and (b) the mean intermediate-period amplification ($F_v$) over the 0.5–1.5 s range, for ground-motion stations in Memphis. In each plot, the mean amplifications from the theoretical 1D linear site response analysis are shown on the horizontal axis, and the mean amplifications from the ergodic site amplification models (both our model and that of Stewart et al. [2020]) are shown on the vertical axis.

### 3.3.2 New York City, New York

Similar site response analyses were performed for the three stations we considered in New York City. In an analogous manner to Section 3.3.1 for Memphis, we first compare the results of theoretical 1D linear site response analyses at two example stations, then provide details of the site response predictions for all three stations, and finally compare the theoretical 1D predictions with those from ergodic site amplification models.

First, we provide representative results at two ground-motion stations in New York City. Station LD.CUNY (Queens College, Flushing-Queens) is located within the Atlantic Coastal Plain in Queens on 158 m of sediments, and has a $V_{S30}$ of 237 m/s (the lowest of the three stations). On the other hand, Station LD.CPNY (Central Park) is located on a shallow soil profile (6 m of sediments) in Central Park in Manhattan, and has a $V_{S30}$ of 635 m/s (the stiffest of the three stations). Figures 3.25 and 3.26 illustrate the amplification spectra for Station LD.CUNY and LD.CPNY, respectively. In each figure, we show (a) the $V_S$ profile, (b) the amplification spectrum vs. frequency, and (c) the amplification spectrum vs. spectral period. From the first (lowest-frequency) peak of the amplification spectrum, we identify $f_0$, $T_0$, and $A_0$, in a similar manner to Memphis. Unlike many of the stations in Memphis, the first peak of the amplification spectrum provides the maximum amplification at any spectral period, so $f_p$, $T_p$, and $A_p$ are the same as $f_0$, $T_0$, and $A_0$, respectively. Finally, we also provide the mean amplifications $F_a$ and $F_v$ over the 0.1–0.5 s and 0.5–1.5 s ranges, respectively.

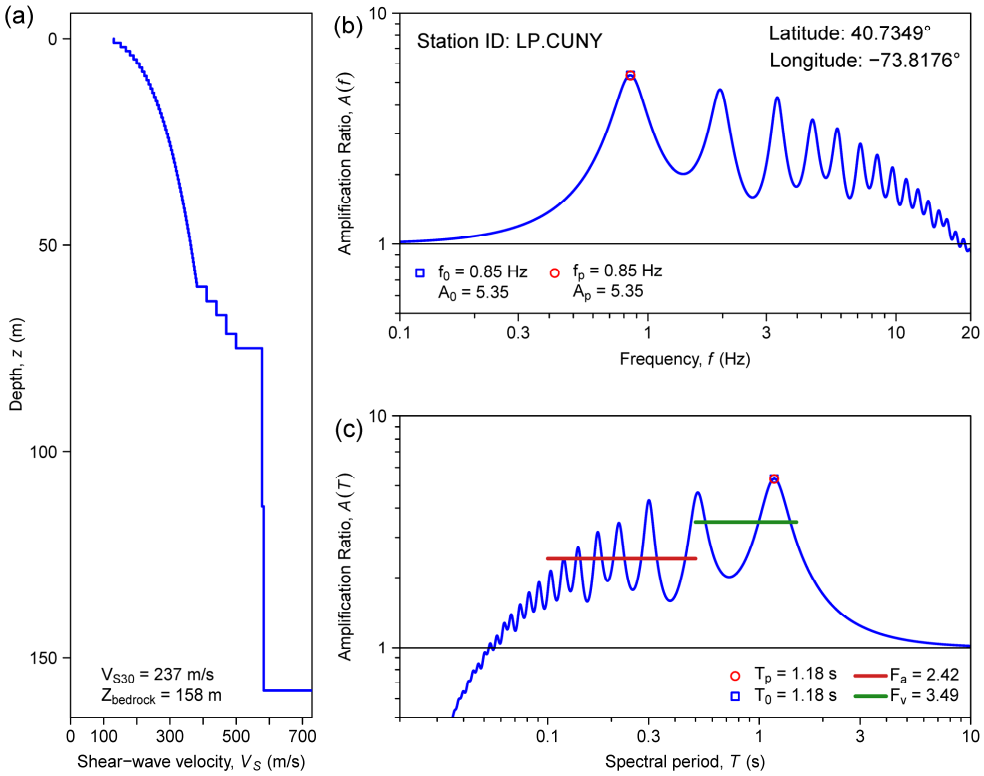


**Figure 3.25.** Plots of (a) the $V_S$ profile, (b) the amplification spectrum vs. frequency, and (c) the amplification spectrum vs. spectral period, computed using linear 1D theoretical site response analyses at station LD.CUNY.

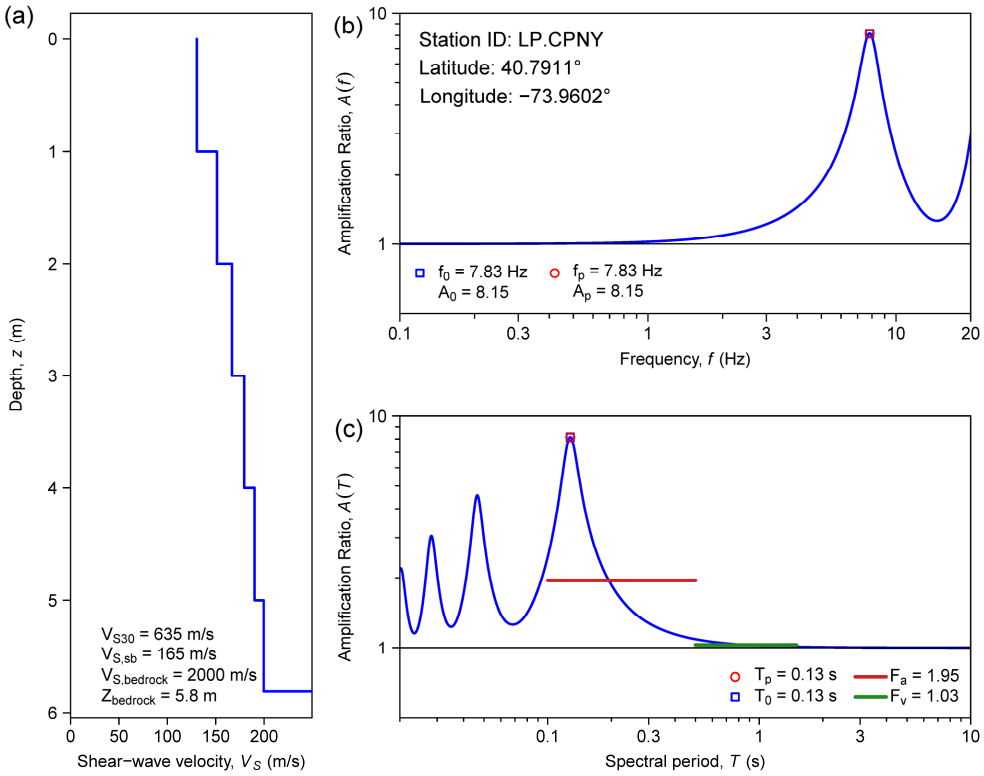


**Figure 3.26.** Plots of (a) the $V_S$ profile, (b) the amplification spectrum vs. frequency, and (c) the amplification spectrum vs. spectral period, computed using linear 1D theoretical site response analyses at station LD.CPNY.

The linear 1D amplification spectra for these two sites have significantly different patterns. The response at the deep soil site (LD.CUNY) is characterized by significantly longer-period response (fundamental period of 1.18 s, maximum amplification of 5.35) than the shallow soil site at LD.CPNY (fundamental period of 0.13 s, maximum amplification of 8.15). The maximum amplification at LD.CUNY is noticeably higher than the deep soil site, although it is at a much shorter period, illustrating the unique challenges associated with ground-motion amplification at shallow soil sites. Similar observations were studied in Boston by Baise et al. (2016). For the deep soil site (LD.CUNY), $F_v$ is noticeably greater than $F_a$, and the inverse is true for the shallow soil site (LD.CPNY). Because the amplification spectrum at LD.CPNY is so sharp and occurs at a shorter period than the full range characterized by $F_a$ and $F_v$, the mean amplifications are not as meaningful at the shallow soil site ($F_v$, for example, represents hardly any amplification at all). Baise et al. (2016) noted similar challenges with mean amplification ratios in shallow-soil, high impedance contrast environments such as many locations in the Northeast.

Table 3.5 displays the results of the linear 1D site response analyses for all three stations in New York City. Significantly different patterns are observed for the two shallow soil sites (LD.CPNY in Manhattan, and LD.FOR in the Bronx) compared to the deep soil site (LD.CUNY in Queens). LD.FOR has a similar amplification pattern to LD.CPNY as described in the previous paragraph: a short fundamental period, a significant peak in the amplification spectrum (maximum amplification ratio of 8) due to the sharp impedance contrast near the ground surface, and a value of $F_a$ significantly higher than $F_v$. Figures 3.27 to 3.30 plot the spatial distribution of $f_0$, $A_0$, $F_a$, and $F_v$, respectively, on a map of the New York City area. Figure 3.15 previously provided the spatial distribution of depth to bedrock. Traversing from northwest (shallow soil) to southeast (deep soil), we can observe a clear increase in depth to bedrock, $T_0$, and $F_v$, and a clear decrease in $f_0$ and $A_0$.

**Table 3.5.** Parameters from linear 1D theoretical site response calculations at New York City ground-motion recording stations.

| | Properties of fundamental mode | | | Properties of peak amplification | | | Mean amplifications | |
|---|---|---|---|---|---|---|---|---|
| Station Code | $f_0$ (Hz) | $T_0$ (s) | $A_0$ | $f_p$ (Hz) | $T_p$ (s) | $A_p$ | $F_a$ (0.1–0.5 s) | $F_v$ (0.5–1.5 s) |
| LD.CUNY | 0.85 | 1.18 | 5.35 | 0.85 | 1.18 | 5.35 | 2.42 | 3.49 |
| LD.CPNY | 7.83 | 0.128 | 8.15 | 7.83 | 0.128 | 8.15 | 1.95 | 1.03 |
| LD.FOR | 6.16 | 0.162 | 8.03 | 6.16 | 0.162 | 8.03 | 2.22 | 1.05 |

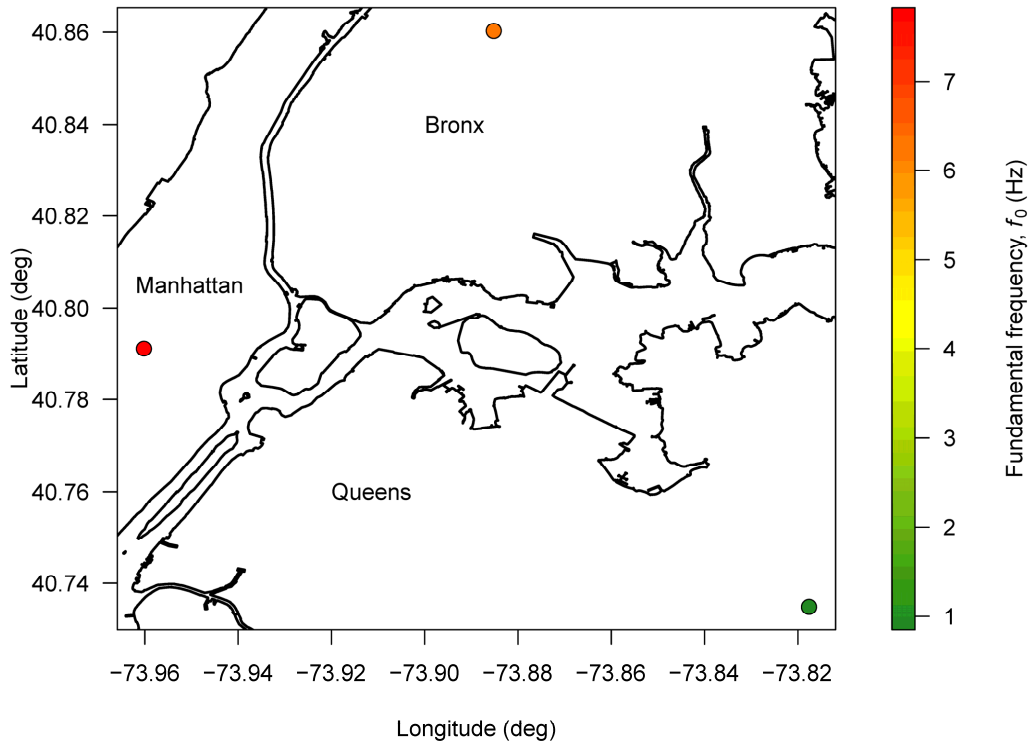


**Figure 3.27.** Map of the three seismic stations from Table 3.3 considered in New York City, colored by fundamental frequency ($f_0$) determined from the theoretical 1D linear amplification spectrum.

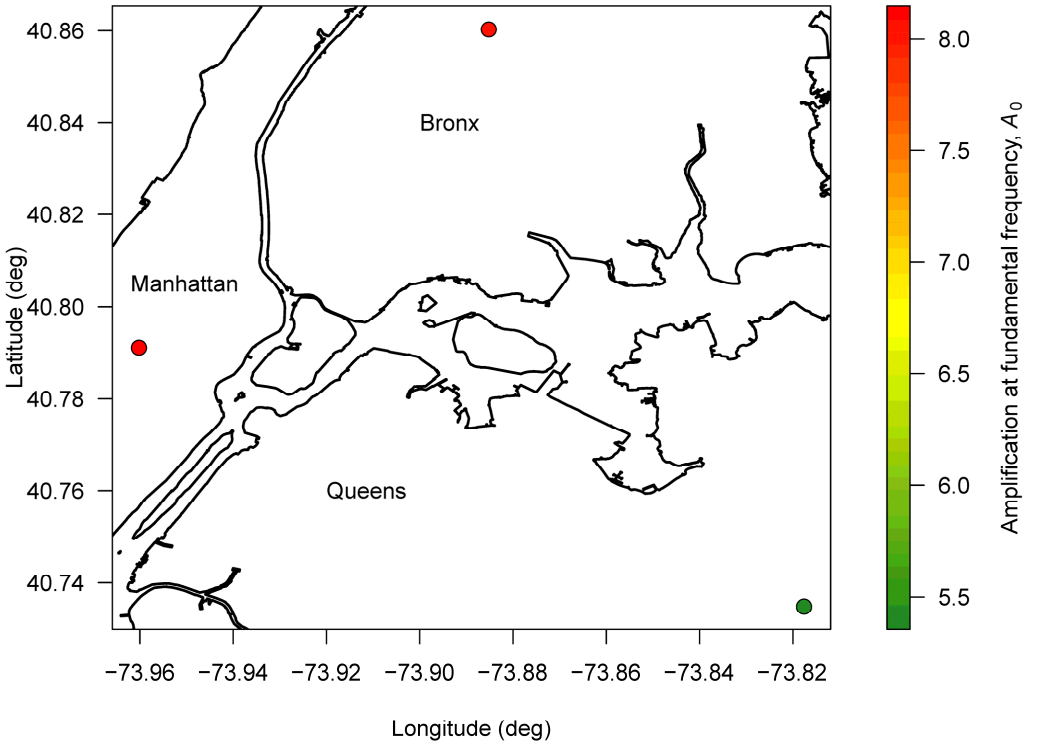


**Figure 3.28.** Map of the three seismic stations from Table 3.3 considered in New York City, colored by the amplification $A_0$ at the fundamental frequency, as determined from the theoretical linear SH1D site response calculation.

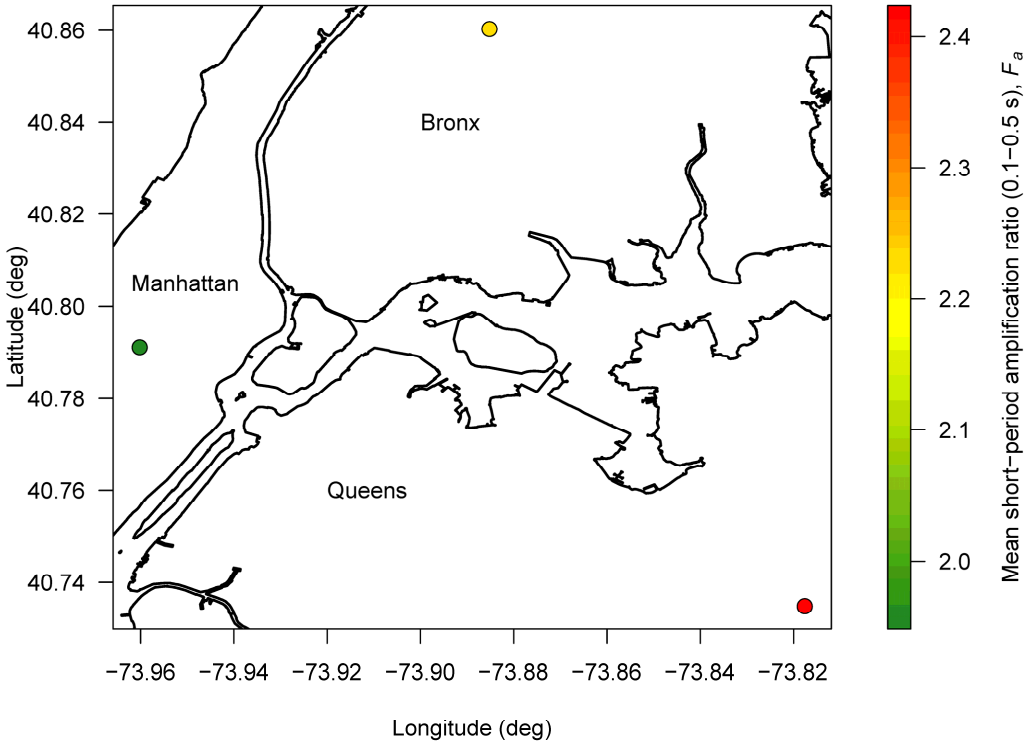


**Figure 3.29.** Map of the three seismic stations from Table 3.3 considered in New York City, colored by the mean short-period amplification ratio ($F_a$) over the 0.1 to 0.5 s range.

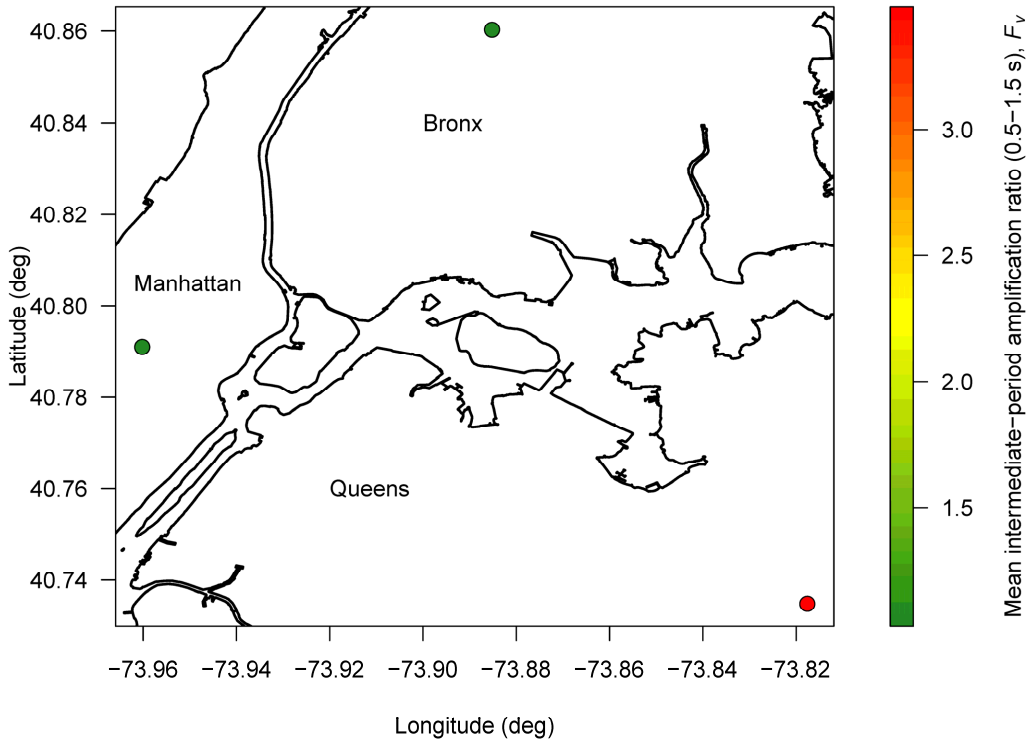


**Figure 3.30.** Map of the three seismic stations from Table 3.3 considered in New York City, colored by the mean intermediate-period amplification ratio ($F_v$) over the 0.5 to 1.5 s range.

Next, we compare the theoretical 1D linear amplification spectra with linear amplifications of our ergodic site amplification model (described in Chapter 2) and the model of Stewart et al. (2020) for central and eastern North America. First, to visualize the differences in the amplifications at a sample of stations, we plot the amplification spectra from these alternate methods at Stations LD.CUNY and LD.CPNY in Figure 3.31. At the deep soil site (LD.CUNY), both our ergodic model and that of Stewart et al. (2020) provide amplifications that capture the general shape of the theoretical 1D linear amplification spectrum, but, as expected, cannot replicate the individual peaks of the transfer function. At the shallow soil site (LD.CPNY), neither ergodic model can accurately capture the significant peak in the amplifications at short periods. The Stewart et al. (2020) model is slightly more accurate at short periods (showing an elevated amplification in the vicinity of the peak), but our ergodic model is slightly more accurate at long periods (showing little to no amplification at periods greater than 0.5 s, consistent with the theoretical site response calculations). At sites with such a strong impedance contrast close to the ground surface (e.g., LD.CPNY), a site-specific ground-response analysis has significant advantages in accurately characterizing the amplification spectrum.

Figure 3.32 provides comparison plots of the mean short-period amplification ($F_a$) over the 0.1–0.5 s range, and the mean intermediate-period amplification ($F_v$) over the 0.5–1.5 s range. The mean amplifications from the theoretical 1D linear site response analysis are shown on the horizontal axis, and the mean amplifications from the ergodic site amplification models are shown on the vertical axis. At short periods, both models underpredict $F_a$ (more data points located below the 1:1 line), with Stewart et al. (2020) offering less bias. In terms of $F_a$, relative to the values predicted from theoretical 1D linear site response, the root mean square error (RMSE) of our model is 0.92, compared to 0.28 for Stewart et al. (2020). The larger RMSE of our model is driven by the underprediction at the two rock sites, likely because we used a coarser sediment thickness model in areas outside of the coastal plain that does not capture the shallow soil layers (e.g., Pelletier et al., 2016). At the two rock sites, our model is predicting almost no amplification at short periods; they behave as hard rock, as suggested by the adjusted province. However, the usage of a finer sediment thickness model of DeMott et al. (2023) in the theoretical 1D linear site response analyses indicates that the shallow soil present has the potential to offer significant amplifications over narrow period ranges. At longer periods, however, both models are more accurate at predicting $F_v$ than $F_a$. Our model has a root mean square error of 0.59 for $F_v$, compared to 0.85 for Stewart et al. (2020). The fact that sediment thickness is a primary explanatory variable in our model is consistent with the better performance of our model at longer periods, particularly at the deep soil Station LD.CUNY. At the two shallow soil stations, however, $F_v$ is less meaningful because there is virtually no amplification at periods longer than 0.5 s.

The analyses in this chapter illustrate the unique challenges associated with evaluating site response for various sediment thicknesses in major CEUS cities. Compared to 1D linear theoretical site response analyses, our ergodic site amplification model is largely in agreement with Stewart et al. (2020), although our model performs slightly worse at shorter periods and better at longer periods. The improved performance of our model at longer periods indicates that the explanatory variables of sediment thickness and adjusted province are useful for estimating site amplifications in the CEUS, especially at sites with greater sediment thickness. However, ergodic site amplification models have challenges in replicating high-resolution site response behavior across urban areas, such as their inability to capture sharp peaks in the theoretical linear amplification spectrum at shallow sites with strong impedance contrasts.

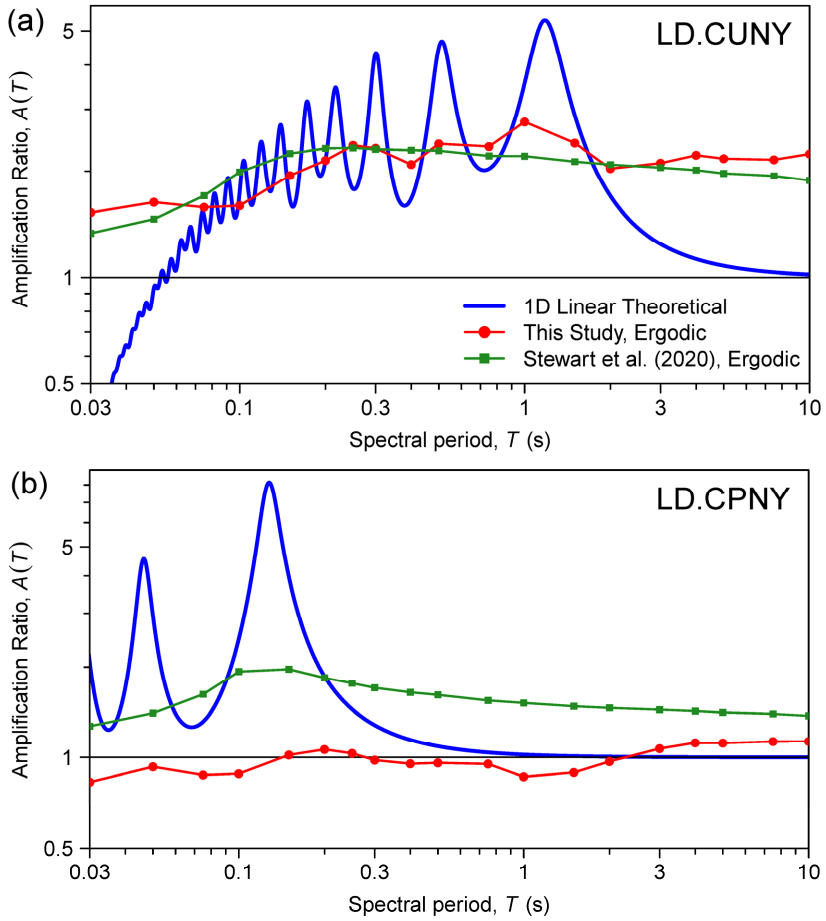


**Figure 3.31.** Comparison of amplification spectra from linear 1D theoretical site response analyses, the ergodic model developed in this study, and the ergodic model of Stewart et al. (2020) at stations (a) LD.CUNY (a deep soil site) and (b) LD.CPNY (a shallow soil site).

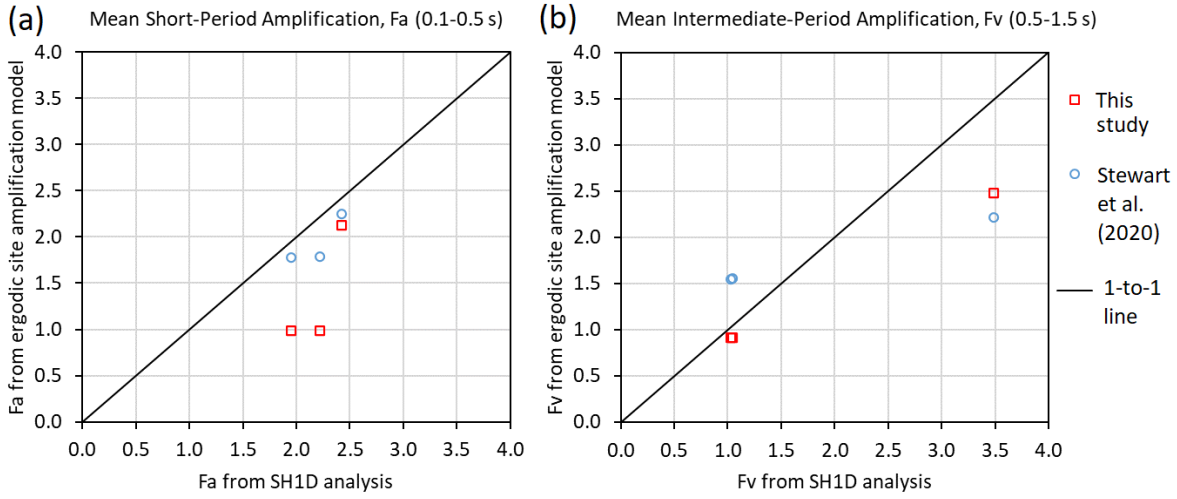


**Figure 3.32.** Comparison plots of (a) the mean short-period amplification ($F_a$) over the 0.1–0.5 s range, and (b) the mean intermediate-period amplification ($F_v$) over the 0.5–1.5 s range, for ground-motion stations in New York City. In each plot, the mean amplifications from the theoretical 1D linear site response analysis are shown on the horizontal axis, and the mean amplifications from the ergodic site amplification models (both our model and that of Stewart et al. [2020]) are shown on the vertical axis.

# Chapter 4: Conclusions

In this study, we propose a new site amplification term for use with CEUS GMMs that is based on geospatial predictor variables (adjusted physiographic province and sediment thickness), and does not rely on site-specific information or inferred $V_{S30}$. We built our model by performing residual analysis using the current $V_{S30}$-based NGA-East linear amplification model residuals to compute site-to-site terms, i.e., the portion of the residual that is due to the amplification at the site. We added these site-to-site terms with the current linear amplification terms at the sites to obtain the total amplification ($A_j$) at each station within our database. We also compiled sediment thickness throughout the CEUS from several alternate models. Because high-quality sediment thickness datasets are not available throughout the entire CEUS, we examined three different regions with higher-quality sediment thickness datasets (Boyd et al., 2024; Soller and Garrity, 2018; and Domrois et al., 2015), as well as one global dataset with coarser spatial resolution (Pelletier et al., 2016).

We initially examined our geospatial predictors using correlation matrices and ANOVA testing for these different regions in the CEUS. Using the insights from the correlation matrices for each region, we simplified our modeling approach. We regionalized the CEUS into two sections: (1) the Atlantic and Gulf Coastal Plains in the southeastern U.S., where the high-quality depth-to-bedrock is available (Boyd et al., 2024); and (2) the northern region of the CEUS, where the lower-resolution dataset (Pelletier et al., 2016) had stronger correlations with amplification than the other tested datasets, as shown in Figures 2.6 and 2.7 (Soller and Garrity, 2018; Domrois et al., 2015). We built models for each of the two regions using the amplification terms $A_j$ as target values, and the continuous/categorical geospatial variables as predictors. To assess each potential model, we used five-fold cross validation to train and test models, computing the average RMSE of the left-out group. Twenty different one-parameter models were evaluated to find the optimum one-parameter model that best predicted total amplification $A_j$ in the CEUS.

The optimal single geospatial variable to predict linear amplification in both regions is the adjusted version of the Fenneman and Johnson (1946) physiographic provinces. In the northern CEUS, the average RMSE using the adjusted province across all periods was 17.4% lower than the average RMSE using $V_{S30}$. In the Coastal Plain, the average RMSE using the adjusted province as the predictor was 17% lower than using $V_{S30}$, and sediment thickness also worked well as a single predictor (with an average RMSE 10.4% lower than $V_{S30}$). Because the optimal single parameter (adjusted physiographic province) is a categorical variable with geographic boundaries, we tested potential two-parameter models by adding possible continuous geospatial terms. We tested eight potential two-parameter models in each region. In the northern region, the Pelletier et al. (2016) sediment thickness dataset provided an additional 1% decrease in average RMSE than using adjusted province alone. In the Coastal Plain, adding the Boyd et al. (2024) sediment thickness as a second parameter to adjusted province lowered the average RMSE by 11.8% versus using adjusted province alone. The high-quality sediment thickness dataset of Boyd et al. (2024) is superior, and the reduced model error highlights the need for similar work in the rest of the CEUS.

Our regionalized two-parameter model for amplification in the CEUS based on physiographic province and sediment thickness. The adjusted versions of the Fenneman and Johnson (1946)

physiographic provinces address the regional trends in site amplification by accounting for large scale geologic structures, such as the Appalachian Mountains, the Superior Upland, and different parts of the Atlantic Coastal Plain. These provinces are divided based on geologic and geomorphologic characteristics, and define large-scale structures within the CEUS. Sediment thickness provides a proxy for soil stiffness and basin structures within these provinces, giving additional insight to linear amplification at a station. Our model reduces the variability in S2S and resolves much of the spatial trend in amplification seen using the current linear amplification model.

To accompany our model development, we examined the city-scale effects of sediment thickness on site response in two CEUS cities that reside within basin structures: Memphis, Tennessee, and New York City, New York. We performed theoretical 1D linear site response analyses to evaluate site response at ground motion stations within these cities, and compare the results with the current $V_{S30}$-based NGA-East linear amplification model (Stewart et al., 2020) and the linear amplification model proposed in this study.

Memphis, Tennessee, is in a location of deep Coastal Plain sediments (approximately 800 to 1300 m) and high seismic hazard (due to its location near the New Madrid Seismic Zone). Theoretical linear 1D site response analyses showed fundamental frequencies mainly around 0.2 Hz and amplification ratios at the fundamental mode between 3.5 and 4.5. Both the Stewart et al. (2020) model and our proposed model overpredicted short-period amplifications compared to the 1D site response analysis, with our model providing larger overpredictions of mean short-period amplifications than Stewart et al. (2020). However, intermediate-to long-period amplifications were more accurately predicted by our model compared to the Stewart et al. (2020) linear amplification model. The fact that our model performed well at longer periods in thick sediments is likely due to using sediment thickness as a parameter, which is correlated with long-period amplification.

In New York City, New York, we analyzed site response at three ground motion stations: two on relatively shallow sediment in Manhattan and the Bronx, and one on deep coastal plain sediments in Queens. The shallow-sediment stations use the lower-quality sediment thickness dataset (Pelletier et al. 2016), while the deeper-sediment station uses the high-quality sediment thickness from Boyd et al. (2024). We see sharply contrasting patterns between the stations, with the deep-sediment station having amplification dominated by long periods, and the shallow-sediment stations showing short fundamental frequencies with amplification dominated by short periods. The two shallow stations show high peak amplification ratios exceeding 8, driven by strong, shallow impedance contrasts. Both the proposed model and the Stewart et al. (2020) model underpredict short-period amplification, with the Stewart et al. (2020) model having a lower RMSE than our proposed model. The larger RMSE is particularly apparent at the shallow-sediment stations, which could stem from the coarser, less accurate sediment thickness data at these stations (from the Pelletier et al. [2016] sediment thickness model). This analysis highlights the need for better sediment thickness data and models outside of the Coastal Plain. For longer-period amplification, both models were less biased, with our proposed model having a lower RMSE compared to the Stewart et al. (2020) linear amplification model.

Chapter 3 also highlights the limitations of ergodic ground-motion modeling and the benefits of site-specific or city-scale ground response analysis within vulnerable cities, especially in capturing changing behavior at a smaller spatial scale. Within deep sedimentary basins, long-period amplification can be adequately characterized using sediment thickness as a parameter. However, shallow soil sites with strong impedance contrasts are poorly modeled using ergodic ground motion models, as shown in this study and previous studies.

In summary, the results of this study work toward the improvement of basin terms in ground motion models, using geospatial, geological, geomorphic, and geotechnical data to characterize sedimentary basins in the Central and Eastern United States. Improved basin terms in ground motion models will reduce the ground-motion uncertainty in probabilistic seismic hazard analyses, and ultimately benefit all those who use regional and local seismic hazard products, including engineers, planners, and loss estimators.

# Data and Resources

The ground motion records used for this analysis were obtained from the PEER NGA-East database (https://ngawest2.berkeley.edu/) and the Central and Eastern U.S. Earthquake Ground Motion Database (https://www.strongmotioncenter.org/specialstudies/thompson2023_ceus/). For all recordings from earthquakes with $M > 4$, the recordings were processed to obtain GMM predictions using the central branch of the NGA-East GMMs (Goulet et al., 2021a), as well as the linear amplification model (Stewart et al., 2020) and the nonlinear amplification model (Hashash et al., 2020), coded and available at https://github.com/wltcwpf/GMPE/blob/main/R/-nga_cena.R For ground motion recordings from earthquakes with magnitudes between 3 and 4, we used the Modified Akima Interpolation in MATLAB (Mathworks, 2023; https://www.mathworks.com/help/matlab/ref-/makima.html) using rupture distance, magnitude, and period following the methods described in Boyd et al. (2024).

The geospatial data used as predictors are described in Table 2.1, including all data references and which terms (Roughness, TPI, Curvature) were derived using elevation data from Jarvis et al. (2008). These terms were derived using ArcGIS Pro. Regional sediment thickness data used in Chapter 2 is outlined in detail with references in Chapter 1.3.1.

Physiographic divisions, provinces, and sections come from Fenneman and Johnson (1946). Detailed insight into the production of the Adjusted Physiographic Provinces is given in Chapter 2.1.4.

Model training, testing, and fitting were performed using the open-source statistical language and environment R (R Core Team, 2024). Figures were created using the statistical language and environment R.

The data compiled for the geotechnical characterization and site response analyses in selected CEUS cities are described in Chapter 3 and Appendix A. No new subsurface data were measured as part of the project. The references described in Chapter 3 and Appendix A detail the publicly available sources of data that were used for the analyses. Relevant data from these resources include shear-wave velocity profiles, depth-to-bedrock measurements, and subsurface exploration reports.

This project is centered on the analysis and processing of electronic data sources (detailed above) and the development of models. We did not collect any geotechnical or seismic data. The outcomes of this project will be disseminated through publication in at least one peer-reviewed journal article. The data generated during this research, including a shapefile of the Adjusted Physiographic Provinces used in our model, will be made available as an electronic supplement accompanying the published article(s), ensuring transparency and accessibility for further research.

# Bibliography

The following is a list of publications and presentations that have resulted from this project. Through the end of 2024, the results from this project have been presented at two conferences, with plans to present aspects of this project at additional conferences in the future. Furthermore, the project team is preparing to publish the results of this project in one or more peer-reviewed journals.


Meyer, E., A. Dioslaki, S. Nie, W. Zhan, J. Kaklamanos, and L. G. Baise (2024). Multi-resolution basin terms for ground motion models in Central and Eastern North America, *2024 Annual Meeting of the Seismological Society of America*, Anchorage, Alaska, 29 April – 3 May 2024 (abstract printed in *Seismological Research Letters*, Vol. 95, No. 2B, p. 1294).

Meyer, E., L. G. Baise, J. Kaklamanos, W. Zhan, S. Nie, and M. Roberts (2024). Province-based ground-motion amplification model for the Central and Eastern U.S., *American Geophysical Union (AGU) Annual Meeting 2024*, Washington, D.C., 9–13 December 2024, abstract S21D-3458.

Meyer, E., M. Roberts, L. G. Baise, S. Nie, J. Kaklamanos, and W. Zhan (in preparation). Province-based ground-motion amplification model for the Central and Eastern U.S. *Manuscript in preparation*.

# References


Abrahamson, N. A., and R. R. Youngs (1992). A stable algorithm for regression analyses using the random effects model, *Bulletin of the Seismological Society of America* **82(1),** 505–510.

Akhani, M., M. Davatgari-Tafreshi, S. Pezeshk (2024). Adjusting Central and Eastern United States ground-motion models for use in the Coastal Plain considering the sediment thickness, *Earthquake Spectra* **40(4),** 2669–2691. DOI: 10.1177/87552930241258354.

Bagley, C. T. (1953). Subsurface study of glacial deposits at Cleveland, Ohio, *Ohio Journal of Science* **53(2),** 65–71.

Baise, L. G., J. Kaklamanos, B. M. Berry, and E. M. Thompson (2016). Soil amplification with a strong impedance contrast: Boston, Massachusetts, *Eng. Geol.* **202,** 1–13.

Baxter, C. D. P., M. Page, A. S. Bradshaw, and M. Sherrill (2005). Guidelines for geotechnical site investigations in Rhode Island, *Final Report, Rhode Island Department of Transportation Study 0103*, 111 p.

Bierschenk, W. H. (1959). Ground-water resources of the Providence Quadrangle, Rhode Island, Rhode Island Water Resources Coordinating Board, *Rhode Island Geological Bull*. **10.**

Bindi, D., and D. Di Giacomomo (2024). Energy-magnitude station corrections across the conterminous United States, *Bulletin of the Seismological Society of America*, DOI: 10.1785/0120240092.

Boore, D. M. (2005). SMSIM – Fortran programs for simulating ground motions from earthquakes: Version 2.3 – A revision of OFR 96-80-A, *U.S. Geol. Surv. Open-File Rept. 2008–1128*, 55 pp.

Boore, D. M. (2016). Determining generic velocity and density models for crustal amplification calculations, with an update of the Boore and Joyner (1997) generic site amplification for $\bar{V}_S(Z)$ = 760 m/s, *Bull. Seismol. Soc. Am.* **106,** 313–317.

Bosbyshell, H. (2008). Bedrock geologic map of a portion of the Philadelphia Quadrangle, Montgomery and Philadelphia Counties, Pennsylvania, *Pennsylvania Geological Survey Open-File Report OFBM 08–05.0*, 21 p.

Boyd, O. S., D. Churchwell, M. P. Moschetti, E. M. Thompson, M. C. Chapman, O. Ilhan, T. L. Pratt, S. K. Ahdi, and S. Rezaeian (2024). Sediment thickness map of United States Atlantic and Gulf Coastal Plain Strata, and their influence on earthquake ground motions, *Earthquake Spectra* **40(1),** 89–112.

Brocher, T. M. (2005). Empirical relations between elastic wavespeeds and density in the Earth's crust, *Bull. Seism. Soc. Am.* **95**, 2081–2092.

Building Seismic Safety Council (BSSC) (2020). *NEHRP Recommended Seismic Provisions for New Buildings and Other Structures (FEMA P-2082-1): Volume 1: Part 1 Provisions, Part 2 Commentary*, Federal Emergency Management Agency, Washington, D.C., 593 pp.

Campbell, K. W. (2009). Estimates of shear-wave Q and $\kappa_0$ for unconsolidated and semiconsolidated sediments in Eastern North America. *Bull. Seism. Soc. Am.* **99(4),** 2365–2392

Campbell, K. W., Y. M. A. Hashash, B. Kim, A. R. Kottke, E. M. Rathje, W. Silva, and J. P. Stewart, J. P. (2014). Reference rock site condition for Central and Eastern North America Part II—Attenuation (Kappa) definition, *PEER Report No. 2014/12.* Pacific Earthquake Engineering Research Center, University of California.

Chapman, M. C., and P. Talwani (2006). Seismic hazard mapping for bridge and highway design in South Carolina, *Report No. FHWA-SC-06-09*, South Carolina Dept. of Transportation.

Chung, J. W., and J. D. Rogers (2010). GIS-based virtual geotechnical database for the St. Louis metro area, *Environmental & Engineering Geoscience* **16(2),** 143–162.

Chung, J. W., and J. D. Rogers (2012). Estimating the position and variability of buried bedrock surfaces in the St. Louis metro area, *Engineering Geology* **126,** 37–45.

Coleman, J. L., Jr., and S. M. Cahan (2012). Preliminary catalog of the sedimentary basins of the United States, *U.S. Geological Survey Open-File Report 2012–1111*, 27 p.

Cramer, C. H., J. S. Gomberg, E. S. Schweig, B. A. Waldron, and K. Tucker (2004). The Memphis, Shelby County, Tennessee, Seismic Hazard Maps, *U.S. Geological Survey Open-File Report 04-1294*, 41 p.

Darton, N. H. (1950). Configuration of the bedrock surface of the District of Columbia and vicinity, *U.S. Geological Survey Professional Paper 217*, 42 p.

Delgado, J., C. López Casado, J. Giner, A. Estévez, A. Cuenca, and S. Molina (2000). Microtremors as a geophysical exploration tool: Applications and limitations, *Pure and Applied Geophysics* **157,** 1445–1462.

DeMott, L.M., F. Stumm, and J. Finkelstein (2023). Bedrock-surface elevation and overburden thickness maps of the five boroughs, New York City, New York, *U.S. Geological Survey Data Report 1176,* 22 p.

Domrois, S., S. Marshak, C. C. Abert, and T. H. Larson (2015). ArcGIS maps depicting topography of the basement-cover contact (the Great Unconformity), and the traces of faults and folds, in the Cratonic Platform of the United States, *American Association of Petroleum Geologists Search and Discovery*, article 30410, 29 pp.

Fenneman, N.M., and D. W. Johnson (1946). Physiographic divisions of the conterminous U. S: U.S. Geological Survey data release, https://doi.org/10.5066/P9B1S3K8.

Fischer, K. M., L. A. Salvati, S. E. Hough, E. Gonzalez, C. E. Nelsen, and E. G. Roth (1995). Sediment-induced amplification in the Northeastern United States: a case study in Providence, Rhode Island, *Bulletin of the Seismological Society of America* **85(5),** 1388–1397.

Gann-Phillips, C., A. Cabas, C. Ji, C. Cramer, J. Kaklamanos, and O. Boyd (2024). Regional seismic velocity model for the U.S. Atlantic and Gulf Coastal Plains based on measured shear wave velocity, sediment thickness, and surface geology, *Earthquake Spectra* **40(2),** 1269–1300.

Gardner, G. H. F., L. W. Gardner, and A. R. Gregory (1974). Formation velocity and density—the diagnostic basics for stratigraphic traps, *Geophysics* **39,** 770–780.

Goulet, C. A., Y. Bozorgnia, N. Kuehn, L. Al Atik, R. R. Youngs, R. W. Graves, and G. M. Atkinson (2021a). NGA-East Ground-Motion Characterization model part I: Summary of products and model development, *Earthquake Spectra* **37,** 1231–1282.

Goulet, C. A., T. Kishida, T. D. Ancheta, C. H. Cramer, R. B. Darragh, W. J. Silva, Y. M. Hashash, J. Harmon, G. A. Parker, J. P. Stewart, and R. R. Youngs (2021b). PEER NGA-East database, *Earthquake Spectra* **37,** 1331–1353.

Hashash, Y. M. A., A. R. Kottke, J. P. Stewart, K. W. Campbell, B. Kim, C. Moss, S. Nikolaou, E. M. Rathje, and W. J. Silva (2014). Reference rock site condition for Central and Eastern North America, *Bull. Seism. Soc. Am.* **104(2),** 684–701.

Hashash, Y. M., O. Ilhan, J. A. Harmon, G. A. Parker, J. P. Stewart, E. M. Rathje, K. W. Campbell, and W. J. Silva (2020). Nonlinear site amplification model for ergodic seismic hazard analysis in central and eastern North America, *Earthquake Spectra*, **36(1),** 69–86.

Haskell, N. A. (1953). The dispersion of surface waves on multilayered media, *Bull. Seismol. Soc. Am.* **72,** 17–34.

Hassani, B., and G. M. Atkinson (2016). Site-effects model for central and eastern North America based on peak frequency, *Bulletin of the Seismological Society of America* **106(5),** 2197–2213.

Hassani, B., and G. M. Atkinson (2018). Site-effects model for Central and Eastern North America based on peak frequency and average shear-wave velocity, *Bulletin of the Seismological Society of America* **108(1),** 338–350.

Heath, D. C., D. J. Wald, C. B. Worden, E. M. Thompson, and G. M. Smoczyk (2020). A global hybrid $V_{S30}$ map with a topographic slope–based default and regional map insets, *Earthquake Spectra* **36(3),** 1570-1584.

Ibs-von Seht, M., and J. Wohlenberg (1999). Microtremor measurements used to map thickness of soft sediments, *Bull. Seism. Soc. Am.* **88,** 250–259

Jarvis, A., H. I. Reuter, A. Nelson, and E. Guevara (2008). Hole-filled seamless SRTM data V4, *International Centre for Tropical Agriculture (CIAT).*

Jaumé, S. C., and S. T. Ghanat (2015). Translating observed weak motion site response into predicted strong motion in Charleston, South Carolina, USA, *Sixth International Conference on Earthquake Geotechnical Engineering*, Christchurch, New Zealand, 2–4 November 2015, 8 pp.

Li, K., and C. Wetzel (2019). Site specific seismic studies for building projects in metropolitan New York City area, *Earthquake Geotechnical Engineering for Protection and Development of Environment and Constructions: Proceedings of the VII ICEGE Seventh International Conference on Earthquake Geotechnical Engineering*, Rome, Italy, 17–20 June 2019, CRC Press, F. Silvestri and N. Moraci (eds.), pp. 3585–3592.

Liu, S., Y. Wei, W. M. Post, R. B. Cook, K. Schaefer, and M. M. Thornton (2014). NACP MsTMIP: Unified North American Soil Map. *Oak Ridge National Laboratory Distributed Active Archive Center*. DOI: 10.3334/ORNLDAAC/1242.

Mabee, S. B., C. C. Duncan, W. P. Clement, and M. Pontrelli (2023). Massachusetts depth to bedrock project, *Massachusetts Department of Transportation Report No. 23-041*, 170 p.

MathWorks Inc. (2023). MATLAB version: 23.2.0.2515942 (R2023b), Update 7. Natick, Massachusetts: The MathWorks Inc., https://www.mathworks.com, last accessed November 2024.

McCafferty, A. E., C. A. San Juan, C. J. M. Lawley, G. E. Graham, M. G. Gadd, D. L. Huston, K. D. Kelley, S. Paradis, J. M. Peter, and K. Czarnota (2023). National-scale geophysical, geologic, and mineral resource data for the United States, Canada, and Australia. *U.S. Geological Survey data release*. DOI: 10.5066/P970GDD5.

Moschetti, M. P., E. M. Thompson, J. Rekoske, M. G. Hearne, P. M. Powers, D. E. McNamara, and C. Tape (2020). Ground-Motion amplification in Cook Inlet Region, Alaska, from intermediate-depth earthquakes, including the 2018 $M_w$ 7.1 Anchorage earthquake, *Seismological Research Letters* **91(1),** 142–152.

Nikolaou, S., and P. Edinger (2001). Seismic amplification of typical New York City soil profiles, *Fourth International Conference on Recent Advances in Geotechnical Earthquake Engineering and Soil Dynamics*, San Diego, California, 26–31 March 2001.

Nikolaou, S., G. Mylonakis, and P. Edinger (2001). Evaluation of site factors for seismic bridge design in New York City area, *Journal of Bridge Engineering* **6,** 564–576.

Nweke, C. C., J. P. Stewart, and S. J. Brandenberg (2020). Site response of southern California sedimentary basins and other geomorphic provinces. *Report GIRS-2020-12202012*. Los Angeles, CA: B. John Garrick Risk Institute, Natural Hazards Risk and Resiliency Research Center, University of California, Los Angeles.

Parker, G. A., J. A. Harmon, J. P. Stewart, Y. M. A. Hashash, A. R. Kottke, E. M. Rathje, W. J. Silva, and K. W. Campbell (2017). Proxy-based $V_{S30}$ estimation in Central and Eastern North America, *Bull. Seism. Soc. Am.* **107(1),** 117–131.

Parker, G. A., J. P. Stewart, Y. M. A. Hashash, E. M. Rathje, K. W. Campbell, and W. J. Silva (2019). Empirical linear seismic site amplification in Central and Eastern North America, *Earthquake Spectra* ***35*****(2),** 849–881.

Peck, R. B., and W. C. Reed (1954). Engineering properties of Chicago subsoils, *University of Illinois Engineering Experiment Station Bulletin No. 423*, 62 p.

Pelletier, J. D., P. D. Broxton, P. Hazenberg, X. Zeng, P. A. Troch, G.-Y. Niu, Z. Williams, M. A. Brunke, and D. Gochis (2016). A gridded global data set of soil, immobile regolith, and sedimentary deposit thicknesses for regional and global land surface modeling, *J. Adv. Model. Earth Syst.*, **8**, 41–65. DOI: 10.1002/2015MS000526.

Petersen, M. D., A. M. Shumway, P. M. Powers, C. S. Mueller, M. P. Moschetti, A. D. Frankel, S. Rezaeian, D. E. McNamara, N. Luco, O. S. Boyd, K. S. Rukstales, K. S. Jaiswal, E. M. Thompson, S. M. Hoover, B. S. Clayton, E. H. Field, and Y. Zeng (2020). The 2018 update of

the US National Seismic Hazard Model: Overview of model and implications, *Earthquake Spectra* **36(1)**, 5–41. DOI: 10.1177/8755293019878199.

Petersen, M. D., A. M. Shumway, P. M. Powers, E. H. Field, M. P. Moschetti, K. S. Jaiswal, K. R. Milner, S. Rezaeian, A. D. Frankel, A. L. Llenos, A. J. Michael, J. M. Altekruse, S. K. Ahdi, K. B. Withers, C. S. Mueller, Y. Zeng, R. E. Chase, L. M. Salditch, N. Luco, K. S. Rukstales, J. A. Herrick, D. L. Girot, B. T. Aagard, A. M. Bender, M. L. Blanpied, R. W. Briggs, O. S. Boyd, B. S. Clayton, C. B. DuRoss, E. L. Evans, P. J. Haeussler, A. E. Hatem, K. L. Haynie, E. H. Hearn, K. M. Johnson, Z. A. Kortum, N. S. Kwong, A. J. Makdisi, H. B. Mason, D. E. McNamara, D. F. McPhillips, P. G. Okubo, M. T. Page, F. F. Pollitz, J. L. Rubinstein, B. E. Shaw, Z.-K. Shen, B. R. Shiro, J. A. Smith, W. J. Stephenson, E. M. Thompson, J. A. Thompson Jobe, E. A. Wirth, and R. C. Witter (2024). The 2023 US 50-State National Seismic Hazard Model: Overview and implications, *Earthquake Spectra* **40(1),** 5–88. DOI: 10.1177/87552930231215428.

Porter, R., Y. Liu, and W. E. Holt (2016). Lithospheric records of orogeny within the continental U.S. *Geophysical Research Letters* **43**, 144–153. DOI: 10.1002/2015GL066950.

R Core Team (2024). R*: A Language and Environment for Statistical Computing*, R Foundation for Statistical Computing, Vienna, Austria, ISBN 3-900051-07-0.

Rekoske, J. M., M. P. Moschetti, and E. M. Thompson (2022). Basin and Site Effects in the US Pacific Northwest Estimated from Small-Magnitude Earthquakes, *Bulletin of the Seismological Society of America* **112(1),** 438–456.

Riegel, M. D., P. B. Pizzimenti, B. Materek, and E. M. Zamiskie (2019). Evaluating and managing risk: Replacement of the Brooklyn Queens Expressway (BQE) Connector for the Kosciuszko Bridge in New York, New York, *Geo-Congress 2019: Earth Retaining Structures and Geosynthetics*, 24–27 March 2019, Philadelphia, Pa., American Society of Civil Engineers (ASCE) Geotechnical Special Publication No. 306, C. L. Meehan, S. Kumar, M. A. Pando, and J. T. Joe (eds.), pp. 190–202.

Rorabaugh, M. I., F. F. Schrader, and L. B. Laird (1953). Water resources of the Louisville area, Kentucky and Indiana, *U.S. Geological Survey Circular 276*, 49 p.

Smith, J. H. (1956). Surficial geology of the Providence quadrangle, Rhode Island, *U.S. Geol. Surv. Geol. Quad. Map* 84.

Sofia, G., and E. I. Nikolopoulos (2020). Floods and rivers: a circular causality perspective. *Sci Rep* **10,** 5175. DOI: 10.1038/s41598-020-61533-x.

Soller, D. R., and C. P. Garrity (2018). Quaternary sediment thickness and bedrock topography of the glaciated United States east of the Rocky Mountains, *U.S. Geological Survey Scientific Investigations Map 3392*, 2 sheets. DOI: 10.3133/sim3392.

Soller, D. R., M. C. Reheis, C. P. Garrity, and D. R. Van Sistine (2009). Map Database for Surficial Materials in the Conterminous United States. *U.S. Geological Survey, Data Series 425*, scale 1:5,000,000.

Stanford, S. D. (2004). Surficial geology of the Camden and Philadelphia Quadrangles, Camden, Gloucester, and Burlington counties, New Jersey. *United States Geological Survey Open-File Map OFM 60*.

Stephenson, W. J., S. Hartzell, A. D. Frankel, M. Asten, D. L. Carver, and W. Y. Kim (2009). Site characterization for urban seismic hazards in lower Manhattan, New York City, from microtremor array analysis, *Geophys. Res. Lett.* **36,** L03301, doi:10.1029/2008GL036444.

Stewart, J. P., G. A. Parker, G. M. Atkinson, D. M. Boore, Y. M. A. Hashash, and W. J. Silva (2020). Ergodic site amplification model for central and eastern North America, *Earthquake Spectra* **36(1),** 42–68.

Thomann, T. G., and K. Chowdhury (2004). Shear wave velocity and its effect on seismic design forces and liquefaction assessment, *Fifth International Conference on Case Histories in Geotechnical Engineering*, New York City, N.Y., 13–17 April 2004.

Thompson, E. M., O. S. Boyd, D. Churchwell, and M. P. Moschetti (2023). *Central and Eastern U.S. Earthquake Ground Motion Database: 2010 to 2020*, Center for Engineering Strong Motion Data (CESMD). DOI: 10.5066/P9HX7MYG.

Thomson, W. T. (1950). Transmission of elastic waves through a stratified solid, *J. Appl. Phys.* **21,** 89–93.

Voigt, V. (2012). Depth to bedrock of the state of Missouri, *Missouri Dept. of Natural Resources*, https://geothermal.isgs.illinois.edu/aasggeothermal/modnr/map/MissouriDepthToBedrock.pdf, last accessed November 2024.

Wang, H., C. Li, R. Wen, and Y. Ren (2022). Integrating effects of source-dependent factors on sediment-depth scaling of additional site amplification to ground-motion prediction equation, *Bulletin of the Seismological Society of America* **112(1),** 400–418.

Woodhouse D., and P. J. Barosh (2011/2012). Geotechnical factors in Boston, *Civil Engineering Practice* **26/27,** 237–263.

Yang, L., S. Jin, P. Danielson, C. Homer, L. Gass, S. M. Bender, A. Case, C. Costello, J. Dewitz, J. Fry, M. Funk, B. Granneman, G. C. Liknes, M. Rigge, and G. Xian (2018). A new generation of the United States National Land Cover Database: Requirements, research priorities, design, and implementation strategies. *ISPRS Journal of Photogrammetry and Remote Sensing* **146,** 108–123. DOI: 10.1016/j.isprsjprs.2018.09.006.

# Appendix A: Geotechnical Characterizations of Major CEUS Cities

As part of this project, we compiled and analyzed depth-to-bedrock, shear-wave velocity, and other geotechnical data in a set of eleven (11) selected cities in the Central and Eastern United States (CEUS). The goal of the data compilation was to allow for more detailed seismic site response evaluations in a set of cities; in Chapter 3, we presented the results for Memphis, Tennessee, and New York City, New York. The geotechnical characterizations in this appendix will support future work by expanding these analyses to additional CEUS cities with varying geologic conditions. Moreover, this data could help support the development of geotechnical-informed terms that could be used to update our ergodic site amplification model in regions with extensive geotechnical data.

A map of the eleven cities included in this appendix is provided in Figure A1. We selected major cities that spanned a range of geologic conditions, geotechnical profiles, and seismic hazard levels. The following eleven cities are profiled in this appendix:

1. Boston, Massachusetts
2. Providence, Rhode Island
3. New York City, New York
4. Philadelphia, Pennsylvania
5. Washington, D.C.
6. Charleston, South Carolina
7. Cleveland, Ohio
8. Louisville, Kentucky
9. Chicago, Illinois
10. Saint Louis, Missouri
11. Memphis, Tennessee

The focus of the discussions in this appendix is on resources that describe the geologic conditions and depth to bedrock patterns in each city. There are many cities in the CEUS that are located in sedimentary basins where the soft soil deposits and a strong soil-bedrock impedance contrast have the potential to amplify seismic waves. These sedimentary basins increase the potential for earthquake-induced damage, especially in densely populated areas. More detailed geotechnical data, at the scale of cities, allow for more site-specific characterizations of sediment depths than those from more regional models such as Boyd et al. (2024), Soller and Garrity (2018), Domrois et. al. (2015), and Pelletier et al. (2016). This geotechnical data compilation could be used to validate the broader-scale sediment thickness models and perform more site-specific ground response analyses, especially in locations where shear-wave velocity data are available.


**Figure A1.** Locations of the eleven CEUS cities with geotechnical data compilations profiled in this appendix.

## A.1 Boston, Massachusetts

In Massachusetts, Mabee et al. (2023) undertook a significant effort to develop a detailed state-wide depth-to-bedrock map, illustrated in Figure A2. In the Mabee et al. (2023) model, bedrock elevations range from a high of 1059 meters at Mount Greylock to a low of −512 meters on Nantucket. These bedrock elevations correspond to minimum sediment thicknesses of zero throughout much of the state, to a maximum of 531 m in the Atlantic Coastal Plain in Nantucket. As expected, the thickest overburden is found in southeastern Massachusetts, Cape Cod and the Islands, the Boston basin, and in the larger river valleys. Several deep, glacially-eroded depressions exist in the Connecticut Valley in the west-central portion of the state. About 75 percent of the state has measurement uncertainties of less than 5 meters, particularly in locations where the depth to bedrock is shallow. Figure A3 provides a zoomed-in view of the Mabee et al. (2023) dataset in the Boston region.

Woodhouse and Barosh (2011/2012) performed a detailed review of geotechnical factors in Boston, Massachusetts. As summarized by Baise et al. (2016) in a study of site amplification in Boston, many areas of the city have been extensively filled, resulting in a layer of non-engineered fill overlying the natural soils throughout much of the city. Many areas have significant thicknesses of Boston Blue Clay, a glaciomarine clay deposited during the last Ice Age. On the other hand, locations in the city on outcrops of bedrock (often overlain by glacial till) may have no soft clay deposits. The depth to bedrock generally varies from 0 to a maximum of approximately 80 m in Boston. Figure A4 provides several generalized soil profiles for the city of Boston from Woodhouse and Barosh (2011/2012), indicating the range of profile types (e.g. sites with thick clay deposits vs. sites largely on glacial till and bedrock), as well as typical thicknesses.

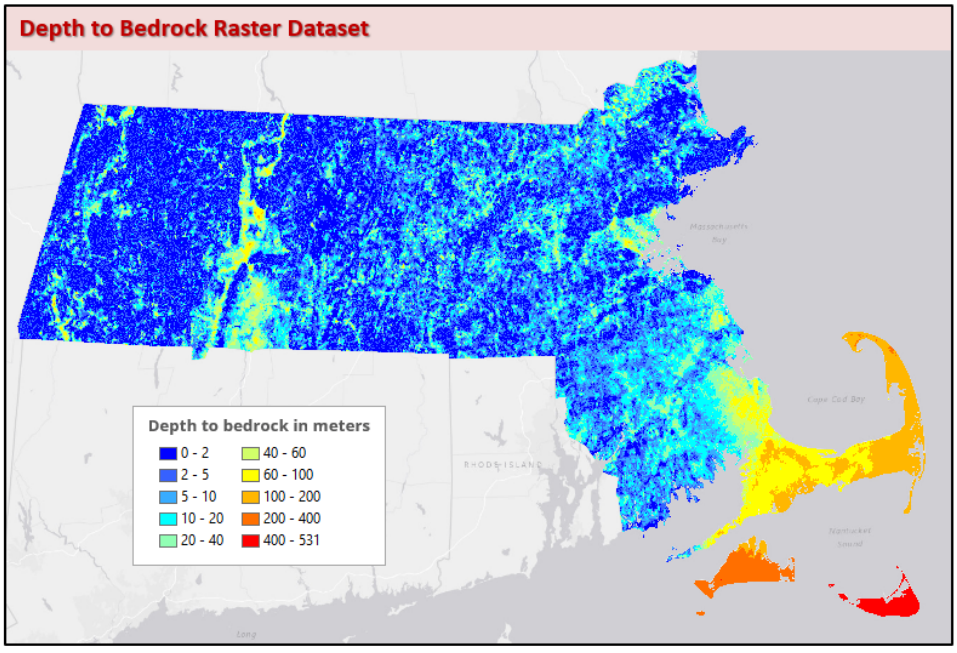


**Figure A2.** Mabee et al. (2023) depth-to-bedrock map for Massachusetts. Source: Mabee et al. (2023).

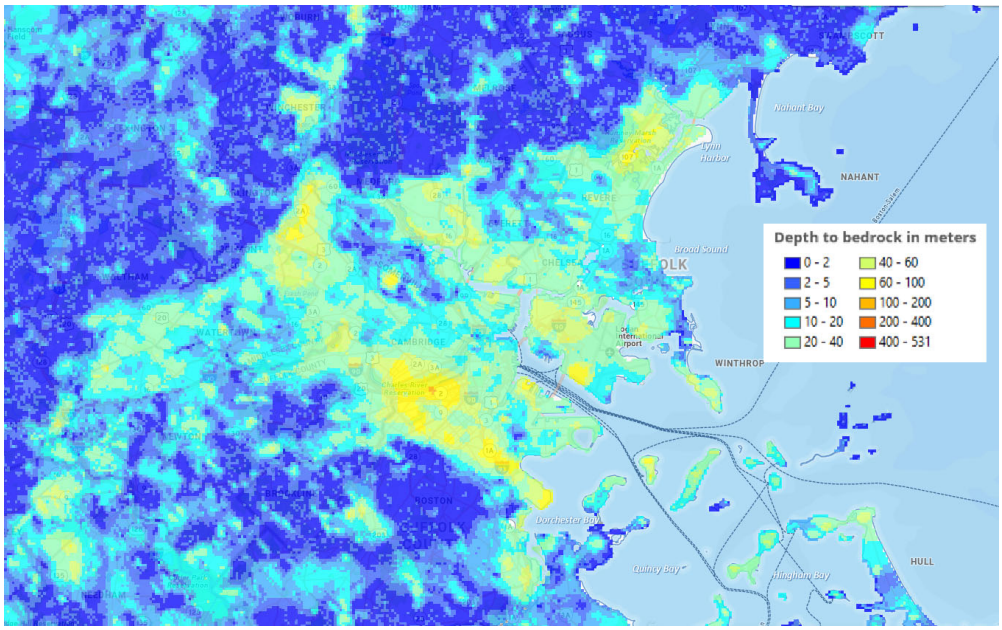


**Figure A3.** Mabee et al. (2023) depth-to-bedrock map for Massachusetts, zoomed in on the Boston region. Source: Adapted from https://maps.massgis.digital.mass.gov, using the Mabee et al. (2023) dataset.

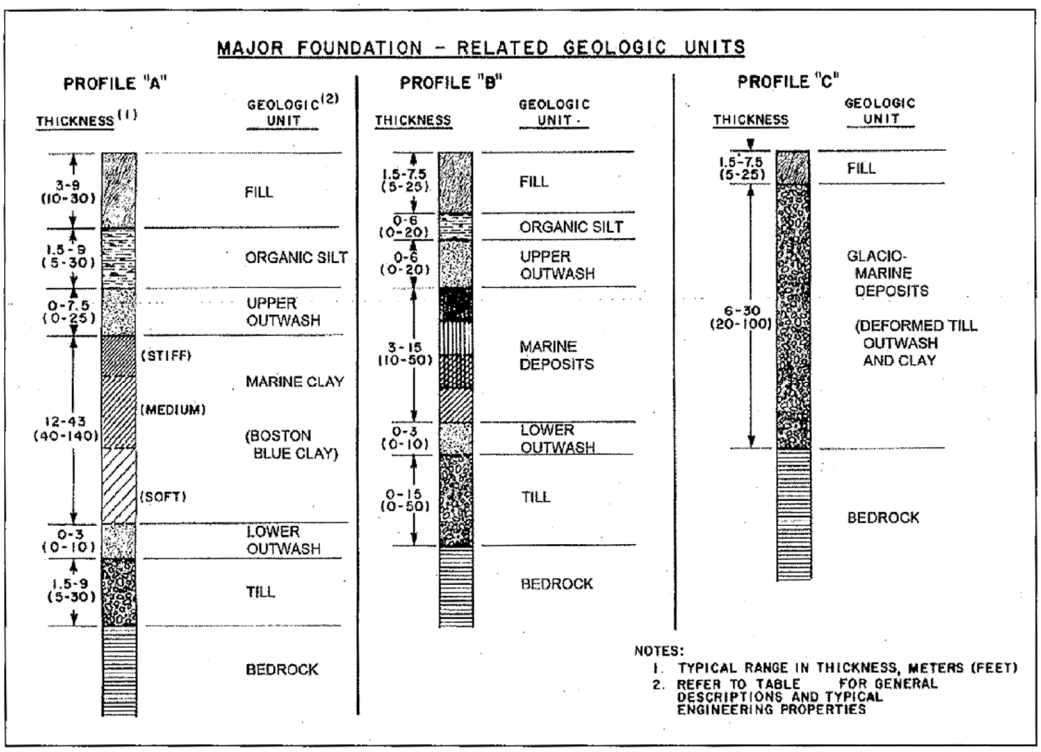


**Figure A4.** Woodhouse and Barosh (2011/2012) generalized geologic profiles for the city of Boston, indicating three common variations of sites, along with typical thicknesses of the various units. Source: Woodhouse and Barosh (2011/2012).

## A.2 Providence, Rhode Island

Providence, Rhode Island, is located in an area of varying depth to bedrock. Beneath downtown Providence, three branches of a bedrock valley system intersect. These valleys, which range in depth from 40 to 60 meters below the surface, are composed of artificial fill and unconsolidated settlements overlying compacted glacial till (Fischer et al., 1995; Smith, 1956; Bierschenk, 1959). Fischer et al. (1995) notes that there is an east-west trending bedrock valley beneath the Woonasquatucket River with a maximum depth of 50 to 60 meters that intersects with a smaller north-south trending bedrock valley with a maximum depth of 40 to 50 meters. This intersection opens to the south into a northwest and southeast trending bedrock valley with a maximum depth of 30 to 40 meters. In contrast, however, east of downtown (in the vicinity of Brown University), there is a bedrock outcrop covered by a thin (< 5 m) layer of glacial sediment (Fischer et al., 1995). Contours of surface topography and bedrock elevations from Fischer et al. (1995) are provided in Figure A5.

Baxter et al. (2005) notes that much of the sediments in downtown Providence are comprised of nonplastic silt, in contrast to Boston, where a plastic soft clay (the Boston Blue Clay) is much more prevalent. A representative soil profile from the Fox Point neighborhood, adjacent to Providence Harbor (southeast of downtown), is provided in Figure A6 (Baxter et al., 2005). The geotechnical profile in this area consists of artificial fill, overlying organic silt, glacial outwash, glacial till, and bedrock. The bedrock here is approximately 30 m below the ground surface, as this location is outside of the deeper 60- to 70-meter-deep bedrock valley within downtown Providence.

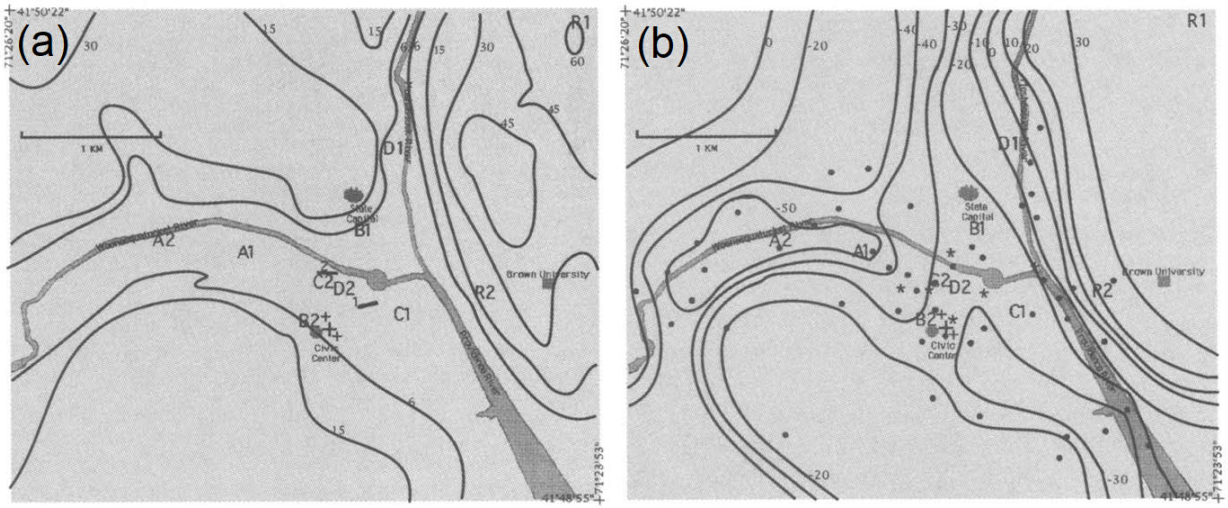


**Figure A5.** Fischer et al. (1995) contour maps of (a) ground surface elevation in meters, and (b) bedrock surface elevation in meters, for downtown Providence. Dots indicate the locations of borehole data. Source: Fischer et al. (1995).

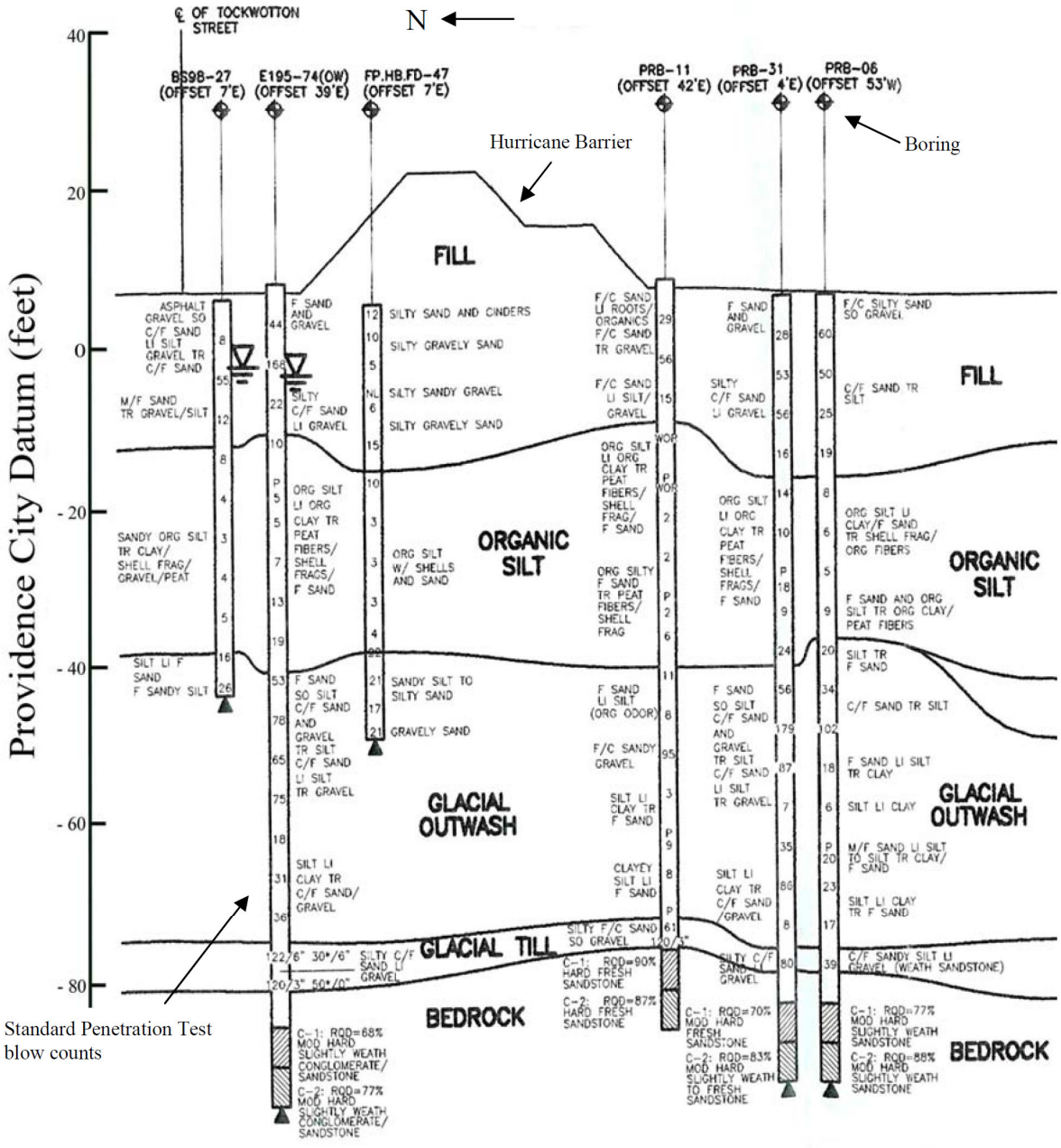


**Figure A6.** A representative soil profile from the Fox Point neighborhood, adjacent to Providence Harbor (southeast of downtown), illustrating typical layers observed in subsurface investigations in Providence. Depths are provided in feet. Source: Baxter et al. (2005).

## A.3 New York City, New York

As summarized in Chapter 3, New York City is located on the edge of the Atlantic Coastal Plain. DeMott et al. (2023) developed a comprehensive depth-to-bedrock model for the five boroughs of New York City, using historical data and horizontal-to-vertical spectral ratio (HVSR) measurements. Figure A7 (previously presented as Figure 3.10) illustrates the depth-to-bedrock model of DeMott et al. (2023), which provides bedrock depths in feet. There is a clear increase in sediment thickness from northwest to southeast as the Atlantic Coastal Plain thickens. Bedrock is typically shallow (generally 0 to 15 m deep) throughout most of Manhattan, the Bronx, and Staten Island (with the exception of the southern part of Staten Island, where it is deeper). Bedrock depths increase significantly in Brooklyn and Queens, reaching a maximum of approximately 360 m in the extreme southeastern portion of New York City on the Rockaway Peninsula. Because there is such a large variation in subsurface conditions, New York City was an interesting test case for the site response analyses we described in Chapter 3.

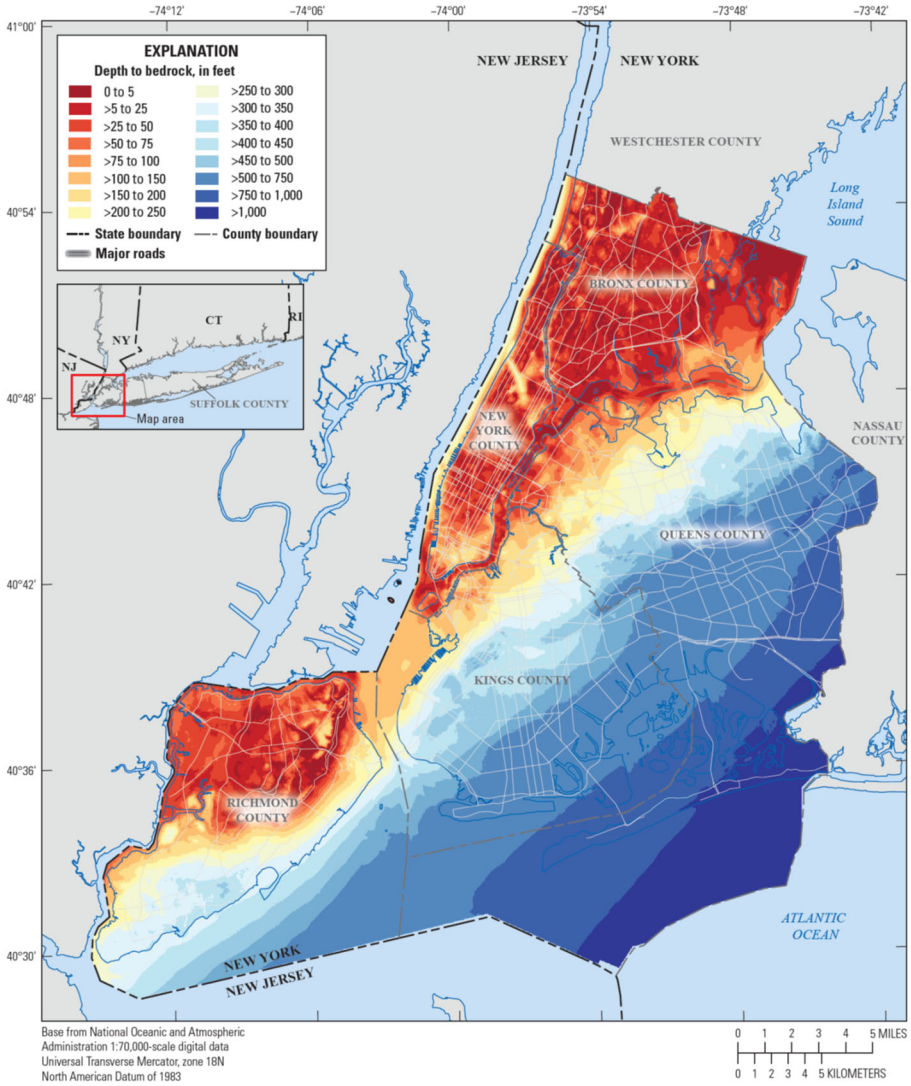


**Figure A7.** Depth-to-bedrock model of DeMott et al. (2023) for New York City. Depths are provided in feet. Previously presented as Figure 3.10. Source: DeMott et al. (2023).

# A.4 Philadelphia, Pennsylvania

Like New York City and Washington, D.C., Philadelphia is located on the edge of the Atlantic Coastal Plain. Geologic cross-sections of the Delaware River (which serves as the eastern boundary of the city), shown in Figure A8 from Stanford (2004), illustrate that the bedrock surface at the river is approximately 100 ft (30 m) below the ground surface. A map of bedrock geology and associated cross-section from Bosbyshell (2008) is provided in Figure A9. The edge of the Atlantic Coastal Plain can be observed along a southwest-northeast boundary that passes just to the northwest of downtown in the map. In the cross-section at the bottom of the figure, the dipping surface of the bedrock and the beginning of the coastal plain sediments can be observed in the far right of cross-section (which represents downtown Philadelphia). In summary, the sediment thickness in Philadelphia starts at zero northwest of downtown, and increases to approximately 30 m on the east side of the city near the Delaware River as the Atlantic Coastal Plain thickens.

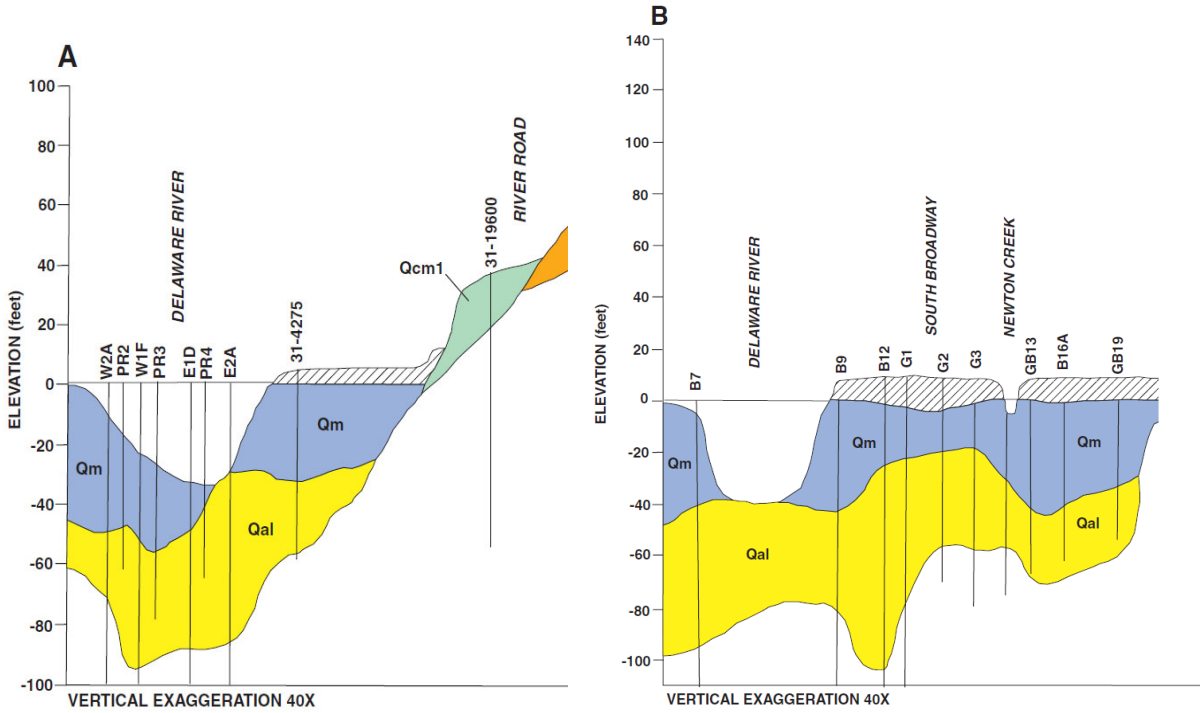


**Figure A8.** Stanford (2004) geologic cross-sections near the Delaware River, traversing west to east for (a) North Philadelphia (near the Betsy Ross Bridge), and (b) South Philadelphia (near the Walt Whitman Bridge). The base of the cross-sections are bedrock, and units are in feet. Source: Adapted from Stanford (2004).

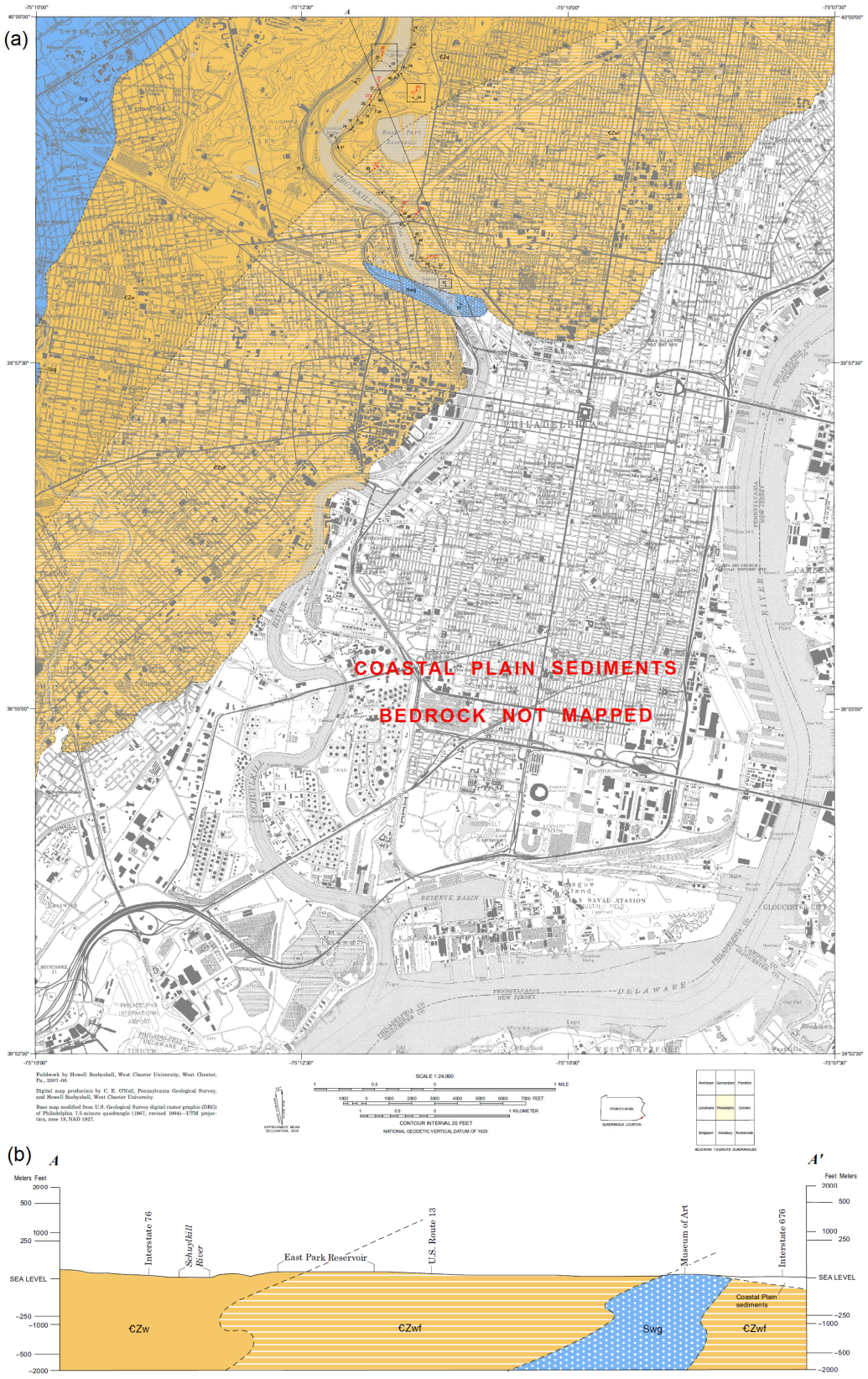


**Figure A9.** Bosbyshell (2008) (a) bedrock geologic map, and (b) cross-section A-A′ from the northwest side of Philadelphia to downtown. Source: Adapted from Bosbyshell (2008).

# A.5 Washington, D.C.

Washington, D.C., displays similar depth-to-bedrock patterns to New York City and Philadelphia, as it is located on the edge of the Atlantic Coastal Plain. Example cross-sections from Darton (1950) are illustrated in Figure A10, for (a) north-to-south and (b) west-to-east transects. The northwest side of the city is located out of the coastal plain, largely on bedrock or shallow soil. The increasing bedrock thickness is clearly visible from west to east as the bedrock dips and the coastal plain thickens, starting at zero in the Georgetown neighborhood (northwest of downtown) and increasing to approximately 100 m in the southeast side of the city.

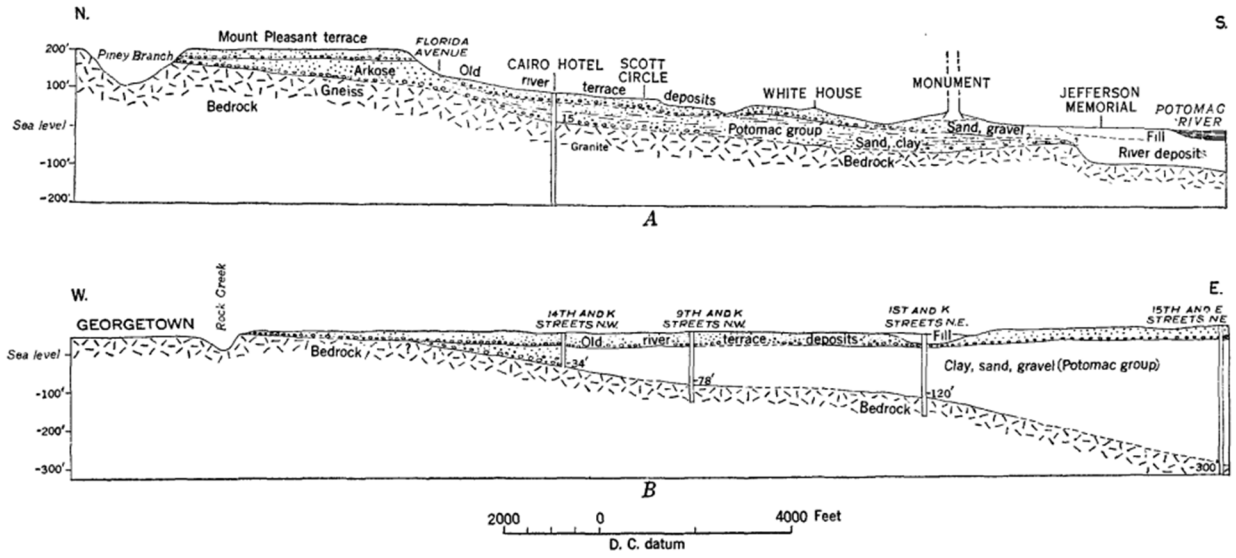


**Figure A10.** Darton (1950) geologic cross-sections through Washington, D.C., demonstrating clear indications of the dipping bedrock surface and thickening Atlantic Coastal Plain: (a) north to south along Sixteenth Street, and (b) west to east from Georgetown to Fifteenth and E Streets NE. Measurements are provided in feet. Source: Darton (1950).

## A.6 Charleston, South Carolina

Charleston, South Carolina, has the largest earthquake hazards of any metropolitan area on the East Coast of the United States. The 1886 Charleston earthquake caused extensive damage throughout the region, and the Atlantic Coastal Plain has a significant ground-shaking potential. Figure A11 provides a map of coastal plain sediment thickness for South Carolina derived from borehole and geophysical data, with a box highlighting the Charleston metropolitan area (Jaumé and Ghanat, 2015; Chapman and Talwani, 2006). The Coastal Plain thickness in the Charleston area is approximately 750 to 900 meters thick; in downtown, the depth to bedrock is approximately 850 m. The Atlantic Coastal Plain thickens from northwest to southeast across South Carolina; the edge of the coastal plain is about 150 km inland from Charleston.

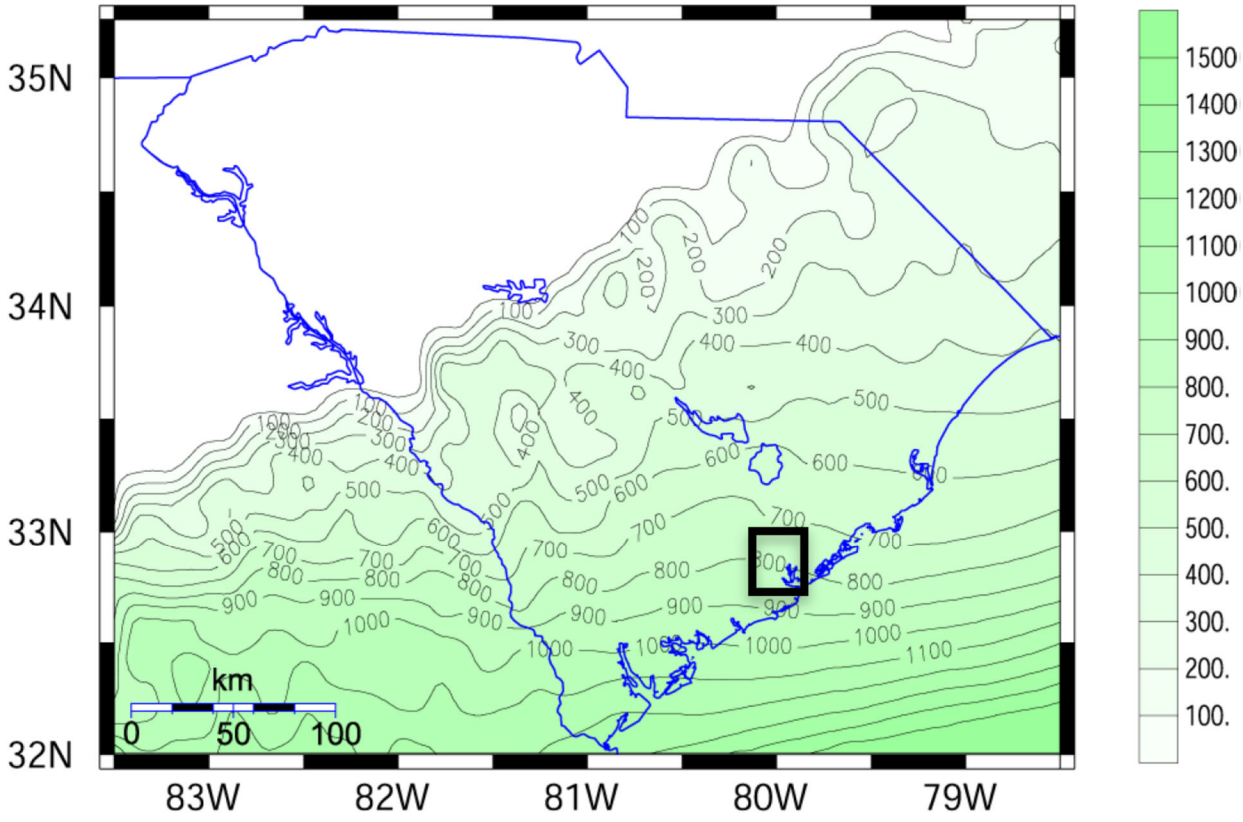


**Figure A11.** Thickness of Atlantic Coastal Plain sediments in South Carolina (in meters), derived from borehole and geophysical data. The box identifies the Charleston metropolitan area. Source: Jaumé and Ghanat (2015), derived from Chapman and Talwani (2006).

## A.7 Cleveland, Ohio

Moving inland, we now turn our discussion to several major cities located on significant rivers or lakes in the Midwest. Cleveland, Ohio, is located at the mouth of the Cuyahoga River, which flows into Lake Erie. An example cross-section of the Cuyahoga River Valley and corresponding soil types is shown in Figure A12 (Bagley, 1953). Soil borings in the area reveal layers of alluvial deposits from the Cuyahoga River, underlain by continuous till alternating with beds of lacustrine clay. The bedrock surface beneath Cuyahoga River follows a deep narrow valley up to approximately 700 ft (over 200 m) deep. The more recent sediment thickness map by Soller and Garrity (2018) in the vicinity of Cleveland, shown in Figure A13, also indicates a deep sedimentary basin (similar in depth to Figure A12) that is narrow in width. Although Cleveland is not in a region of high seismic hazards like Charleston, this basin geometry is quite interesting from a site response perspective.

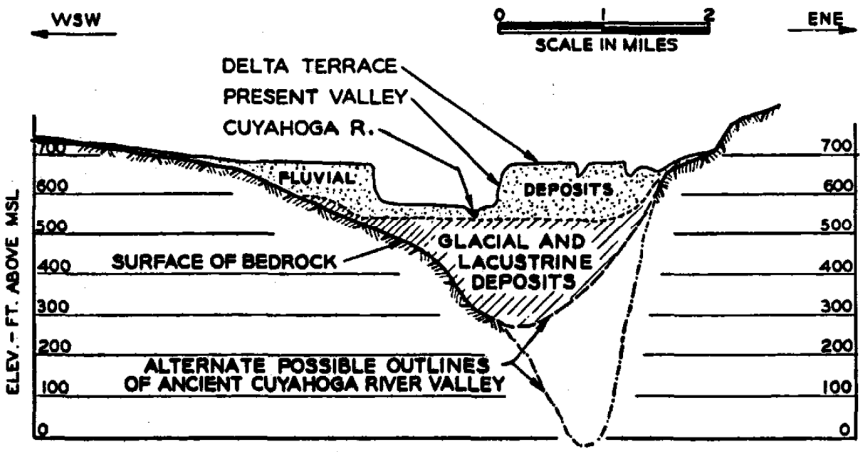


**Figure A12.** Bagley (1953) geologic cross-section of the Cuyahoga River Valley (from west to east) in the vicinity of Cleveland, Ohio. Units are feet. Source: Adapted from Bagley (1953).

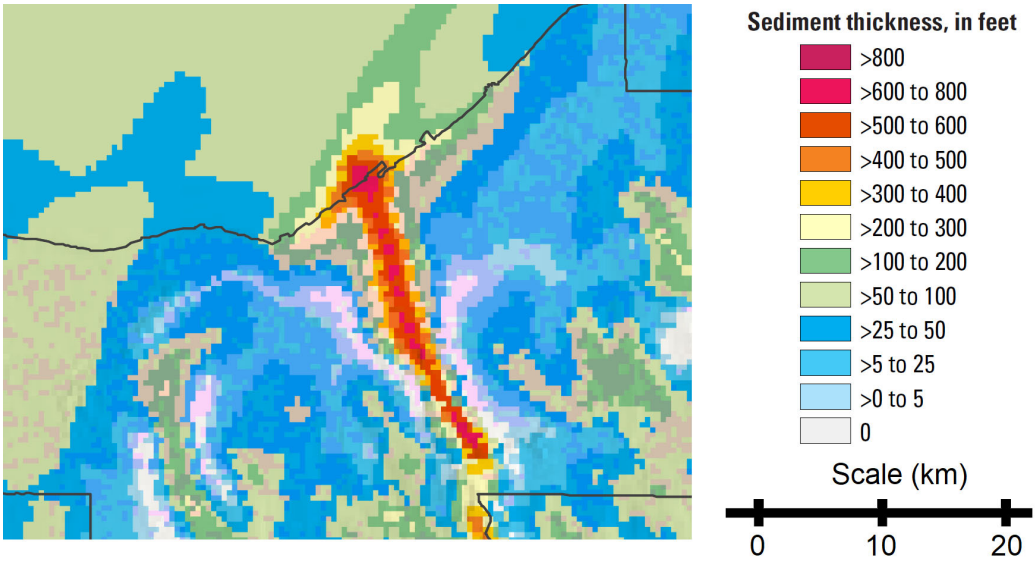


**Figure A13.** Soller and Garrity (2018) sediment thickness model (feet) in the vicinity of Cleveland, Ohio, indicating a deep narrow sedimentary basin beneath the Cuyahoga River. Source: Adapted from Soller and Garrity (2018).

# A.8 Louisville, Kentucky

Louisville, Kentucky, is located along the Ohio River near the southern periphery of the maximum glaciation during the last Ice Age. Figure A14 provides a cross-section through Louisville, Kentucky, from north to south across the Ohio River (Rorabaugh et al., 1953). During the glacial period, the Ohio River carved a deep valley into the bedrock, which was later filled with glacial sands, gravels, and river sediments. The bedrock valley is several miles wide in Louisville and has relatively constant thickness beneath the city, reaching maximum depths of approximately 30 to 40 m (100 to 130 ft). The bedrock beneath Louisville is predominantly limestone, but shales are present as well, particularly to the west of the city.

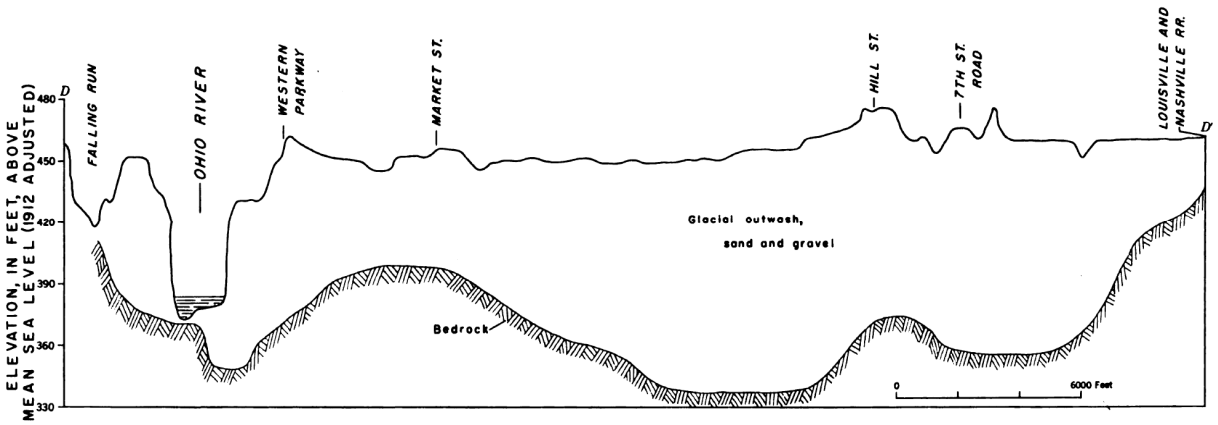


**Figure A14.** Rorabaugh et al. (1953) cross-section through Louisville, Kentucky, from north to south across the Ohio River. Units are feet. Source: Adapted from Rorabaugh et al. (1953).

# A.9 Chicago, Illinois

Chicago, Illinois, has been studied extensively from a geotechnical engineering perspective. In many regards, Chicago displays parallels to Boston because of the presence of clays deposited during the last glacial period, and roughly similar bedrock depths. Figure A15 displays a north-south geologic cross-section along State Street in downtown Chicago (Peck and Reed, 1954). The bedrock varies in thickness along the profile, and reaches a maximum depth of approximately 45 m (150 ft). The subsoil in the Chicago area primarily consists of layers of glacial clays, with each layer being slightly firmer than the one above it. Beneath layers of artificial fill and beach sand sometimes found beneath the surface, the glacial clays have soft to medium firmness; harder clays are generally encountered before reaching the bedrock. The bedrock itself is limestone, with a highly uneven surface, though it generally rises toward the west. In some places, there are exposed rock outcrops, while in others, the bedrock is found at a depth of up to 45 m. The overall depth to bedrock is quite irregular, making it difficult to predict its elevation at specific locations.

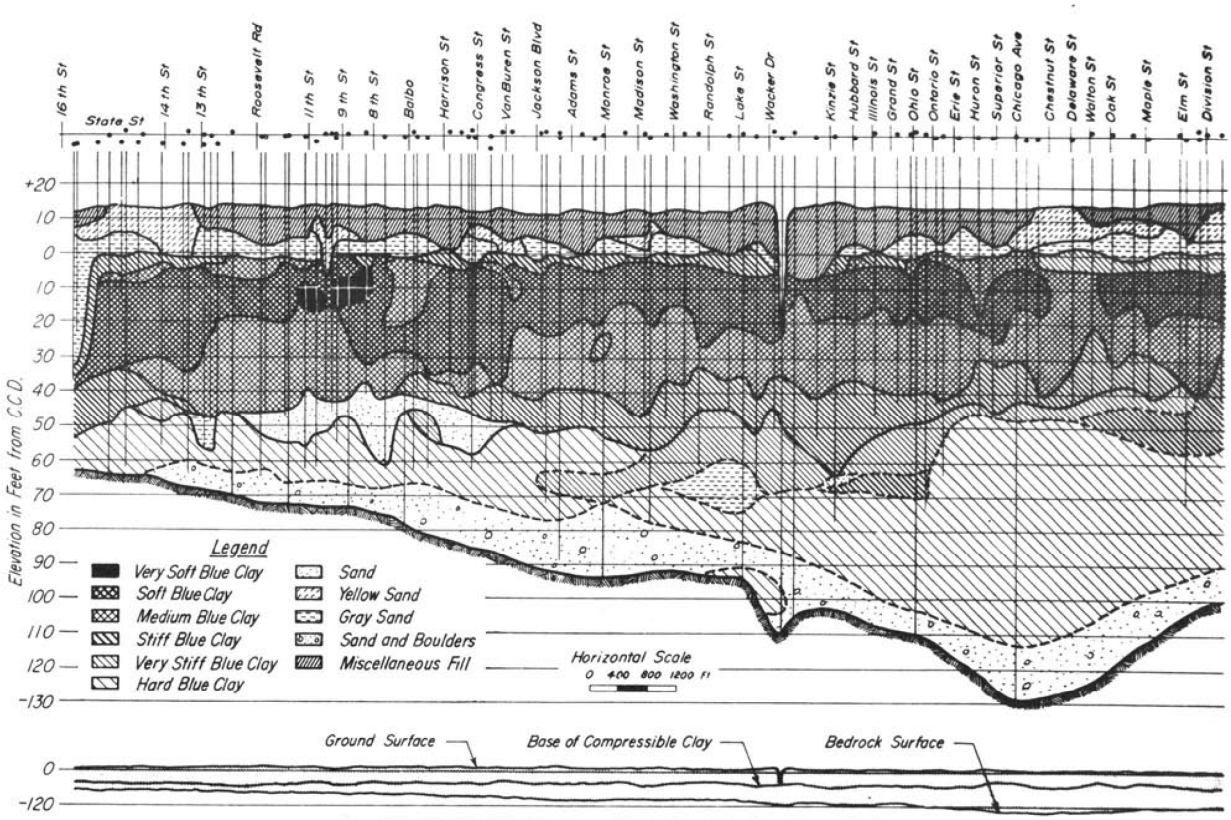


**Figure A15.** Peck and Reed (1954) geologic cross-section along State Street in downtown Chicago, from south (left side of figure) to north (right side of figure). Units are feet. Source: Peck and Reed (1954).

# A.10 Saint Louis, Missouri

Saint Louis, like Memphis, has been characterized extensively in terms of seismic hazards due to its proximity to the New Madrid Seismic Zone. Saint Louis is located along the Mississippi River just south of the confluence of the Missouri and Mississippi Rivers. Like Louisville, Saint Louis lies near the edge of the maximum glacial advance during the last Ice Age. A detailed characterization of subsurface conditions and development of a depth-to-bedrock model was undertaken by Chung and Rogers (2010, 2012). Figure A16 provides the depth-to-bedrock model model for the St. Louis region, and Figure A17 provides a cross-section across the Mississippi and Missouri River floodplains, in the vicinity of the deepest bedrock in the area (Chung and Rogers, 2012). Subsurface data indicates that in the St. Louis region, bedrock elevations are correlated with surface elevations; the bedrock is deeper in the river floodplains, and tends to become shallower in eroded, loess-covered highlands. Unconsolidated deposits in the floodplains ranged from 0 to 48 meters thick, with an average thickness of 35 meters. In the uplands, the bedrock is found between 0 to 48 meters deep, with an average depth of around 12 meters.

In addition, Voigt (2012) developed a depth-to-bedrock map for the entire state of Missouri, as shown in Figure A18. There are deeper bedrock depths in the northern and southeastern portions of the state, while the middle of the state tends to have shallower bedrock depths.

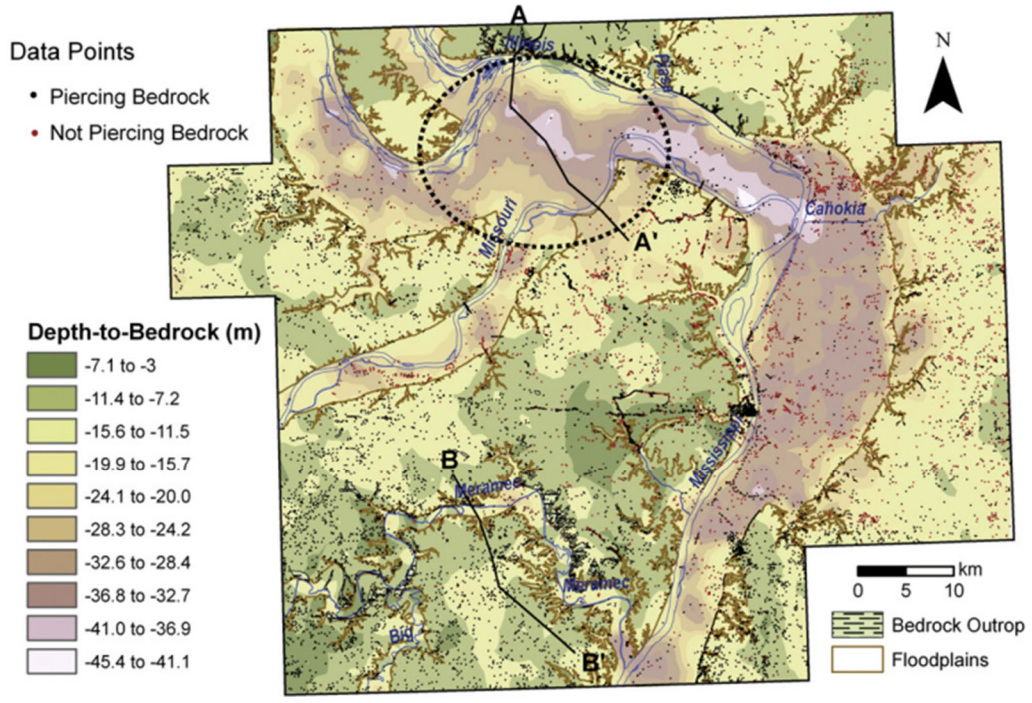


**Figure A16.** Chung and Rogers (2012) depth-to-bedrock model (meters) for the Saint Louis metropolitan area. The deeper bedrock in the floodplains of the Mississippi and Missouri Rivers is clearly observed. Downtown Saint Louis is located on the west bank of the Mississippi River, in the vicinity of a dense number of borings (marked as dots in the figure). Source: Chung and Rogers (2012).

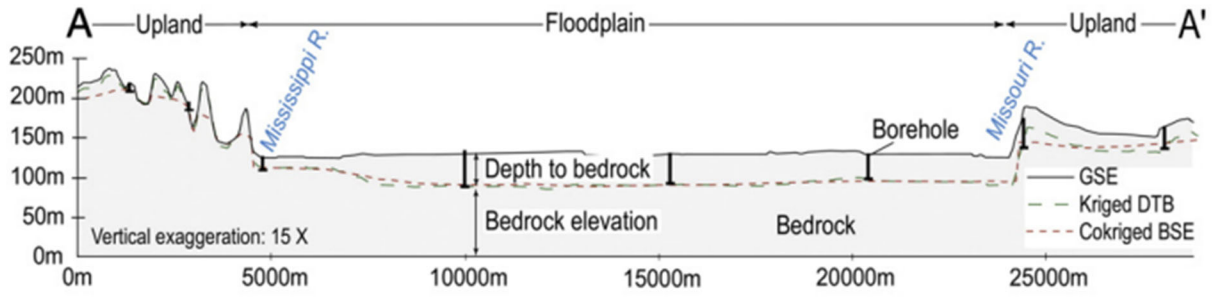


**Figure A17.** Chung and Rogers (2012) cross-section across the Mississippi and Missouri River floodplains, in the vicinity of the deepest bedrock in the area. The location of section A-A′ is marked in Figure A16, and traverses from northwest (A) to southeast (A′). Source: Chung and Rogers (2012).

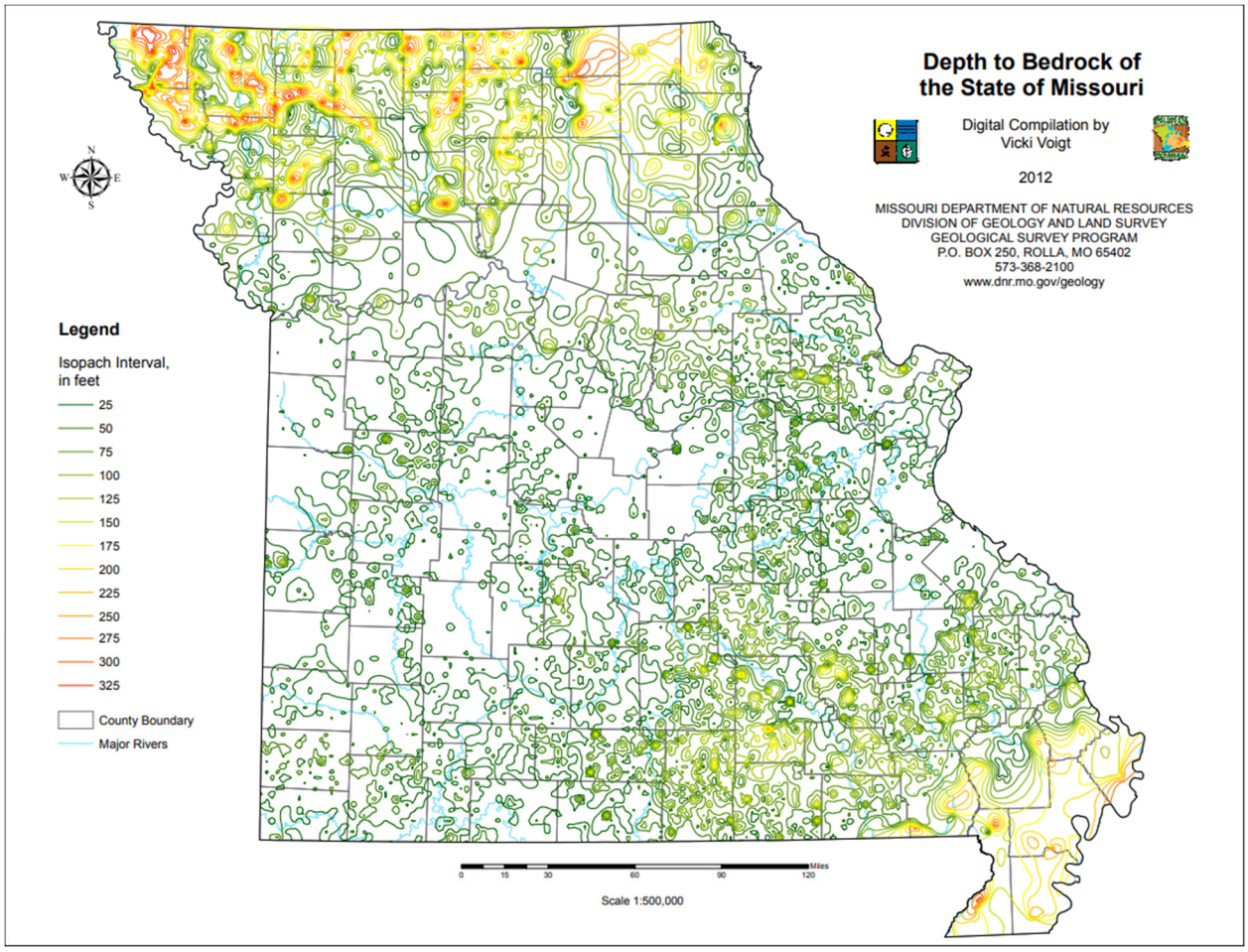


**Figure A18**. Voigt (2012) depth-to-bedrock map for the state of Missouri. Source: Voigt (2012).

## A.11 Memphis, Tennessee

Finally, like New York City, Memphis was previously analyzed in Chapter 3. Memphis, Tennessee, is located in the Mississippi Embayment in the Gulf Coastal Plain. Due to its high seismic hazard and close distance to the New Madrid Seismic Zone, Memphis is arguably the most well-characterized CEUS city in terms of seismic hazards. The depth to bedrock in Memphis is approximately 1 km, with the bedrock surface sloping downwards approaching the Mississippi River. Figure A19 (previously presented as Figure 3.1) shows the estimated depths of Paleozoic limestones and Cretaceous sediments from the model of Cramer et al. (2004). The increasing bedrock depths approaching the Mississippi River are clearly observed. We employed the recent Boyd et al. (2024) sediment thickness model for the Atlantic and Gulf Coastal Plains to characterize the depth to bedrock in Memphis, Tennessee. Boyd et al. (2024) defines the depth to bedrock as the base of the Cretaceous sediments underlying the Atlantic Coastal Plain and Mesozoic sediments underlying the Gulf Coastal Plain. Across the ground motion stations encountered in the vicinity of Memphis, Tennessee, the sediment thicknesses range from approximately 800 to 1300 m, with an average of 1100 to 1200 m.

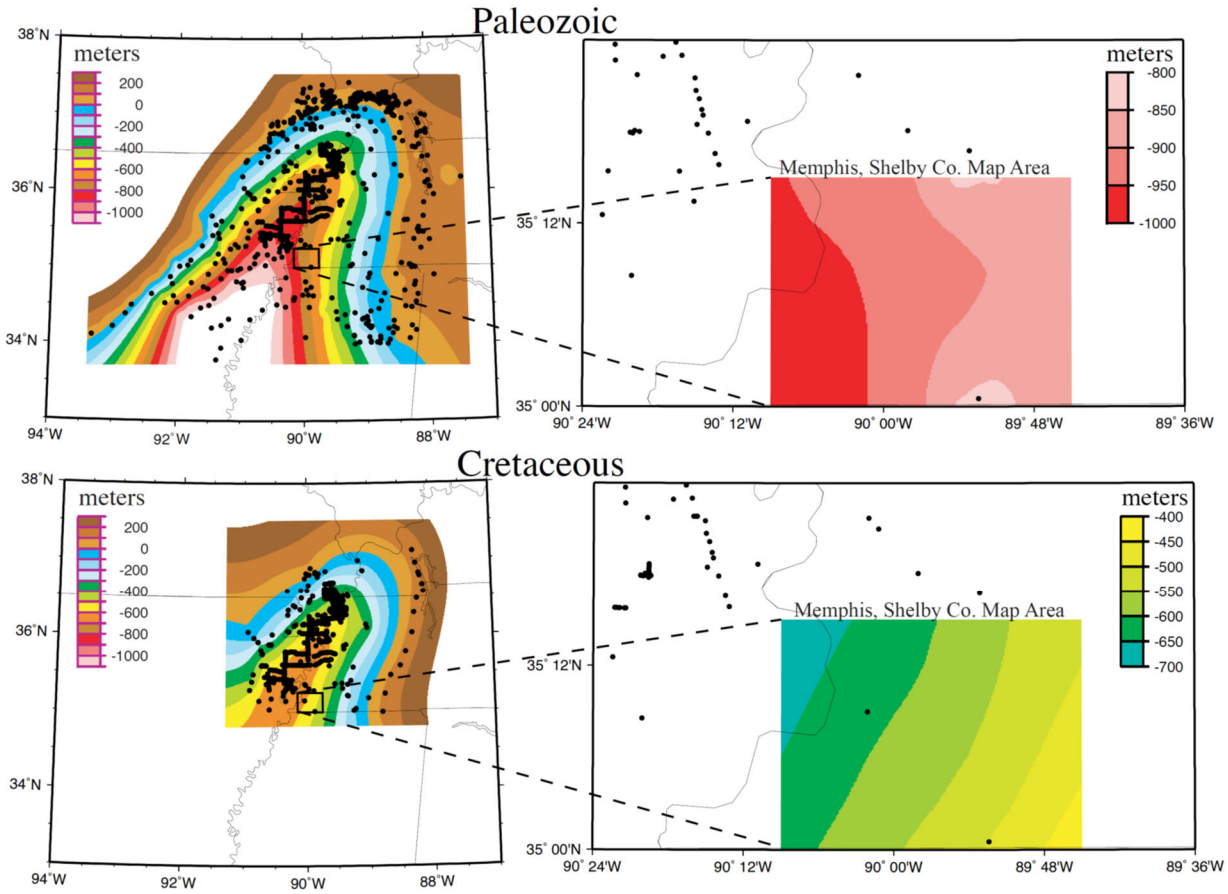


**Figure A19.** Estimated depths to the top of the Paleozoic limestones (top figures) and Cretaceous sediments (bottom figures) in the vicinity of Memphis, Tennessee. Black dots indicate locations where well log observations constrain these boundaries. Note that Memphis is at a surface elevation of approximately 100 m. Previously presented as Figure 3.1. Source: Cramer et al. (2004).

# Appendix B: Regional Patterns of Site-to-Site Terms

This appendix displays four figures that characterize the regional variation of site-to-site terms for four ground-motion intensity measures: spectral acceleration at 0.1 s (Figure B1), 1 s (Figure B2), and 3 s (Figure B3); and peak ground acceleration (Figure B4).

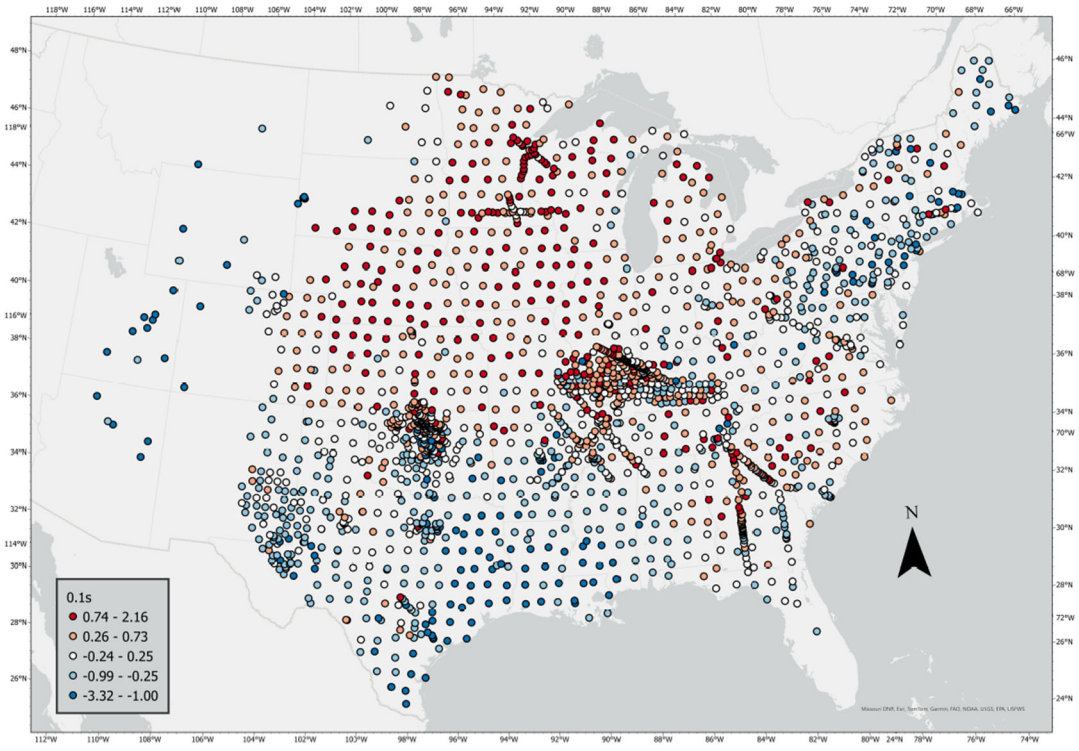


**Figure B1**. Regional variation of site-to-site terms for 0.1 s SA.

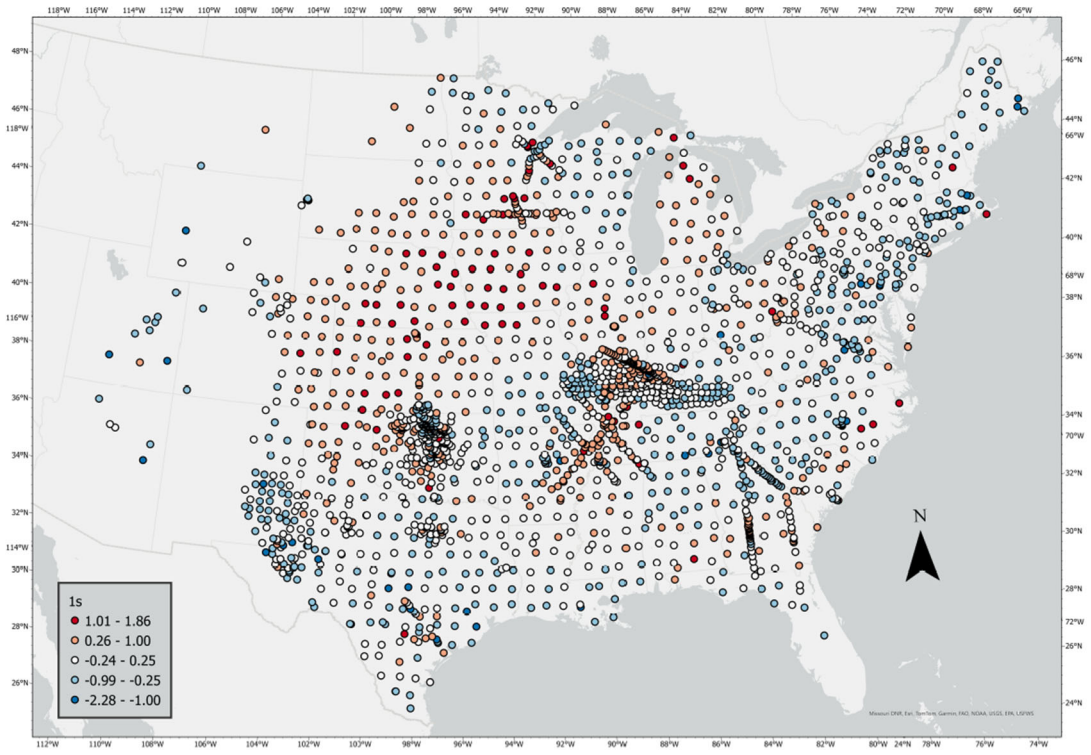


**Figure B2.** Regional variation of site-to-site terms for 1 s SA.

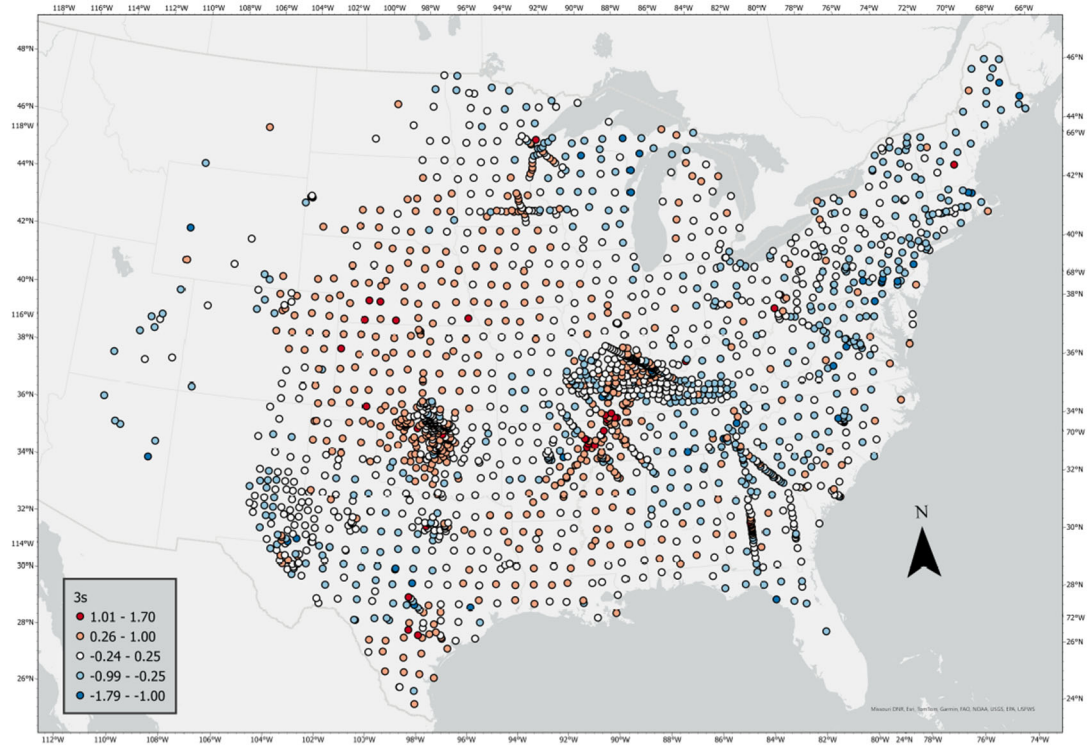


**Figure B3.** Regional variation of site-to-site terms for 3 s SA.

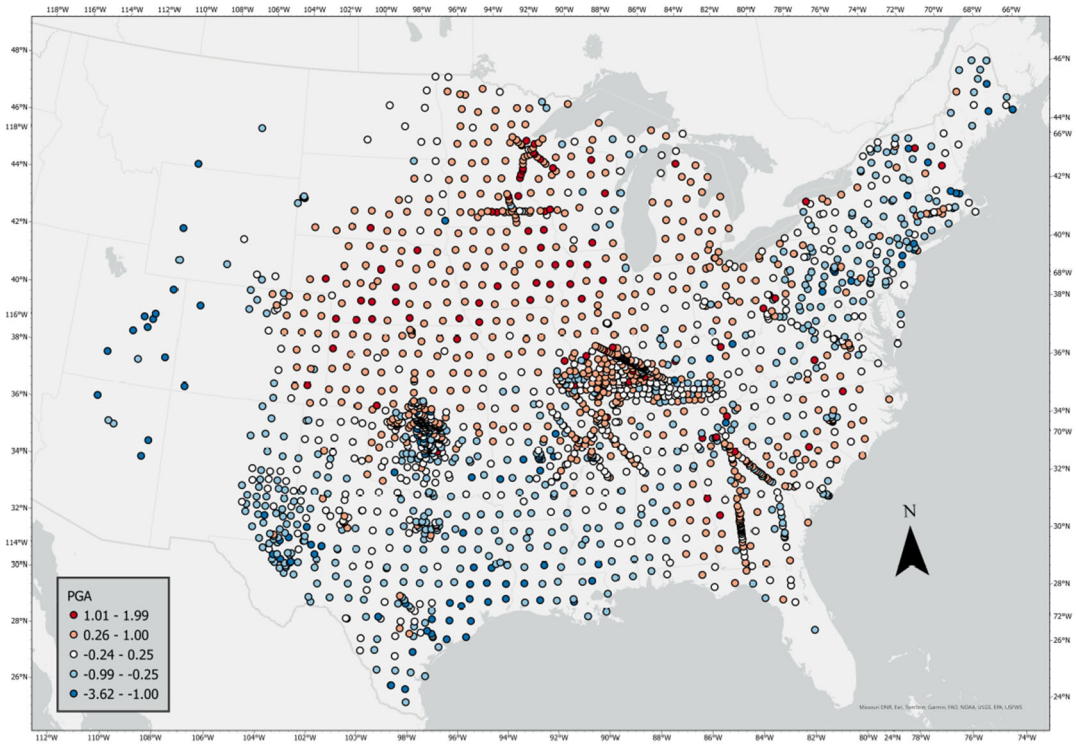


**Figure B4.** Regional variation of site-to-site terms for PGA.

# Appendix C: Regional Patterns of Site-to-Site Terms

This appendix includes the regression model coefficients in Equation 2.5: the intercept $F_{ADJPROVINCE,j}$ for the adjusted physiographic province of the site, and the slope $c_1$ that accompanies the sediment thickness at the site. Table C1 provides the regression coefficients for provinces within the Atlantic and Gulf Coastal Plains, which use sediment thickness from the Boyd et al. (2024) regional model. Tables C2 through C4 provide the regression coefficients for provinces outside of the Atlantic and Gulf Coastal Plains (in the northern CEUS), which use sediment thickness from the global Pelletier et al. (2016) model. Coefficients are provided for PGA, PGV, and spectral acceleration (SA) at 21 periods.

**Table C1.** Regression coefficients for provinces within the Atlantic and Gulf Coastal Plains

| Ground-motion parameter | Province-dependent intercept of regression model, $F_{ADJPROVINCE,j}$ | | | | | | | | | | | Slope ($c_1$) of regression model, for Boyd et al. (2024) sediment thickness |
|---|---|---|---|---|---|---|---|---|---|---|---|---|
| | CENTRAL TEXAS | EAST GULF COASTAL PLAIN | EDWARDS PLATEAU | EMBAYED | FLORIDIAN | HIGH PLAINS | MISSISSIPPI ALLUVIAL PLAIN | OSAGE PLAINS | PIEDMONT | SEA ISLAND | WEST GULF COASTAL PLAIN | |
| PGV | 0.027 | 0.878 | 0.043 | 0.930 | 0.583 | -0.005 | 1.055 | 0.326 | -0.114 | 0.787 | 0.640 | -5.70E-05 |
| PGA | -0.248 | 0.851 | 0.014 | 0.743 | 0.647 | -0.223 | 0.902 | 0.280 | 0.033 | 0.751 | 0.469 | -9.92E-05 |
| SA(T = 0.01 s) | 0.062 | 0.412 | -0.159 | 0.347 | 0.263 | -0.597 | 0.348 | -0.233 | -0.211 | 0.403 | -0.087 | -6.83E-05 |
| SA(T = 0.02 s) | -0.057 | 0.509 | -0.073 | 0.419 | 0.457 | -0.606 | 0.380 | -0.182 | -0.188 | 0.507 | -0.033 | -7.24E-05 |
| SA(T = 0.03 s) | -0.113 | 0.580 | -0.016 | 0.469 | 0.562 | -0.567 | 0.423 | -0.179 | -0.019 | 0.581 | -0.002 | -7.52E-05 |
| SA(T = 0.05 s) | -0.121 | 0.687 | 0.025 | 0.544 | 0.620 | -0.418 | 0.572 | -0.082 | 0.084 | 0.628 | 0.092 | -8.30E-05 |
| SA(T = 0.075 s) | 0.006 | 0.639 | 0.008 | 0.524 | 0.504 | -0.354 | 0.600 | -0.029 | 0.032 | 0.576 | 0.059 | -9.72E-05 |
| SA(T = 0.10 s) | 0.176 | 0.611 | -0.021 | 0.543 | 0.530 | -0.299 | 0.673 | 0.159 | 0.138 | 0.501 | 0.162 | -1.13E-04 |
| SA(T = 0.15 s) | 0.154 | 0.793 | 0.050 | 0.768 | 0.462 | -0.114 | 0.968 | 0.519 | 0.174 | 0.689 | 0.533 | -1.30E-04 |
| SA(T = 0.20 s) | 0.065 | 1.004 | 0.057 | 0.891 | 0.794 | -0.007 | 1.205 | 0.563 | 0.035 | 0.867 | 0.788 | -1.31E-04 |
| SA(T = 0.25 s) | 0.054 | 1.098 | 0.073 | 1.006 | 1.008 | 0.125 | 1.303 | 0.549 | -0.213 | 0.963 | 0.885 | -1.29E-04 |
| SA(T = 0.30 s) | 0.086 | 1.080 | 0.014 | 0.994 | 0.938 | 0.060 | 1.327 | 0.512 | -0.374 | 0.933 | 0.868 | -1.22E-04 |
| SA(T = 0.40 s) | 0.178 | 1.015 | -0.048 | 0.897 | 0.707 | 0.025 | 1.297 | 0.381 | -0.500 | 0.864 | 0.823 | -1.16E-04 |
| SA(T = 0.50 s) | 0.234 | 0.945 | -0.101 | 1.039 | 0.665 | 0.007 | 1.272 | 0.340 | -0.500 | 0.779 | 0.786 | -1.09E-04 |
| SA(T = 0.75 s) | 0.204 | 0.852 | -0.054 | 1.005 | 0.662 | 0.108 | 1.205 | 0.331 | -0.334 | 0.800 | 0.744 | -7.84E-05 |
| SA(T = 1.0 s) | 0.198 | 0.814 | -0.030 | 1.184 | 0.647 | 0.155 | 1.175 | 0.318 | -0.235 | 0.869 | 0.729 | -5.94E-05 |
| SA(T = 1.5 s) | 0.151 | 0.805 | -0.039 | 1.036 | 0.488 | 0.287 | 1.187 | 0.362 | -0.269 | 0.678 | 0.791 | -3.89E-05 |
| SA(T = 2.0 s) | 0.119 | 0.753 | 0.003 | 0.852 | 0.362 | 0.470 | 1.117 | 0.439 | -0.194 | 0.618 | 0.875 | -2.14E-05 |
| SA(T = 3.0 s) | 0.001 | 0.807 | 0.036 | 0.875 | 0.266 | 0.499 | 1.253 | 0.478 | -0.062 | 0.668 | 0.949 | -1.16E-05 |
| SA(T = 4.0 s) | -0.062 | 0.781 | 0.069 | 0.919 | 0.303 | 0.544 | 1.326 | 0.515 | -0.004 | 0.684 | 0.957 | -1.46E-05 |
| SA(T = 5.0 s) | -0.081 | 0.751 | 0.098 | 0.891 | 0.333 | 0.563 | 1.292 | 0.449 | 0.000 | 0.653 | 0.904 | -9.90E-06 |
| SA(T = 7.5 s) | -0.066 | 0.716 | 0.102 | 0.880 | 0.326 | 0.510 | 1.170 | 0.392 | 0.015 | 0.624 | 0.803 | -1.85E-06 |
| SA(T = 10.0 s) | -0.131 | 0.787 | 0.063 | 0.912 | 0.363 | 0.450 | 1.186 | 0.460 | 0.115 | 0.675 | 0.789 | -2.10E-07 |

**Table C2.** Regression coefficients for provinces in the northern CEUS outside of the Atlantic and Gulf Coastal Plains (1 of 3)

| Ground-motion parameter | Province-dependent intercept of regression model, $F_{ADJPROVINCE,j}$ | | | | | | | | | | | | |
|---|---|---|---|---|---|---|---|---|---|---|---|---|---|
| | ADIRONDACKS | APPALA-CHIAN PLATEAUS | BASIN AND RANGE | BLACK HILLS | BLUE RIDGE | CENTRAL TEXAS | COLORADO PIEDMONT | COLORADO PLATEAUS | DISSECTED TILL PLAINS | EAST GULF COASTAL PLAIN | EASTERN LAKE | EDWARDS PLATEAU | EMBAYED |
| PGV | -0.094 | 0.370 | -0.021 | -0.188 | 0.443 | 0.307 | 0.931 | -0.358 | 1.132 | 0.529 | 0.757 | -0.162 | 0.816 |
| PGA | -0.266 | 0.313 | -0.003 | -0.549 | 0.644 | 0.431 | 0.744 | -0.842 | 1.137 | 0.538 | 0.826 | -0.336 | 0.553 |
| SA(T = 0.01 s) | 0.262 | 0.003 | -0.404 | -1.407 | 0.072 | 0.227 | 0.213 | -1.478 | 0.695 | 0.079 | 0.574 | -0.999 | -0.153 |
| SA(T = 0.02 s) | 0.106 | 0.121 | -0.247 | -1.084 | 0.248 | 0.316 | 0.345 | -1.314 | 0.831 | 0.212 | 0.691 | -0.985 | -0.015 |
| SA(T = 0.03 s) | 0.034 | 0.177 | -0.135 | -0.900 | 0.369 | 0.376 | 0.423 | -1.216 | 0.899 | 0.285 | 0.762 | -0.968 | 0.067 |
| SA(T = 0.05 s) | -0.011 | 0.223 | 0.066 | -0.749 | 0.570 | 0.398 | 0.527 | -1.142 | 0.943 | 0.377 | 0.797 | -0.752 | 0.293 |
| SA(T = 0.075 s) | 0.145 | 0.122 | 0.166 | -0.811 | 0.591 | 0.399 | 0.478 | -1.326 | 0.891 | 0.240 | 0.772 | -0.433 | 0.355 |
| SA(T = 0.10 s) | 0.241 | 0.195 | 0.050 | -0.924 | 0.622 | 0.465 | 0.546 | -1.385 | 0.969 | 0.249 | 0.753 | -0.195 | 0.425 |
| SA(T = 0.15 s) | 0.002 | 0.403 | -0.144 | -0.766 | 0.772 | 0.633 | 0.866 | -1.163 | 1.277 | 0.669 | 0.968 | 0.071 | 0.659 |
| SA(T = 0.20 s) | -0.131 | 0.477 | -0.191 | -0.689 | 0.668 | 0.536 | 0.900 | -0.933 | 1.260 | 0.758 | 1.014 | 0.233 | 1.056 |
| SA(T = 0.25 s) | -0.160 | 0.511 | -0.300 | -0.620 | 0.564 | 0.466 | 0.943 | -0.784 | 1.197 | 0.799 | 1.017 | 0.201 | 0.765 |
| SA(T = 0.30 s) | -0.152 | 0.490 | -0.231 | -0.610 | 0.434 | 0.474 | 0.930 | -0.691 | 1.207 | 0.857 | 0.947 | 0.026 | 0.969 |
| SA(T = 0.40 s) | -0.178 | 0.488 | -0.069 | -0.484 | 0.391 | 0.517 | 1.034 | -0.529 | 1.223 | 0.924 | 0.925 | 0.025 | 1.021 |
| SA(T = 0.50 s) | -0.210 | 0.489 | 0.074 | -0.388 | 0.372 | 0.442 | 1.057 | -0.397 | 1.224 | 0.763 | 0.944 | 0.107 | 0.400 |
| SA(T = 0.75 s) | -0.199 | 0.461 | 0.070 | -0.216 | 0.259 | 0.327 | 1.051 | -0.213 | 1.204 | 0.523 | 0.895 | 0.090 | 1.256 |
| SA(T = 1.0 s) | -0.121 | 0.357 | 0.050 | -0.185 | 0.112 | 0.229 | 0.944 | -0.156 | 1.020 | 0.288 | 0.736 | 0.120 | 1.543 |
| SA(T = 1.5 s) | -0.194 | 0.339 | 0.090 | 0.025 | 0.106 | 0.263 | 1.047 | 0.080 | 0.931 | 0.320 | 0.675 | 0.336 | 0.811 |
| SA(T = 2.0 s) | -0.296 | 0.372 | 0.192 | 0.355 | 0.159 | 0.385 | 1.270 | 0.262 | 0.906 | 0.439 | 0.666 | 0.498 | 0.741 |
| SA(T = 3.0 s) | -0.405 | 0.453 | 0.462 | 0.302 | 0.270 | 0.411 | 1.271 | 0.291 | 0.941 | 0.490 | 0.700 | 0.609 | 0.921 |
| SA(T = 4.0 s) | -0.436 | 0.453 | 0.398 | 0.183 | 0.322 | 0.378 | 1.317 | 0.149 | 0.968 | 0.434 | 0.704 | 0.875 | 1.045 |
| SA(T = 5.0 s) | -0.438 | 0.418 | 0.273 | 0.048 | 0.342 | 0.403 | 1.445 | 0.124 | 0.984 | 0.421 | 0.700 | 0.827 | 1.032 |
| SA(T = 7.5 s) | -0.434 | 0.385 | 0.234 | 0.018 | 0.382 | 0.411 | 1.400 | 0.051 | 0.984 | 0.500 | 0.707 | 0.757 | 1.049 |
| SA(T = 10.0 s) | -0.442 | 0.369 | 0.163 | -0.021 | 0.393 | 0.347 | 1.320 | -0.002 | 0.980 | 0.551 | 0.698 | 0.647 | 1.075 |

**Table C3.** Regression coefficients for provinces in the northern CEUS outside of the Atlantic and Gulf Coastal Plains (2 of 3)

| Ground-motion parameter | Province-dependent intercept of regression model, $F_{ADJPROVINCE,j}$ | | | | | | | | | | | |
|---|---|---|---|---|---|---|---|---|---|---|---|---|
| | HIGH PLAINS | INTERIOR LOW PLATEAUS | MIDDLE ROCKY MOUNTAINS | MISSISSIPPI ALLUVIAL PLAIN | MISSOURI PLATEAU, GLACIATED | MISSOURI PLATEAU, UNGLACIATED | NEW ENGLAND | OSAGE PLAINS | OUACHITA | OZARK PLATEAUS | PECOS VALLEY | PIEDMONT |
| PGV | 0.835 | 0.612 | -0.575 | 1.041 | 0.777 | 1.064 | -0.050 | 0.587 | -0.087 | 0.428 | 0.042 | 0.418 |
| PGA | 0.640 | 0.643 | -0.961 | 1.090 | 0.535 | 1.142 | -0.038 | 0.502 | -0.247 | 0.579 | -0.069 | 0.581 |
| SA(T = 0.01 s) | 0.276 | 0.144 | -1.644 | 0.384 | 0.106 | 0.660 | -0.420 | -0.227 | -0.907 | 0.122 | -0.586 | 0.021 |
| SA(T = 0.02 s) | 0.395 | 0.272 | -1.488 | 0.464 | 0.202 | 0.905 | -0.309 | -0.184 | -0.837 | 0.166 | -0.523 | 0.194 |
| SA(T = 0.03 s) | 0.450 | 0.343 | -1.378 | 0.532 | 0.256 | 1.050 | -0.225 | -0.123 | -0.776 | 0.220 | -0.474 | 0.315 |
| SA(T = 0.05 s) | 0.494 | 0.459 | -1.307 | 0.762 | 0.318 | 1.151 | -0.103 | 0.144 | -0.531 | 0.435 | -0.243 | 0.475 |
| SA(T = 0.075 s) | 0.423 | 0.509 | -1.574 | 0.707 | 0.222 | 1.207 | -0.145 | 0.247 | -0.495 | 0.570 | -0.113 | 0.475 |
| SA(T = 0.10 s) | 0.483 | 0.541 | -1.644 | 0.758 | 0.428 | 1.223 | -0.126 | 0.430 | -0.397 | 0.632 | -0.057 | 0.508 |
| SA(T = 0.15 s) | 0.711 | 0.754 | -1.217 | 1.320 | 0.809 | 1.503 | 0.016 | 0.855 | -0.041 | 0.740 | 0.139 | 0.735 |
| SA(T = 0.20 s) | 0.754 | 0.792 | -0.912 | 1.819 | 0.841 | 1.303 | 0.029 | 1.000 | 0.089 | 0.750 | 0.183 | 0.792 |
| SA(T = 0.25 s) | 0.755 | 0.725 | -0.800 | 1.566 | 0.675 | 1.170 | -0.018 | 0.976 | 0.085 | 0.658 | 0.225 | 0.708 |
| SA(T = 0.30 s) | 0.788 | 0.670 | -0.738 | 1.480 | 0.654 | 1.033 | -0.076 | 0.905 | 0.062 | 0.586 | 0.228 | 0.566 |
| SA(T = 0.40 s) | 0.918 | 0.661 | -0.702 | 1.264 | 0.622 | 1.092 | -0.095 | 0.835 | 0.065 | 0.495 | 0.263 | 0.415 |
| SA(T = 0.50 s) | 1.023 | 0.668 | -0.618 | 1.200 | 0.783 | 1.170 | -0.085 | 0.817 | 0.101 | 0.453 | 0.329 | 0.340 |
| SA(T = 0.75 s) | 1.065 | 0.591 | -0.582 | 0.796 | 1.014 | 1.171 | -0.080 | 0.733 | 0.041 | 0.301 | 0.366 | 0.274 |
| SA(T = 1.0 s) | 0.981 | 0.511 | -0.470 | 0.607 | 0.917 | 1.103 | -0.169 | 0.656 | -0.064 | 0.142 | 0.311 | 0.190 |
| SA(T = 1.5 s) | 1.061 | 0.558 | -0.322 | 0.592 | 1.000 | 1.104 | -0.138 | 0.766 | 0.062 | 0.184 | 0.429 | 0.217 |
| SA(T = 2.0 s) | 1.191 | 0.636 | -0.067 | 0.739 | 1.213 | 1.271 | -0.056 | 0.868 | 0.223 | 0.350 | 0.595 | 0.283 |
| SA(T = 3.0 s) | 1.160 | 0.703 | -0.058 | 0.862 | 1.059 | 1.188 | 0.040 | 1.048 | 0.333 | 0.530 | 0.716 | 0.367 |
| SA(T = 4.0 s) | 1.131 | 0.691 | -0.189 | 0.905 | 0.927 | 1.080 | 0.084 | 1.115 | 0.429 | 0.625 | 0.790 | 0.401 |
| SA(T = 5.0 s) | 1.119 | 0.669 | -0.269 | 0.925 | 0.841 | 1.092 | 0.080 | 1.090 | 0.448 | 0.657 | 0.817 | 0.398 |
| SA(T = 7.5 s) | 1.058 | 0.670 | -0.352 | 0.974 | 0.845 | 1.087 | 0.089 | 1.062 | 0.398 | 0.661 | 0.759 | 0.423 |
| SA(T = 10.0 s) | 0.994 | 0.672 | -0.387 | 1.030 | 0.851 | 1.056 | 0.087 | 1.081 | 0.386 | 0.669 | 0.699 | 0.432 |

**Table C4.** Regression coefficients for provinces in the northern CEUS outside of the Atlantic and Gulf Coastal Plains (3 of 3)

| Ground-motion parameter | Province-dependent intercept of regression model, $F_{ADJPROVINCE,j}$ | | | | | | | | | | | Slope ($c_1$) of regression model, for Pelletier et al. (2016) sediment thickness |
|---|---|---|---|---|---|---|---|---|---|---|---|---|
| | PLAINS BORDER | RATON | SEA ISLAND | SOUTHERN ROCKY MOUNTAINS | ST. LAWRENCE VALLEY | SUPERIOR UPLAND | TILL PLAINS | VALLEY AND RIDGE | WESTERN LAKE | WISCONSIN DRIFTLESS | WYOMING BASIN | |
| PGV | 1.302 | 0.482 | 0.565 | 0.115 | -0.094 | 0.768 | 0.917 | 0.178 | 0.959 | 0.674 | -0.096 | 0.00431 |
| PGA | 1.098 | 0.301 | 0.777 | -0.092 | -0.105 | 1.097 | 0.936 | 0.148 | 0.985 | 1.066 | -0.464 | 0.00336 |
| SA(T = 0.01 s) | 0.649 | -0.183 | 0.447 | -0.505 | -0.684 | 1.096 | 0.436 | -0.164 | 0.810 | 0.985 | -1.025 | 0.00093 |
| SA(T = 0.02 s) | 0.762 | -0.081 | 0.597 | -0.373 | -0.520 | 1.208 | 0.557 | -0.053 | 0.913 | 1.108 | -0.892 | 0.00093 |
| SA(T = 0.03 s) | 0.814 | -0.012 | 0.661 | -0.296 | -0.380 | 1.252 | 0.628 | 0.013 | 0.955 | 1.188 | -0.808 | 0.00110 |
| SA(T = 0.05 s) | 0.876 | 0.135 | 0.718 | -0.231 | -0.175 | 1.216 | 0.715 | 0.100 | 0.956 | 1.231 | -0.745 | 0.00195 |
| SA(T = 0.075 s) | 0.787 | 0.188 | 0.687 | -0.291 | -0.167 | 1.268 | 0.766 | -0.021 | 0.936 | 1.409 | -0.928 | 0.00178 |
| SA(T = 0.10 s) | 0.874 | 0.153 | 0.707 | -0.321 | -0.176 | 1.242 | 0.847 | 0.027 | 0.981 | 1.398 | -0.975 | 0.00195 |
| SA(T = 0.15 s) | 1.208 | 0.320 | 0.808 | -0.169 | -0.058 | 1.288 | 1.115 | 0.207 | 1.200 | 1.332 | -0.657 | 0.00362 |
| SA(T = 0.20 s) | 1.323 | 0.431 | 1.048 | -0.099 | -0.069 | 1.144 | 1.158 | 0.254 | 1.139 | 1.033 | -0.425 | 0.00559 |
| SA(T = 0.25 s) | 1.352 | 0.562 | 0.851 | -0.069 | -0.046 | 1.067 | 1.097 | 0.282 | 1.090 | 0.898 | -0.289 | 0.00657 |
| SA(T = 0.30 s) | 1.365 | 0.558 | 0.740 | -0.014 | -0.060 | 0.960 | 1.043 | 0.249 | 1.035 | 0.793 | -0.254 | 0.00694 |
| SA(T = 0.40 s) | 1.433 | 0.604 | 0.701 | 0.137 | -0.142 | 0.832 | 1.064 | 0.243 | 0.992 | 0.782 | -0.201 | 0.00713 |
| SA(T = 0.50 s) | 1.513 | 0.680 | 0.410 | 0.161 | -0.092 | 0.799 | 1.071 | 0.238 | 1.121 | 0.755 | -0.165 | 0.00698 |
| SA(T = 0.75 s) | 1.526 | 0.616 | 0.324 | 0.249 | -0.053 | 0.663 | 0.964 | 0.222 | 1.122 | 0.683 | -0.007 | 0.00613 |
| SA(T = 1.0 s) | 1.388 | 0.452 | 0.246 | 0.166 | -0.141 | 0.545 | 0.822 | 0.145 | 0.913 | 0.487 | -0.034 | 0.00608 |
| SA(T = 1.5 s) | 1.543 | 0.505 | 0.305 | 0.185 | -0.121 | 0.516 | 0.803 | 0.113 | 0.876 | 0.442 | 0.171 | 0.00544 |
| SA(T = 2.0 s) | 1.600 | 0.632 | 0.343 | 0.331 | -0.080 | 0.490 | 0.820 | 0.151 | 0.912 | 0.374 | 0.304 | 0.00512 |
| SA(T = 3.0 s) | 1.488 | 0.718 | 0.441 | 0.345 | 0.069 | 0.542 | 0.938 | 0.223 | 0.920 | 0.400 | 0.348 | 0.00526 |
| SA(T = 4.0 s) | 1.486 | 0.817 | 0.517 | 0.254 | 0.189 | 0.553 | 0.995 | 0.260 | 0.889 | 0.415 | 0.148 | 0.00522 |
| SA(T = 5.0 s) | 1.448 | 0.889 | 0.515 | 0.330 | 0.163 | 0.563 | 1.000 | 0.237 | 0.871 | 0.431 | 0.100 | 0.00527 |
| SA(T = 7.5 s) | 1.377 | 0.807 | 0.551 | 0.267 | 0.167 | 0.562 | 0.970 | 0.221 | 0.861 | 0.432 | 0.126 | 0.00554 |
| SA(T = 10.0 s) | 1.353 | 0.781 | 0.547 | 0.241 | 0.124 | 0.544 | 0.952 | 0.212 | 0.847 | 0.417 | 0.093 | 0.00566 |